5-2013

The Contribution of Magnetospheric Currents to Ground Magnetic Perturbation during Geomagnetic Storms

Swadesh Patra
Utah State University

THE CONTRIBUTION OF MAGNETOSPHERIC CURRENTS TO GROUND MAGNETIC PERTURBATION DURING GEOMAGNETIC STORMS

by

Swadesh Patra

A dissertation submitted in partial fulfillment
of the requirements for the degree

of

DOCTOR OF PHILOSOPHY

in

Electrical Engineering

Approved:

Dr. Edmund Spencer Major Professor	Dr. Robert Schunk Committee Member
Dr. Charles M. Swenson Committee Member	Dr. Reyhan Bakhtur Committee Member
Dr. Jacob Gunther Committee Member	Dr. Mark R. McLellan Vice President for Research and Dean of the School of Graduate Studies

UTAH STATE UNIVERSITY
Logan, Utah

2013

Abstract

The Contribution of Magnetospheric Currents to Ground Magnetic Perturbation During Geomagnetic Storms

by

Swadesh Patra, Doctor of Philosophy

Utah State University, 2013

Major Professor: Dr. Edmund Spencer
Department: Electrical and Computer Engineering

A geomagnetic storm is triggered in response to a disturbance in the solar wind. The earth's ring current gets energized during a geomagnetic storm, which leads to a decrease in the horizontal component of the geomagnetic field on the earth's surface. The Disturbance Storm Time (Dst) index, which is a measure of the intensity of the ring current, is calculated by taking the average of this decrease in the horizontal intensity across four low latitude magnetometer stations and removing the quiet time secular variations. The rate of decrease of the Dst index is an indicator of the deenergization of the ring current particles. But there are several issues with the Dst measurement as a proxy of the ring current energy. In particular, the percentage contribution of the tail current effect to the Dst index is still debated. In this work, an effort has been made to separate and quantify the possible contribution of the tail current to the Dst index. The relative contribution for a selected set of storms for which the interplanetary magnetic field turned northward abruptly after the peak in Dst was observed is estimated.

The WINDMI model of the nightside magnetosphere is used to investigate the contributions of ring current, magnetotail current, and magnetopause current on the observed two-phase decay of the Dst index. The role of different solar wind magnetosphere coupling

functions on the Dst index calculated by the WINDMI model is also investigated. The performance of four other coupling functions in addition to the rectified vBs is evaluated. These coupling functions emphasize different physical mechanisms to explain the energy transfer into the magnetosphere due to solar wind velocity, dynamic pressure, magnetic field, and Mach number. One coupling function is due to Siscoe, another by Borovsky, and two by Newell. The results indicate that for a majority of cases, at most only vx, By, and Bz are needed to sufficiently account for the supply of energy to the ring current and geotail current components that contribute to the Dst index.

The capabilities of the WINDMI model to reliably determine the state of the global magnetosphere are improved by employing the the Magnetotail (MT) index as a measurement constraint during large geomagnetic storms. The MT index is used as a proxy for the strength of the magnetotail current in the magnetosphere. The inclusion of the MT index as an optimization constraint in turn increases our confidence that the ring current contribution to the Dst index calculated by the WINDMI model is correct during large geomagnetic storms. To improve the models prediction of AL index, we also modify the ionospheric conductivity and fit to two substorms.

The rate of reduction of convection in the magnetotail for some of these storms is numerically simulated by using inner magnetospheric models like the Fok Ring Current (FRC) and the Rice Convection Model along with the global BATSRUS model at the community coordinated modeling center. Model results are compared against magnetometer data by creating movie maps from several low-latitude magnetometer stations.

The results indicate the contribution from the tail current to the Dst is important. In addition, the reduction of the cross-tail current during substorm dipolarization is predicted by the measured isotropic boundary locations. Several well known phenomena are identified in the magnetometer movie maps.

(182 pages)

Public Abstract

The Contribution of Magnetospheric Currents to Ground Magnetic Perturbation During Geomagnetic Storms

by

Swadesh Patra, Doctor of Philosophy

Utah State University, 2013

Major Professor: Dr. Edmund Spencer
Department: Electrical and Computer Engineering

A geomagnetic storm is a disturbance in the earth's space environment in response to a disturbance in the solar wind. The earth's ring current that is a toroidal current flowing roughly in the region also occupied by the Van-Allen radiation belt is energized during a geomagnetic storm. This leads to a decrease in the horizontal component of the geomagnetic field on the earth's surface. The Disturbance Storm Time (Dst) index, which is a measure of the intensity of the ring current, is calculated by taking the average of this decrease in the horizontal intensity across four low latitude magnetometer stations and removing the quiet time secular variations. The rate of decrease of the Dst index is an indicator of the deenergization of the ring current particles. But there are several issues with the Dst measurement as a proxy of the ring current energy. In particular, the percentage contribution of the tail current effect to the Dst index is still debated. In this work, an effort has been made to separate and quantify the possible contribution of the tail current to the Dst index. The relative contribution for a selected set of storms for which the interplanetary magnetic field turned northward abruptly after the peak in Dst was observed is estimated.

The results indicate the contribution from the tail current to the Dst is important. In addition, the reduction of the cross-tail current during substorm dipolarization is predicted by the measured isotropic boundary locations. Several well known phenomena are identified in the magnetometer movie maps. The improved space weather prediction capability obtained as a result of this work helps in protecting our space based assets. The auroral precipitation that affects airline traffic on polar routes and ground-induced currents that affect long pipe lines and electricity grids can now be better understood and protected.

To my Teachers.

Acknowledgments

The acknowledgments page never does justice to all the people who have contributed towards the work. Whatever little knowledge that I have gained in this life is because of my teachers. They have come in different forms, as parents, friends, strangers, and teachers in the literal sense. It is they, who have influenced my thought process and inspired me to learn.

My journey from a graduate student, who wanted to do research but did not know how, to now, where I feel confident enough to approach any problem in life, would not have been possible without Dr. Spencer. He has been my guide, friend, critic, and inspiration throughout. His belief in me, when I was struggling, helped me overcome my fears and gave me strength. I will be forever indebted to him for so many lessons in life.

I am also thankful to Dr. Swenson for being such a great teacher and for getting me started in the field of space science. Dr. Wendell Horton from University of Texas, Austin, has constantly helped me with my projects and has always inspired me to look at challenging problems. His energy and enthusiasm after working for so many years is something that I hope to imbibe.

In the summer of 2009, Dr. Spencer and Dr. Jan Sojka had a brief discussion, and Dr. Sojka's suggestions led to this work. Dr. Schunk and Dr. Sojka have been an inspiration for me throughout these last six years. I hope that their passion of attempting challenging problems rubs off on me. Dr. Baktur and Dr. Gunther have always been very supportive of my work.

The road to my doctoral degree has been long and winding. I could not have survived without the support of my parents, relatives, and friends. I would like to thank you all for believing in me.

Swadesh Patra

Contents

List of Tables

List of Figures

Chapter 1

Introduction and Project Overview

The earth's magnetic field is comprised of two parts: an internal dipolar magnetic field originating in the core, and the more dynamic external magnetic field created by the combined effects of the solar wind and various magnetospheric currents. The magnetosphere of the earth is defined as the region of influence of the earth's magnetic field. The magnetosphere is formed when the solar wind pushes against the earth's magnetic field and creates a cavity in the solar wind. The various regions of the magnetosphere are shown in fig. 1.1.

The earth's magnetosphere is bounded by a thin current layer called the magnetopause, which is shaped somewhat like a windsock, and preceded upstream by a hyperboloidal bow shock through which the solar wind makes a transition from super magnetosonic to sub magnetosonic flow velocity. A gap $2 - 3R_E$ (earth radii, $1R_E = 6371.2$ km by convention) separates the bow shock from the magnetopause along the earth-sun line because the magnetopause itself presents a blunt obstacle to the flowing solar wind [1]. The interaction with the solar wind deforms the earth's basically dipolar magnetic field, compressing the field lines on the day side and stretching them out to form a long comet-like tail (the magnetotail) on the night side. On the day side, the magnetosphere extends out to a distance of approximately 10 earth radii (under quiet conditions), while the magnetotail extends several hundred earth radii in the antisunward direction.

In this chapter the different magnetospheric currents and some of their physical processes are discussed briefly. In addition, space weather indices which were used frequently during this work are explained. Some of the popular techniques to model the magnetosphere are also briefly introduced. In particular, the physics based WINDMI model and the ring current models are explained in some detail. Finally, the motivation for the work done here is presented and the organization of the dissertation is discussed.

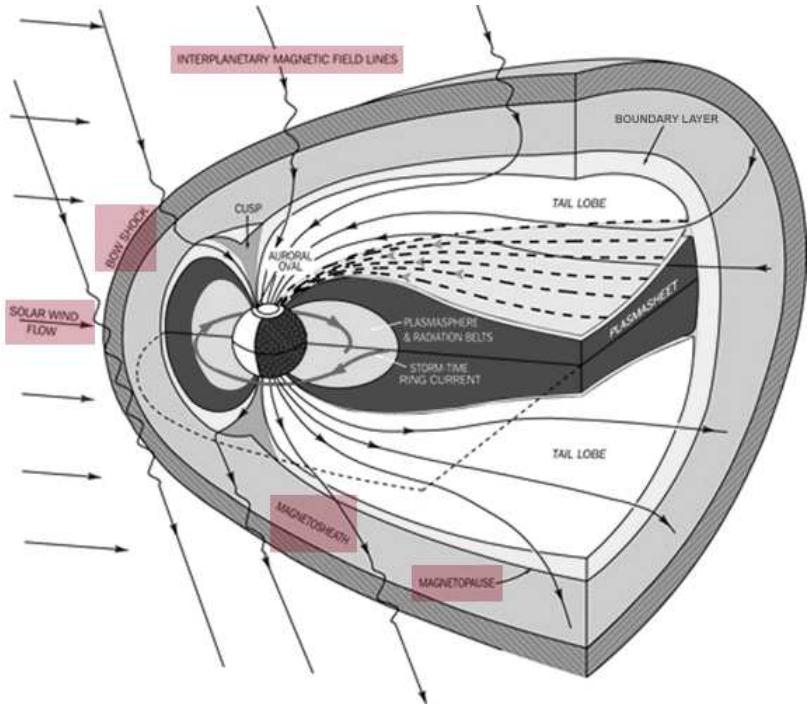

Fig. 1.1: A schematic showing the different regions of the earth's magnetosphere.

1.1 Magnetospheric Currents

The distortion of the earth's internal dipole field into the typical shape of a magnetosphere produced by the interaction with the solar wind is accompanied by electrical currents in the magnetosphere. The major currents in the magnetosphere are: (1) the magnetopause currents shielding earth's dipole and the ring current; (2) the symmetric ring current; (3) the cross-tail current along with the closure currents on the magnetopause; and (4) the partial ring current, which connects the Region 2 field-aligned currents. Figure 1.2 shows the various currents and their rough geographical locations inside the magnetosphere.

The four major current systems are shown again in fig. 1.3 (left). Note that each of the systems is closed. In fig. 1.3 (right), the magnetic disturbances produced by each of these basic current systems are sketched [2]. These currents systems are not only different topologically but have different origins which are briefly discussed in this section. The currents on the magnetopause are carried by the solar wind protons with the energy of about 1 keV. The component that shields earth's dipole is controlled by the solar wind

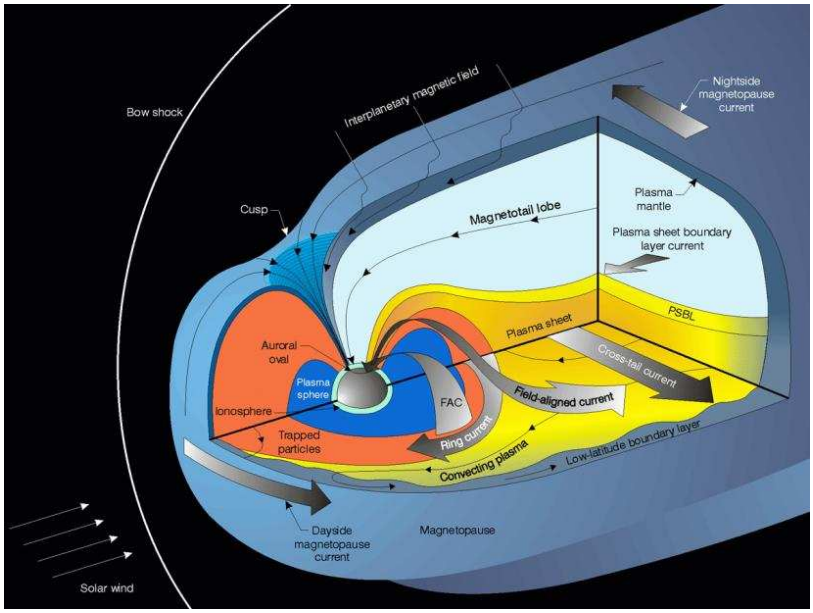

Fig. 1.2: A schematic showing the different magnetospheric currents.

dynamic pressure. The ring current is formed by the steadily trapped particles, mostly protons with the energy of 10-100 keV, the oxygen ions of an ionospheric origin being added during strong storm events [3]. The ground magnetic effect of the ring current is determined mainly by the total energy of the trapped particles. The carriers of the cross-tail current are temporarily trapped particles in the magnetospheric plasma sheet (the protons with the energy of 10 keV). The origin of the partial ring current is typically related to the charge separation in the course of the particle drift from the magnetospheric tail to the sun through the non-uniform magnetic field.

1.1.1 Magnetopause Current

Approaching a planet and its magnetosphere from interplanetary space, the first signature of its existence is the bow shock, a shock wave standing in the supersonic solar wind flow in front of the magnetosphere. Parameters like flow velocity, plasma density, and magnetic field all change significantly across the bow shock shown in fig. 1.1. According to Ampere's law, the jump in the magnetic field across the bow shock is associated with the magnetosheath current flowing in the bow shock region. The magnetopause separates

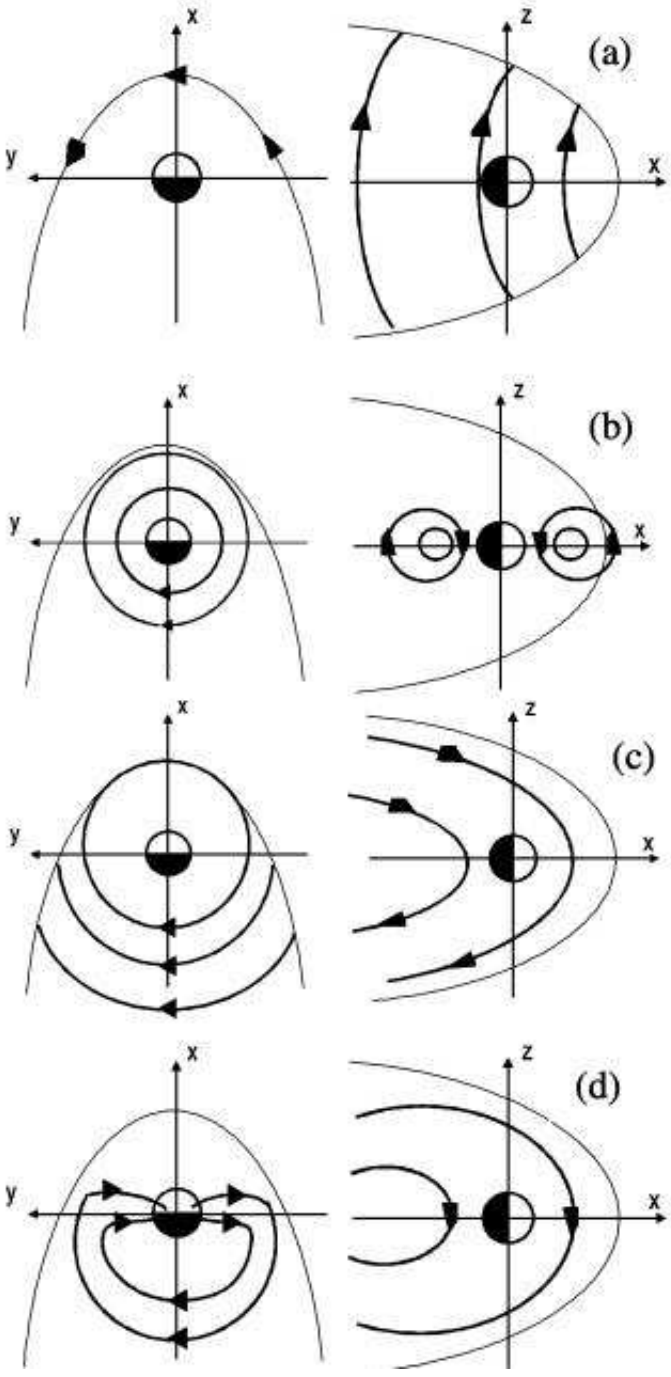

Fig. 1.3: Sketch of (left) the electric currents and (right) the associated magnetic disturbances for the four elementary current systems contributing to Dst. From top to bottom: the magnetopause currents shielding earth's dipole and the ring current, symmetric ring current, cross-tail current along with the closure currents on the magnetopause, and partial ring current closed to the Region 2 field-aligned currents.

the shocked solar wind, i.e., the magnetosheath plasma, from the magnetospheric magnetic field. Being a surface across which the magnetic field strength jumps from its low interplanetary value to the high magnetospheric field strength, the magnetopause represents a surface current layer.

The compression of the internal magnetic field on the dayside is associated with current flow across the magnetopause surface, the magnetopause current [4]. The magnetopause current (also called the Chapman-Ferraro current) is the current system flowing around the magnetopause as shown in fig. 1.4 (top) [5]. This current system generates a magnetic field that "prevents" the terrestrial dipole field from penetrating into the solar wind [6]. Figure 1.4 (bottom) shows an overview of the MP currents using the assumptions that the currents are predominantly determined by the magnetospheric field adjacent to the magnetopause boundary [7]. The magnetopause current is largely perpendicular to the geomagnetic field if the magnetic field outside the magnetosphere is small.

The currents on the dayside magnetopause close through the tail magnetopause. In the magnetotail, the northern and the southern lobes are separated by a cross-tail current layer. This current also closes over the tail magnetopause. A word of caution is needed with respect to this concept of current closure. Although $\nabla.\mathbf{j} = 0$ a particular current line will in general not close in the simplistic way indicated in fig. 1.4 (bottom). Currents do not originate in from some dipole as magnetic field lines and are generated locally. Thus, any particular current line may be highly complicated and will in general not close in a simple way into itself. There is also no simple concept like a frozen-in condition applicable to current density. Currents are not bound to a particle plasma element.

These currents can be derived from the single-fluid MHD equations. Neglecting the effects of gravity, the steady-state continuity and momentum equations can be written as [6]:

$$\begin{aligned} \nabla.(\rho_m \mathbf{u}) &= 0, \\ (\rho_m \mathbf{u}.\nabla)\mathbf{u} + \nabla p - \mathbf{j} \times \mathbf{B} &= 0. \end{aligned} \tag{1.1}$$

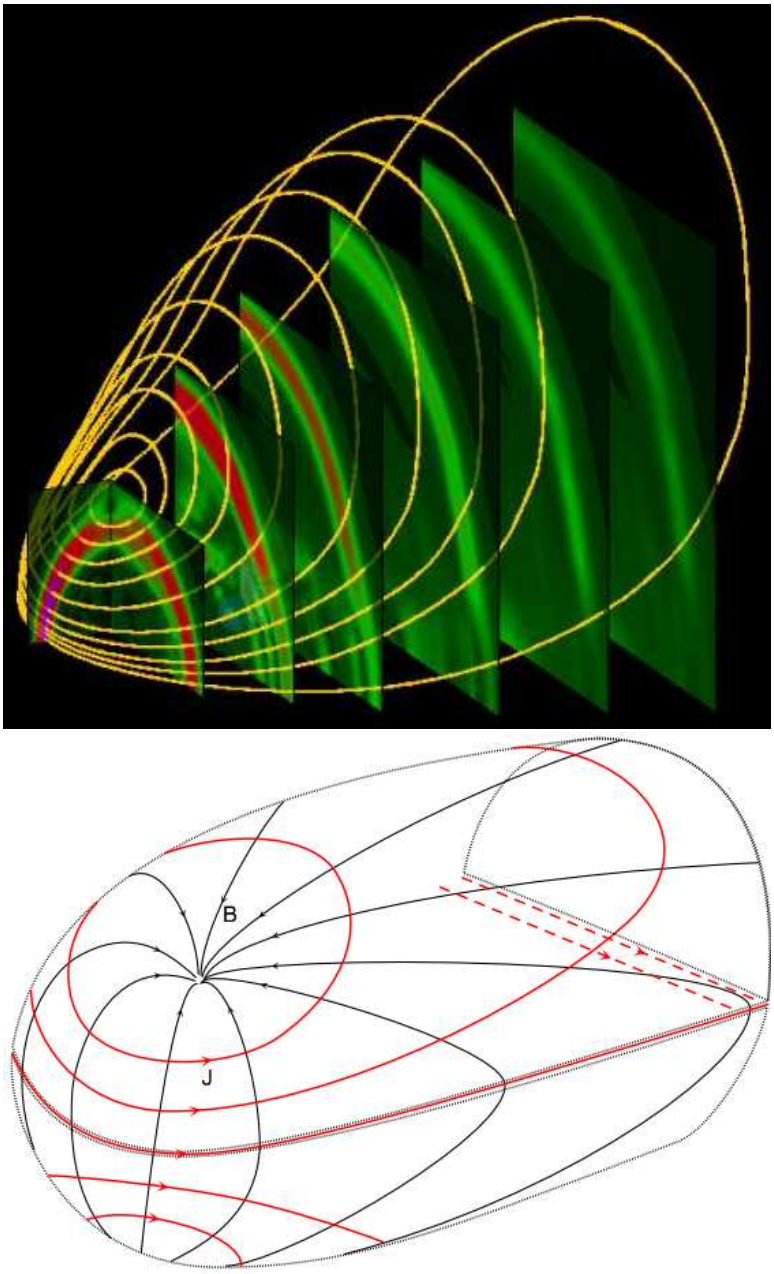

Fig. 1.4: Top. A Simulation result showing the configuration of the magnetopause current. Bottom. A sketch of the magnetopause currents and the associated magnetic field.

With the help of the continuity equation, the momentum equation can be written as:

$$\nabla(\rho_m u^2 + p) = \mathbf{j} \times \mathbf{B}. \tag{1.2}$$

In the simplest model of the magnetopause current system one neglects the magnetic field outside the magnetopause and the contribution of particles inside it. In other words, the magnetopause current system separates the shocked magnetosheath plasma from the "empty" magnetic dipole field inside. In this model the current density is given by:

$$\mathbf{j}_{MP} = \frac{\mathbf{B}_{dp}}{B_{dp}^2} \times \nabla(\rho_m u^2 + p), \tag{1.3}$$

where B_{dp} is the magnetospheric field at the magnetopause. The total pressure (ram pressure plus thermal pressure) in the magnetosheath is approximately equal to the free streaming solar wind kinetic pressure. Therefore, one can estimate the magnitude of the magnetopause current as:

$$j_{MP} = \frac{1}{B_{dp}} \frac{\rho_{m_{sw}} u_{sw}^2}{\Delta}, \tag{1.4}$$

where Δ is the thickness of the magnetopause.

The magnetopause can be considered as a boundary separating a vacuum magnetic field from a plasma. As a good approximation, the pressure in the magnetosphere, which is mainly magnetic pressure, must match the pressure in the magnetosheath, which is a combination of thermal plus magnetic pressures. The magnetosheath pressure is in turn determined by the solar wind momentum flux or dynamic pressure. The dominant pressure terms in the solar wind and at the nose of the magnetosphere are in approximate equilibrium:

$$\rho_{sw} u_{sw}^2 = B_{ms}^2 / 2\mu_0, \tag{1.5}$$

where the subscripts sw and ms refer to solar wind and magnetosphere. This expression can be used to calculate the B-field due to the magnetopause currents (assuming that the

B-field pressure at the magnetopause is the same as in magnetosheath.)

An alternative viewpoint to understand the origin of this current is from the perspective of the motion of particles in electromagnetic fields. Considering a simple boundary between a plasma and a magnetic field, called a Chapman-Ferraro layer as shown in fig. 1.5 [8]. Assuming only a cold beam of electrons and ions on the left and a uniform magnetic field on the right. In reality, boundary between an unmagnetized plasma and a vacuum magnetic field could occur only with a thermal distribution of particles instead of a cold beam on the left side of the boundary [9].

When an unmagnetized proton and electron begin to penetrate the boundary, they sense a $\mathbf{u} \times \mathbf{B}$ Lorentz force, which causes them to gyrate. After half an orbit they exit the boundary, moving anti parallel to the solar wind flow, as shown in fig. 1.5. in performing the half orbit, the proton moves $2\rho_{cp}$ down the page, and the electron moves twice the electron gyroradius, ρ_{ce}, up the page, giving rise to a current. As the inertia of the protons carries them much farther that the electrons, their motion constitutes most of the current. However, in a more realistic situation, the greater thermal velocity of the electrons would partially offset their smaller mass. The strength of the current can be computed by considering the number of protons protons that cross some particular x-z plane, say $y = y_0$. Any proton entering the boundary over a region $2\rho_{cp}$ wide will cross the $y = y_0$ plane. The flux of protons that encounters the section of the boundary is $2\rho_{cp}nu$ per unit length in the z-direction, where the subscripts SW have been dropped. As each proton carries a charge e, the current crossing $y = y_0$ per unit length in z is

$$I = 2\rho_{cp}nue = \frac{2nm_p}{B_z}u^2, \tag{1.6}$$

where we have used $\rho_{cp} = um_p/eB_z$. In a self-consistent treatment, the magnetic field would be modified by the currents carried by the electrons and protons, so that the gyroradius would not be given in terms of the unperturbed field. Now applying Ampere's law across the boundary and noting that $I = \int j dx$, we get

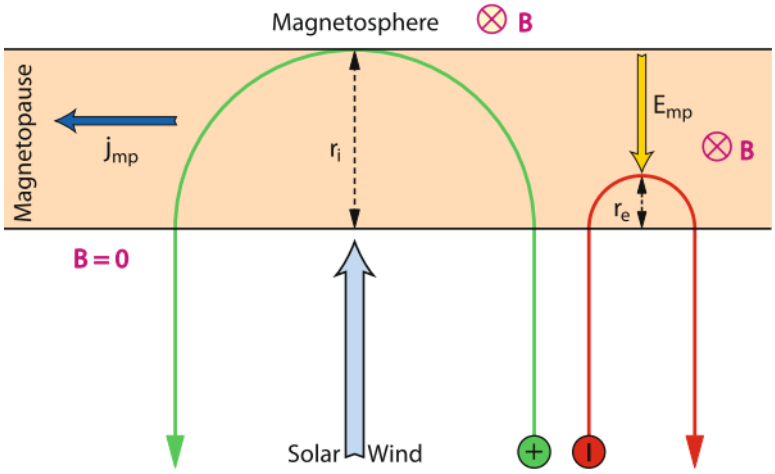

Fig. 1.5: Specular reflection off a magnetopause.

$$B_z = \mu_0 I. \tag{1.7}$$

Combining (1.6) and (1.7), we get

$$\frac{B_z^2}{2\mu_0} = nm_p u^2 = \rho_{sw} u_{sw}^2, \tag{1.8}$$

which brings us back to the pressure balance criterion. This current must provide the $\mathbf{j} \times \mathbf{B}$ force integrated across the boundary needed to balance the rate of change of solar wind momentum or to divert the solar wind flow. The momentum flux into the boundary is $2\rho_{sw} u_{sw}^2$, where the factor 2 comes from the fact that in our picture the plasma is perfectly cold, so that the velocity is $2u$. Equating these gives

$$2\rho_{sw} u_{sw}^2 = |\mathbf{I} \times \mathbf{B}| = B^2/mu_0, \tag{1.9}$$

which is the same as (1.5). This current provides an additional magnetic field, which compresses the magnetospheric field in the magnetosphere and at the same time annihilates its external part. It is a diamagnetic current caused by the perpendicular density gradient at the magnetopause.

The effect of the magnetopause current is felt at the earth's surface. When a sudden increase in solar-wind dynamic pressure, as is often follows the passage of an interplanetary shock, reaches the earth, the magnetosphere is compressed; the magnetopause moves nearer the earth, and at the same time the magnetopause current intensifies. The movement and intensification of the current are sensed at the earth's surface as a sudden increase in the geomagnetic-field intensity of a few tens of nanotesla. This feature is known as a sudden impulse (SI) or a sudden storm commencement (SSC) if a geomagnetic storm follows. This excursion is the magnetic signature of the solar wind impinging faster than usual onto the magnetopause. The position of the dayside magnetopause is essentially determined as the surface of equilibrium between the magnetic pressure of the terrestrial magnetic field and the kinetic pressure of the solar wind. Whenever the speed of the solar wind increases, the terrestrial field is compressed and the magnetopause recedes to a new equilibrium position.

1.1.2 Ring Current

The earth's ring current is a westward flowing toroidal electric current around the earth, centered at the equatorial plane and at altitudes of $1.5R_E$ to $7R_E$. Enhancements in this current are responsible for global decreases in the earth's surface magnetic field, which have been used to define geomagnetic storms.

This current produces a magnetic field in opposition to the earth's magnetic field and so an earthly observer would observe a decrease in the magnetic field in this area. It is generally accepted that the ring current is formed partially from ions with direct convective access to low L values and partially from higher energy ions on closed drift paths diffusing in under the influence of fluctuating electric and magnetic fields [10]. Ions in the energy range 10-200 keV are responsible for the majority of the ring current energy content [11], most of the ring current forms through convective transport from the inner plasma sheet.

The lowest order motion of charged particles in the magnetosphere is gyration combined with parallel drift. For the case of non-time-varying fields, and a weak electric field, the higher order corrections to the motion of charged particles consist of a combination of $\mathbf{E}\times\mathbf{B}$ drift, grad- drift, and curvature drift:

$$\mathbf{v_{1\perp}} = \frac{\mathbf{E}\times\mathbf{B}}{B^2} - \frac{|m|}{q}\frac{\nabla B\times\mathbf{B}}{B^2} - \frac{2W_{||}}{qB^4}[(\mathbf{B}.\nabla)\mathbf{B}]\times\mathbf{B}. \tag{1.10}$$

$\mathbf{E}\times\mathbf{B}$ motion merely gives rise to the convection of plasma within the magnetosphere, without generating a current. By contrast, there is a net current associated with grad- drift and curvature drift, the different drifts are shown schematically in fig. 1.6.

During geomagnetic storms, ring current particle fluxes are dramatically increased, with the peak enhancements occurring in the inner ring current (at$L < 4$). The quiet-time ring current consists predominantly of H+, while the storm-time ring current also contains a significant component of ionospheric O+, whose contribution to ring current energy density may even exceed that of H+ for brief periods near the maximum of particularly intense storms. The formation of the storm-time ring current has been attributed to two different processes: 1) the injection of plasma into the inner magnetosphere during the expansion phase of magnetospheric substorms and 2) increased convective transport of charged particles from the nightside plasma sheet deep ($L < 4$) into the inner magnetosphere as a result of an intensification of the earth's dawn-dusk convection electric field during extended periods of strong southward IMF.

The storm-time growth of the ring current lasts from 3 to 12 hours and constitutes the "main phase" of a magnetic storm. Following this main phase, the ring current begins to decay, returning to its pre-storm state in two to three days. Full recovery can require as long as a month in the case of major geomagnetic storms. During the storm recovery phase, particle transport into the ring current slows, allowing various loss processes to reduce ring current particle fluxes to their quiet-time level. The primary loss process during both the main and recovery phases is charge exchange with neutral hydrogen atoms in the geocorona. In this process, a singly charged energetic ion trapped on a geomagnetic field line collides with a geocoronal neutral hydrogen atom and acquires its electron. Fast initial ring current decay is caused by dayside outflow of particles on open field lines through the magnetopause (fast flow-out losses) and are controlled by the decreased convection electric field.

A second loss process, affecting principally low-energy ($10-30$ keV) ring current ions,

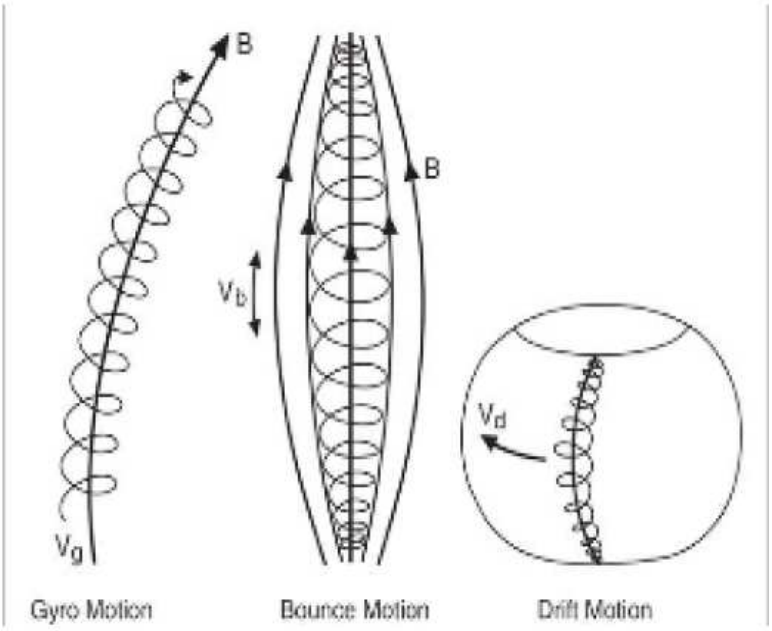

Fig. 1.6: A schematic showing the different drifts that a particle experiences in the earth's magnetic field.

involves Coulomb collisions with the thermal ("cold," 1 eV) plasma of the plasmasphere. Collisions with plasmaspheric electrons result in the energy degradation of ring current ions and the formation of a population of low-energy (< 500eV) ions inside the plasmasphere. In addition to their role in ring current energy decay, coulomb collisions between the ring current ions and the plasmasphere have important plasmaspheric and ionospheric effects, heating the plasmasphere and providing the major energy source for stable auroral red (SAR) arcs (broad diffuse bands of atomic oxygen emissions at 630 nm occurring during the storm recovery phase in the mid-latitude ionosphere). The third process thought to contribute to ring current decay is the precipitative loss of ring current particles into the atmosphere as a result of wave-particle interactions. The role of this loss process in the evolution of the ring current is still not well understood and is the subject of ongoing research.

The ring current is a dynamic system with a complex structure that varies with local time, radial distance, and storm phase. A pronounced noon-midnight asymmetry exists

during injection, for example, and other asymmetries in the particle distributions become evident as the ring current grows and decays. The variable structure of the ring current results from differences in the drift velocities of the trapped particles and in their susceptibility to particular loss processes, both of which, in turn, depend upon the ion species involved and its energy and pitch-angle distributions.

Measurement of the ring current intensity can be done through in-situ measurements by satellites, but these point measurements do not give a global picture of the ring current dynamics. Imaging techniques like the energetic neutral atom (ENA) imaging provide the opportunity to view the time variation of particle densities and intensities on a larger scale. The growth and recovery of the ring current are indicated by changes in the Dst (disturbance storm time) index, the geomagnetic index that serves as the standard measure of ring current activity.

1.1.3 Tail Current

The geomagnetic tail is the name given to the region of the earth's magnetosphere that stretches away from the sun behind the earth. The earth's field lines are dragged anti-sunward through tangential stresses between the solar wind and earth's magnetic field producing the magnetotail. The geomagnetic tail is the largest reservoir of plasma and energy in the magnetosphere. The energy and the plasma are released into the inner magnetosphere aperiodically during magnetically disturbed episodes called magnetic substorms. Magnetic tails are created by a tail current and it is customary to place this current in the neutral sheet. The configuration of this current must be such that when the magnetic field of this current and the principal magnetic field (a dipole for instance) are superposed, a magnetic tail geometry ensues. For earth's magnetotail, the current flows from dawn to dusk [9].

Besides the magnetopause current sheet, another typical example of a diamagnetic current is the neutral sheet current in the geomagnetic tail which divides the tail into northern and southern lobes with their stretched magnetic field lines as shown in fig. 1.2. The magnetic field in the north (south) lobe is directed toward (away from) the earth; hence

the need for a current sheet to separate these two regions of oppositely directed magnetic fields [4]. In the southern lobe the field lines extend from the southern polar cap and, in the earth's case, point antisunward, while in the northern lobe they come from the distant tail pointing sunward ion the terrestrial case and ending in the northern polar cap. This stretching of the otherwise approximately dipolar terrestrial magnetic field can be accounted for by a diamagnetic current flowing across the magnetospheric tail. The tail current sheet, or central plasma sheet (CPS) is a region of hot plasma which separates the anti-sunward and sunward magnetic fields in the geomagnetic tail lobes and flows in the same direction as the ring current in the midnight equatorial plane which reduces the magnetic field at the earth's surface.

The magnetotail current transports positive charges from one flank to the other (from dawn to dusk in the terrestrial case) and negative charges in the opposite direction across the tail and, because of its stationarity and its macroscopic magnetic effect, cannot be anything else but a diamagnetic current. Its cause is a gradient in the plasma pressure perpendicular to the current layer pointing from north to south in the upper (northern) half and from south to north in the lower (southern) half of the current layer. Hence, the current layer is a concentration of dense and hot plasma which is called the neutral sheet because of the weak magnetic field it contains.

The cross-tail current in the central plasma sheet closes on the magnetopause (fig. 1.7 (a)), such that the tail current forms a theta pattern when viewed along the sun-earth line as shown in fig. 1.7 (b). About 106 A of current is carried in each 5 RE section of the tail for total stored energy of 1015 J. The plasma in the geomagnetic tail has a structure similar to the laboratory theta-pinch with a plasma current of approximately 20 MA trapping a high pressure plasma sheet. The nonlinear structure is rather stable and continuous for energies on the order of W_{tail} $10^{15}J$. There must be a pressure equilibrium between the solar wind pressure, the magnetic pressure in the lobes, and the thermal plasma sheet pressure. The tail radius increases, or flares, as the distance down the tail increases and then reaches an asymptotic radius of around 30 RE at around 150 RE down the tail. However, the geometry

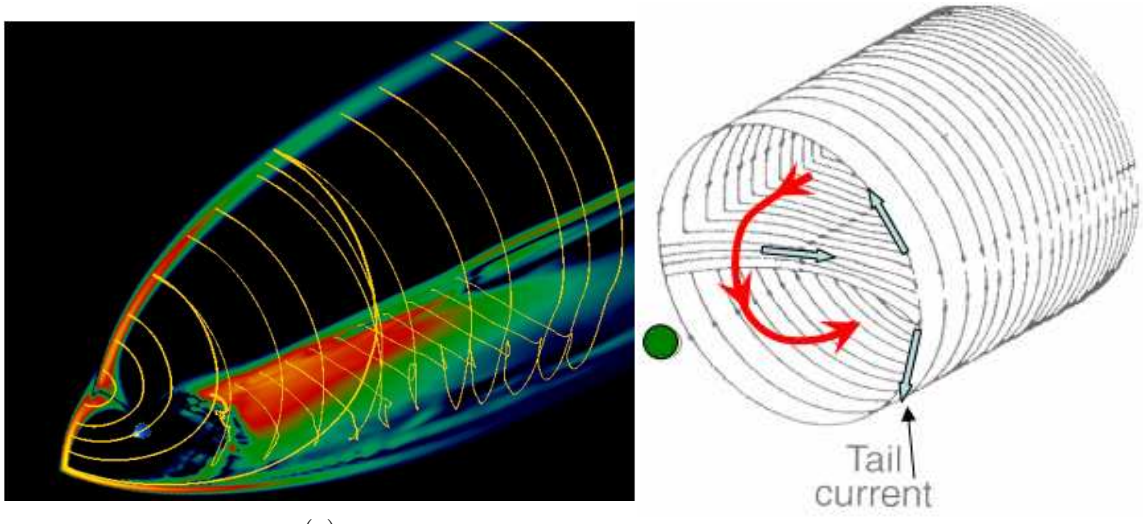

(a) (b)

Fig. 1.7: (a) Simulation result showing the configuration of the magnetotail current. (b) An illustration of the theta pattern of the tail current.

of the geomagnetic tail this distance down the tail is highly variable and dependent on solar wind conditions. The lunar orbit which is around 60 RE crosses the geomagnetic tail.

The current carried by the plasma sheet can be calculated by applying Ampere's law across the current sheet. The total change in magnetic field across the plasma sheet is twice the lobe field strength, because the fields on either side are equal in size but oppositely directed [9]. So

$$\Delta B = 2B_T = \mu_0 I, \tag{1.11}$$

where I is he sheet current density. Approximately $10^6 A$ is carried in each $5R_E$ of the length of the tail, which means that diversion of only a small part of the tail current is sufficient to explain the ionospheric auroral electrojet currents observed during substorms.

1.1.4 Field Aligned Currents (FACs) and Ionospheric Currents

Though a large fraction of these magnetospheric currents flow in closed loops (i.e., is divergence-free), some fraction of it may accumulate charges in specific regions, thus generating electric potential drops between different regions, or be connected to permanent sources of electric potential difference, like the solar wind when the planetary field is recon-

nected with interplanetary field lines. In such a situation, charge accumulation or existing potential drops generate electric current flows along conducting paths connecting regions of different potential. Such paths exist in planetary intrinsic magnetospheres: if magnetic field lines, which are near perfect conductors for cold ionospheric electrons, connect a region of (typically weak) charge accumulation to the planetary ionosphere, these field lines can carry the so called field aligned currents (FACs, also called Birkeland currents), which flow vertically along magnetic field lines and close horizontally through the ionospheric conductor (explained in next section) [4]. These field-aligned currents are of the utmost importance at high latitudes at earth and the giant planets, where near-vertical ionospheric field lines provide a direct electrical connection between the auroral ionosphere and distant magnetospheric regions as shown in fig. 1.8.

Field aligned currents $\mathbf{J}_{||}$ do not contribute to the electromagnetic stress because:

$$\mathbf{J} \times \mathbf{B} = 0. \tag{1.12}$$

Therefore, these currents are associated with a "force-free" magnetic configuration [12]. FACs provide means for coupling the magnetosphere and the ionosphere and they are also a source of visual auroras. The current density of earth's FACs is typically a few tens of micro-amperes/m^2 during a moderate-sized auroral event.

One frequent (if not systematic) visible manifestation of these field-aligned current flows is the generation of intense auroral emissions. The magnetic field associated with the field-aligned currents were first detected in 1966 by a satellite-borne magnetometer flown through an aurora. Indeed, in magnetospheric regions where the density is low, the reservoir of free current-carrying electrons is limited, and the mirror force along converging field lines limits the access of electrons to the ionosphere, upward current flow along field lines requires the generation of limited voltage drops along field lines. The current-carrying electrons are thus accelerated along their guiding field line and precipitated into the ionosphere, where they produce an aurora. For this reason, auroral displays at the various planets are a good first-order tracer of the ionospheric roots of upward field-aligned currents.

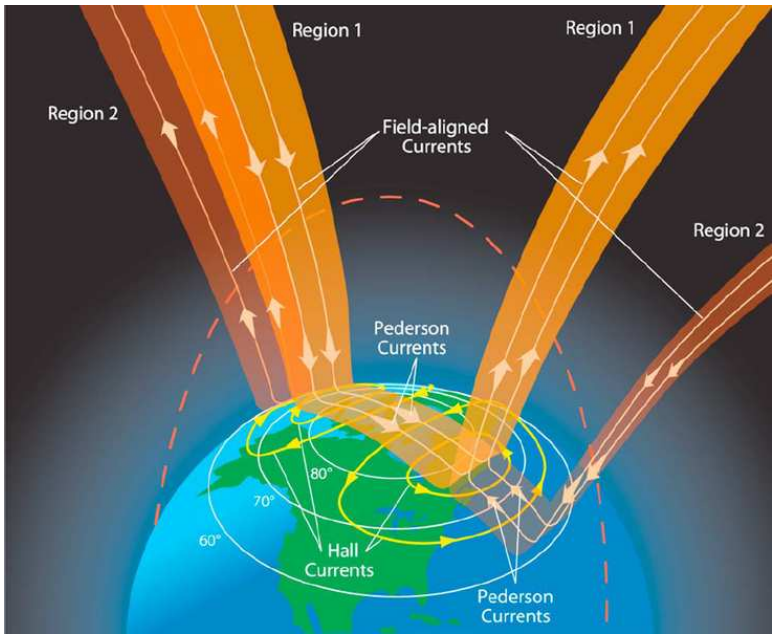

Fig. 1.8: A schematic showing the different ionospheric and field-aligned currents.

Ionospheric Currents

Ionospheric currents flow in a narrow horizontal layer at an altitude between 100 and 150 Km concentric with earth's surface. Ionospheric currents are observed during both quiet and disturbed solar wind conditions. The quiet ionospheric currents, designated as S_q currents, are produced by the motion of the ionized ionospheric particles across the planetary magnetic field [12]. This motion, driven by the daily heating of the ionosphere by the sun and the lunar and solar tidal forces, induces an electromotive force that produces an equivalent current pattern that is fixed with respect to the sun. A diurnal variation of the geomagnetic field is observed by a magnetic station fixed on earth and rotating through this current system.

The disturbed ionospheric currents, designated as S_D, are observed in conjunction with the auroral activity at northern magnetic latitudes. During an aurora, an excess of 10^{19} ergs of particle energy is deposited into the auroral ionosphere. The auroral ionospheric conductivity thus becomes greatly enhanced and ionospheric currents flow in both eastward and westward directions. These currents are referred to as the westward and westward

electrojets. the intensity of these electrojets is several million amperes for a moderately sized aurora. These currents cause a deviation of several hundred nanoteslas of earth's main magnetic field on the surface of the planet.

The partially ionized plasma present in a planet's ionosphere can exhibit a differential motion of ions and electrons and thus a current, under the effect of the existence of a large scale electric field in the rest frame of the neutral gas. This is due to the resistivity existing in the gas in the presence of collisions. Indeed, at certain ionospheric altitudes, the ions and, to a lesser degree, also the electrons are coupled by collisions to the neutral components of the upper atmosphere and follow their dynamics [4]. When the atmosphere is magnetized, atmospheric winds and tidal oscillations of the atmosphere force the ion component to move across the magnetic field lines, while the electrons move much more slowly at right angles to both the field and the neutral wind. This relative movement constitutes an additional electric current driven by the neutral wind, and such a region bears the name dynamo layer, the generator of which is the atmospheric wind motion as shown in fig. 1.9.

In the presence of collisions between charged and neutral particles the momentum equation becomes:

$$m\frac{d\mathbf{v}}{dt} = q(\mathbf{E} + \mathbf{v} \times \mathbf{B}) - m\nu_n\mathbf{v}. \tag{1.13}$$

The collisional term on the right-hand side describes the momentum lost through collisions with neutrals occurring at a frequency ν_n. It is often called frictional term since it impedes motion. An important point is that the electric field $\mathbf{E}'$ is the electric field measured in the centre-of-mass frame of the system, in other words more or less exactly in the rest frame of the neutral gas (for a weakly ionized gas as we have in the upper atmosphere-ionosphere).

The friction term introduces a differential motion between electrons and ions and thus a current, even in homogeneous magnetic fields. The dense regions of the ionosphere (the D, E, and F regions) contain significant concentrations of free electrons and ions. The presence of mobile charges makes the ionosphere highly conducting [6]. A natural consequence of the high conductivity is that electric currents can be generated in the ionosphere by various

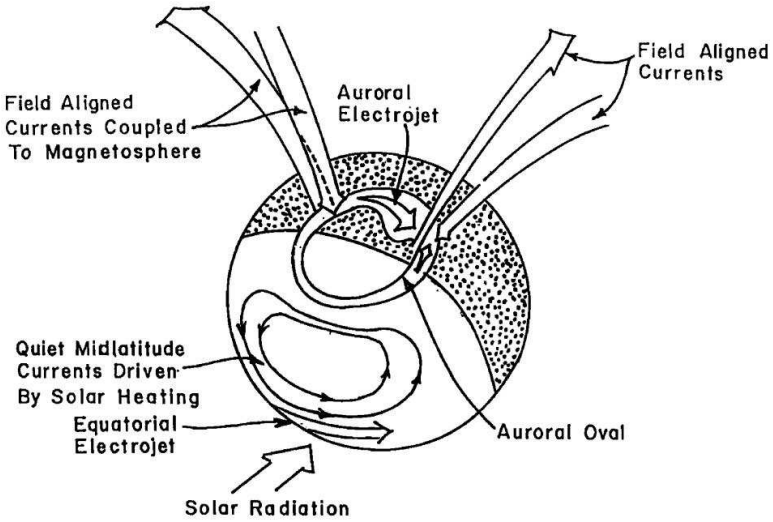

Fig. 1.9: Schematic diagram of the field aligned electric currents flowing in the ionosphere/inner magnetosphere. These field-aligned currents couple the auroral oval with the outer magnetosphere and are also responsible for sustaining the auroral electrojets. The solar quite current system and the equatorial electrojet current system are also shown.

physical processes. These current systems can be quite complicated, because not only is the ionosphere a conduct ing medium, but it is also collisional, and it is penetrated by a strong magnetic field. The ionospheric current system can be described with the help of a few simplified equations. The current is given by the generalized Ohm's law:

$$\mathbf{j} = \sigma.(\mathbf{E} + \times\mathbf{B}). \tag{1.14}$$

In fact, when abundant collisions between the ionized and the neutral part of an upper atmosphere interrupt the cyclotron motion of electrons and/or ions the above equation reduces to an anisotropic Ohm's law:

$$\mathbf{j} = \sigma_{||}\mathbf{E}_{||} + \sigma_p\mathbf{E}'_{\perp} - \sigma_h(\mathbf{E}'_{\perp} \times \mathbf{B})/B. \tag{1.15}$$

The Hall conductivity, σ_H, determines the Hall current in the direction perpendicular to both the electric and magnetic field. The Hall conductivity maximizes at a height where the ions collide so frequently with the neutrals that they are essentially at rest, while the

electrons already undergo a somewhat impeded $\mathbf{E} \times \mathbf{B}$ drift. The Pedersen conductivity, σ_p, governs the Pedersen current in the direction of that part of the electric field, $\mathbf{E}'_{\perp}$, which is transverse to the magnetic field. The Pedersen conductivity maximizes typically at a somewhat higher altitude than the Hall conductivity, namely where the ions are scattered in the direction of the electric field before they can start to gyrate about the magnetic field. The quantity $\sigma_{||}$ is called the parallel conductivity since it governs the magnetic field-aligned current driven by the parallel electric field component, $E_{||}$.

Figure 1.10 shows the altitude variation of the three conductivity components. It is interesting to see that above a few hundred kilometers the specific conductivity σ_o becomes nearly independent of altitude, because the n Q nearly cancels with the density factor in the collision frequencies. The near constancy of the specific conductivity is an important factor in understanding ionospheric current systems. The Hall conductivity falls off very rapidly, and it is important only in the D and E regions.

1.2 Magnetospheric Indices

Geomagnetic indices are a measure of geomagnetic activity, which is a signature of the response of the earth's magnetosphere and ionosphere to solar forcing. They play a significant role in describing the magnetic configuration of the earth's ionized environment. Various different indices have been proposed which represent some region or phenomenon in the magnetosphere-ionosphere system. In this section we discuss the indices most used during the course of this work.

1.2.1 Dst Index

The disturbance storm time (Dst) index has been widely used as an indicator of geomagnetic activity. Dst* which is obtained after removing the contributions from magnetopause currents, induced currents on the conducting earth, and the quiet time ring current is assumed to represent the ring current (RC) intensity. Dst* is calculated using the following

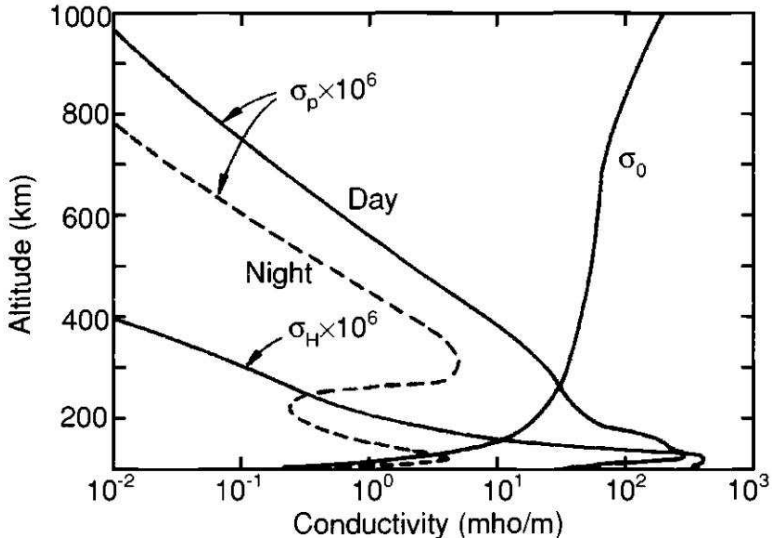

Fig. 1.10: Typical conductivity values in the midlatitude daytime ionosphere.

expression [13]:

$$Dst* = \frac{Dst - Dmp + Dqrc}{C_{IC}}, \tag{1.16}$$

where C_{IC} is a correction factor due to induced currents in the earth, taken to be 1.3, D_{MP} is the perturbation from the Chapman-Ferraro currents on the magnetopause, taken to be $15.5 * \sqrt{Psw}$ (solar wind dynamic pressure in nPa), and D_{QRC} is the contribution from the quiet time ring current (subtracted out as a baseline offset of Dst), taken to be -20 nT [13, 14]. O' Brien and McPherron suggest coefficients that are slightly different values, but the results obtained do not differ much qualitatively [15]. The ring current particles are energized during a geomagnetic storm which is reflected by corresponding decrease in the Dst index. The decay time of the particles is important because the injection rate can not be determined without the knowledge of this parameter.

The Dst index is derived from measurements made at four magnetic observatories, Hermanus, Kakioka, Honolulu, and San Juan. These observatories were chosen on the basis of the quality of observation and for the reason that their locations are sufficiently distant from the auroral and equatorial electrojets and that they are distributed in longitude as evenly as possible. The observatories are within $-35°$ to $+35°$ latitude, a map of the network

is given in fig. 1.11. By removing the earth's magnetic field contribution, and normal daily variations, magnetic disturbances can be determined.

The Dst index represents the axially symmetric disturbance magnetic field at the dipole equator on the earth's surface. Major disturbances in Dst are negative, namely decreases in the geomagnetic field. These field decreases are produced mainly by the equatorial ring current system in the magnetosphere. The neutral sheet current flowing across the magnetospheric tail makes a small contribution to the field decreases near the earth. Positive variations in Dst are mostly caused by the compression of the magnetosphere from solar wind pressure increases [16].

The main problem with magnetometer-derived Dst information is that magnetometers cannot distinguish between the different current systems (ring current, tail current, field-aligned currents, magnetopause current, and ground-induced currents). The resolution of the Dst index is low as the values are given every hour. In addition, different authors have different methods to remove the quiet time values of the ring current. Similar, but higher resolution indices have been proposed, like the $SymH$ and the USGS $SymH$. The use of magnetometer data to characterize the ring current asymmetry could also be problematic. The asymmetry index ($ASymH$) uses data from the two stations that happen to measure the minimum and maximum disturbance. If those two stations are longitudinally near each other, it may lead to a misleading global view.

1.2.2 AL Index

The Auroral-electrojet (AE) index was originally introduced by Davis and Sugiura (1966) as a measure of global electrojet activity in the auroral zone. The AE index is derived from geomagnetic variations in the horizontal component H observed at 12 selected observatories along the auroral zone in the northern hemisphere. The technique for calculating them can be understood by reference to fig. 1.12. The third set of traces in this diagram displays the H-component traces from a worldwide chain of auroral-zone magnetic observatories [9]. Monthly mean values are subtracted from each station's trace to give a base value of zero. The traces are then plotted with respect to a common baseline, and

Fig. 1.11: Geographic locations of the four magnetometer stations, data from whom are used in calculating Dst index.

upper and lower envelopes are calculated. The AU (auroral upper) index is defined any instant of time as the maximum positive disturbance recorded by any station in the chain. Similarly, AL is defined as the minimum disturbance defined by the lower envelope. If the disturbances were caused by an infinite sheet of current, the AU and AL would be proportional to the maximum overhead current density in the two electrojets. A single measure that approximated the total effect of both electrojets is defined as $AE = AU - AL$. For completeness, AO is the defined as the average of AU and AL: $AO = (AU + AL)/2$.

The magnitude of AL is a good indicator of the strength of a substorm. And yet its usage has been severely constrained. Partly this is because of the slowness of distribution of high time resolution AL data (or even, at times, limited distribution). But it is widely suspected that there may be uncertainties which arise from the limited number of geomagnetic stations (12) involved in creating the traditional indices. Historically, the indices have been used as an indicator of auroral electrojet activity, and thereby the magnetospheric activity. The auroral electrojet indices are scalar values, which indicate the maximum perturbation measured at one of the AE station locations. Hence, they are local indices, and measure

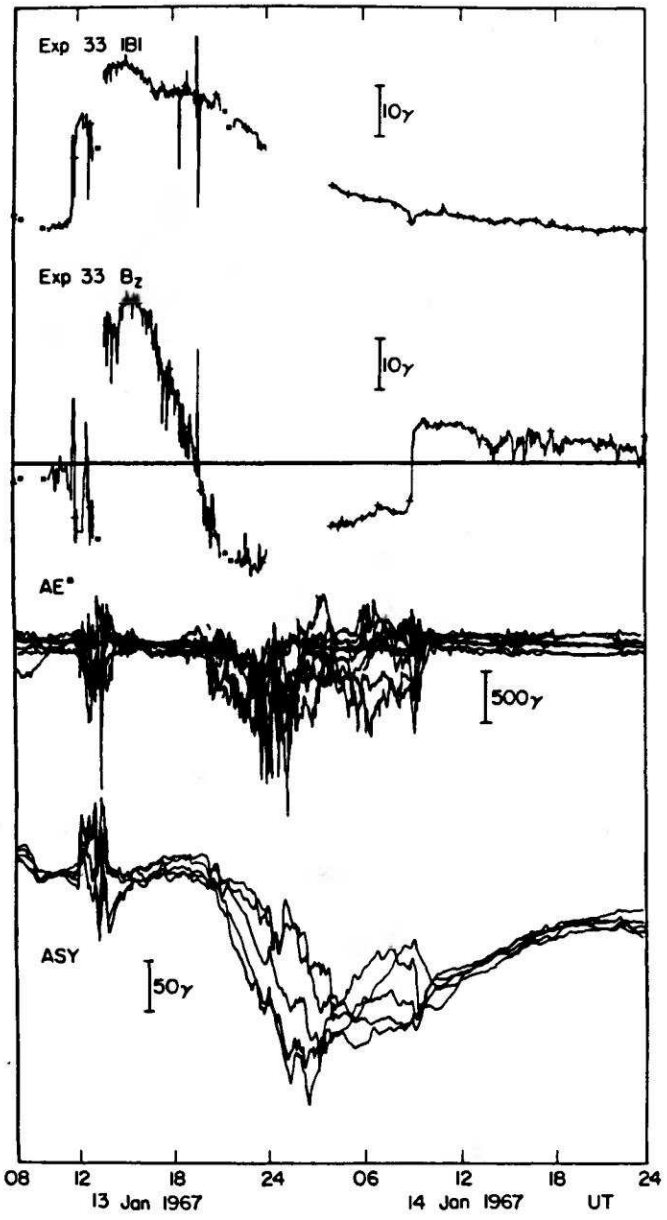

Fig. 1.12: Illustration showing the type of data used to create the auroral-electrojet indices (AU, AL, AO, AE) and the disturbance storm time and asymmetry indices (Dst, Asym). AU is the upper envelope of auroral zone deviation of H (third panel, labeled AE) from a reference value; AL is the lower envelope, AP is the average, and AE is the separation of envelopes. At mid latitudes, Dst and Asym are, respectively, the average deviation of H from a quiet day and the separation of the upper and lower envelopes (bottom panel, labeled ASY). The top two traces show that magnetic activity is produced by a strong interplanetary magnetic field pointing southward ($Bz < 0$) and parallel to the earth's dipole axis.

global electrojet activity only to the extent that station coverage is global. The current AE network consists of 12 stations strategically placed around the globe to minimize these limitations. Newell and Gjerloev have derived a similar index SML (100) based on data from 100 high latitude station instead of the 12 traditionally used, as shown in fig. 1.13 (left) [17].

Figure 1.13 (right) shows the AL (12) and SML indices during a 4 h period including the onset time. A series of auroral brightenings and fadings occurred prior to onset, including a pseudo-onset at 07:53 UT [17] . However, the onset time identified from the Polar UVI substorm database, namely 08:41 UT, is observed only be SML. It is clear that the absence of an AL(12) station beneath the auroral bulge, as shown in fig. 1.13 (left) results in virtually no detection of the sharp and sustained increase in auroral brightness at 08:41 UT. There is independent verification that, in this case at least, AL(12) does not perform nearly as well as SML is identifying substorms.

1.2.3 B2i and IB

The ion isotropy boundary (IB) is a magnetic field-aligned surface stretching between the northern and southern hemispheres. It demarks the low-latitude boundary between regions in the magnetosphere where ions (protons) exhibit adiabatic and non-adiabatic behaviour. In the former region, ions bounce back and forth, stably trapped between mirror points. In the latter region, pitch-angle scattering mechanisms cause the ions to fall into the down-going loss cone. Ions in the loss cone precipitate in the earth's upper atmosphere and produce the proton aurora. Equatorward of this region, the loss cone remains empty and there is essentially no proton precipitation.

In the literature, in situ and remote-sensing techniques have been used to identify where the transition between these two regions occurs. As a result, the nomenclature used to describe this boundary reflects the method used to detect it. Sergeev and co-workers [18,19] used precipitating (directed radially downward) and trapped (perpendicular to the radial direction) ion flux data taken with NOAA spacecraft to identify the location of the boundary. There is a low-latitude transition between a region where ion flux distributions change from

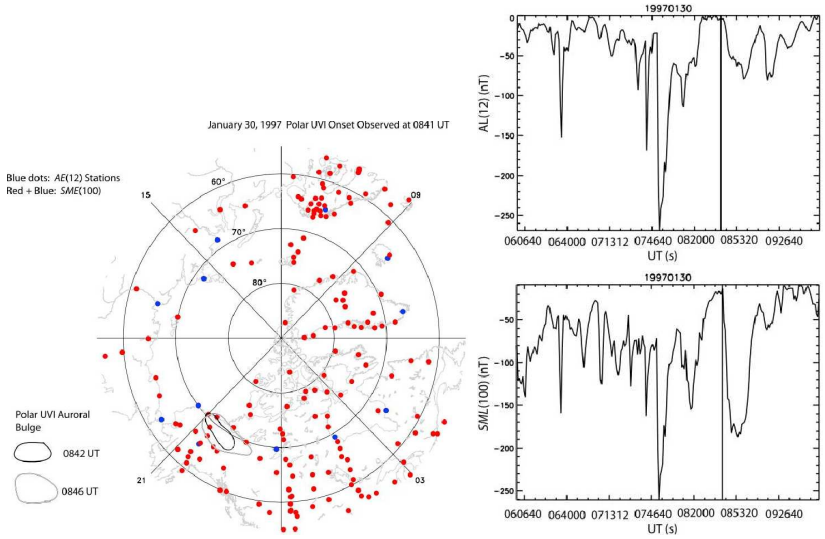

Fig. 1.13: Left. The geomagnetic stations used for AL(12) and for SML(100), with the ionosphere appropriate to 30 January 1997 at 0841 UT, when a substorm onset was observed by Polar UVI. The location of the onset auroral bulge is drawn for two epochs. Note that no AL(12) stations lay beneath the onset bulge. Right. Following a series of brightenings and fadings, Polar UVI observed a sustained auroral breakup and expansion at 31,283 s of 30 January 1997 (vertical line). The substorm can be identified in the SML(100) data just 37 s later, while the traditional AL(12) does not pick up the actual onset.

being isotropic to anisotropic over all pitch-angles, outside of the up-going loss cone. V. Sergeev and B. Gvozdevsky [19] defined the ion isotropy boundary (IB) to be the location at which the ratio of precipitating to trapped flux dropped from approximately 1.0, as the spacecraft flew towards the equator.

The pitch angle distribution of particles on closed field lines may display a strong flux depletion in the loss cone due to collisions in the ionosphere. In particular, when observing the down going particles at low altitudes above the ionospheric loss region, the relative amount of particles inside the loss cone can be used to measure the amount of pitch angle scaterring during one bounce between the opposite mirror points [18] . In the absence of wave particle interaction, the depleted loss cone will be conserved for adiabatically moving particles. However, possible nonadiabaticity or stochastization of particle motion will lead to the filling of the loss cone. For those particle that mirror at low altitudes (having small equatorial pitch angles), the deviations from adiabatic motion are strongest at the equator in the central current sheet. Adiabaticity is primarily controlled by the equatorial value of

the ratio R_c/ρ, where R_c is the curvature radius of the field line, $\rho = mV_c/eB_z = G/B_z$ is the effective particle gyroradius, V is the total particle velocity, and G is particle rigidity.

As shown in fig. 1.14, due to the monotonic decrease of equatorial B_z with a distance into the tail, the closed field line region is divided in two parts. The inner part corresponds to the adiabatic case where the depleted loss cone is conserved. In the outer part the loss cone is refilled because of stochastic particle motion when crossing the equatorial current sheet. The boundary between these regions with different types of particle dynamics at the equator is always valid for protons due to the high threshold B_z value (see fig. 1.14(b)).

Because of the much lower rigidity of electrons, the corresponding threshold B_z values for electron IB are lower and the boundaries are in a magnetic field region mainly controlled by the tail current. The monotonic decrease of the radial B_z profile may not necessarily be valid in this region since the redistribution and filamentation of the tail current and other dynamic phenomena like plasmoids may generate bumps and gaps in this profile. In such a case, as schematically shown by the dashed line in fig. 1.14(b), there may be a few detached isotropic precipitation regions. As a result of such possible structures and time variability of B_z, the pattern and latitudinal position of the isotropic boundary is expected to be more variable for electrons than for protons.

The low-altitude polar spacecraft crossing the auroral zone generally detect a fairly simple pattern of the energetic proton precipitation as shown in fig. 1.15. It includes a region of isotropic precipitation with a well-defined equatorward boundary (IB) [20]. This boundary is rather sharp, only few tenths of degree in latitude, and is ordered in space in a very systematic way: particles of higher energy/mass have their lBs at lower invariant latitudes. The physics of the isotropic boundary can be explained by a mechanism of particle scattering in the regular magnetic field (not by turbulence). Energetic particles bouncing between their mirror points at low altitudes are effectively scattered in pitch angle and fill the loss cone when crossing the equator if the following condition is valid at the equator:

$$R_c/\rho = B_z^2(GdB_x/dz)^{-1} \leq 8. \tag{1.17}$$

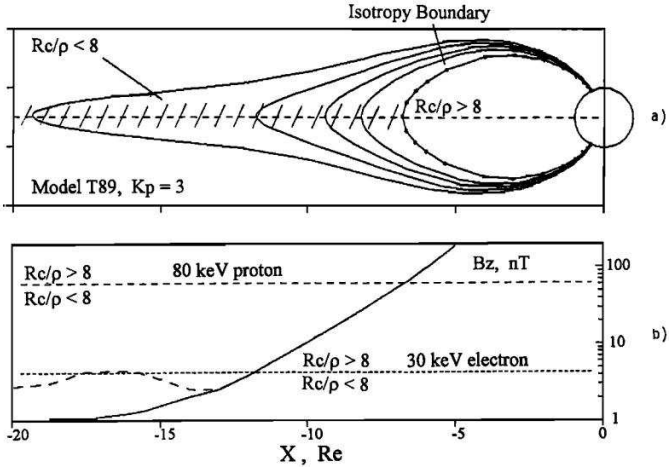

Fig. 1.14: (a) Regions of adiabatic and chaotic particle motion and the isotropic boundary as obtained from eq. (1.15) using T89 model with $K_p = 3$. (b) The radial profile of the B_z component at the equator according to the T89 model (solid line). Threshold values of B_z separating the regions of adiabatic and chaotic motion of 80-keV protons and 30 keV electrons are shown as longer and shorter dashed horizontal lines, respectively. The possible inhomogeneity of B_z in the distant current-dominated plasma sheet is schematically illustrated by the dashed curve.

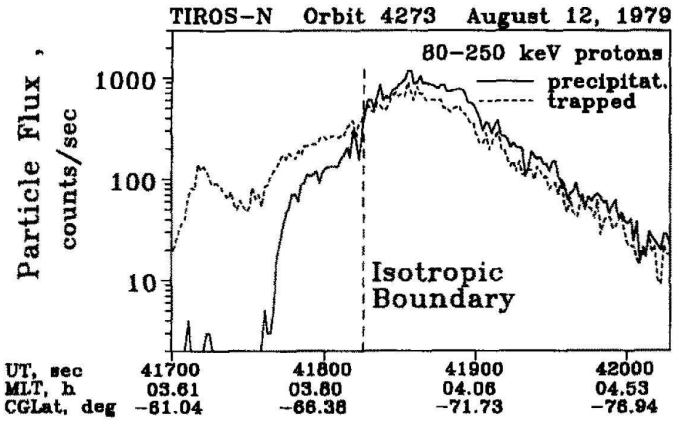

Fig. 1.15: Illustration of the isotropic boundary.

Here R_c and ρ are the curvature radius of the magnetic field line and the particle gyroradius. This simple threshold condition at the tail equator depends only on the equatorial magnetic field and particle rigidity $G = M.V/e$. The equality in expression (1.17) corresponds to the boundary (IB) between regions of empty loss cone and filled loss cone pitch angle distributions observed at low altitudes. Therefore, detecting the IB by low-altitude spacecraft implies that me corresponding relationship between the magnetic field parameters fulfilled in the equatorial section of that magnetic field line. Increasing and/or thinning the tail current moves the equatorial position of that scattering boundary earthward. Also, due to the increased tailward stretching of field lines, the ionospheric projection of any equatorial point moves equatorward. The combined effect of these two mutually related factors leads to the equatorward shift of the IB latitude with increasing tall current. This explains a causal relationship between the IB latitude and the amount of tailward stretching of the magnetotail configuration.

According to the numerical simulations of trajectories of small pitch angle particles done by Sergeev et al. [18, 21], the threshold condition for strong pitch angle scattering in the tail current sheet (scattering to the center of loss cone) is approximately as follows:

$$R_c/\rho = B_z^2(GdB_x/dz)^{-1} \leq 8, \tag{1.18}$$

where the equality sign corresponds to the isotropic boundary. Here R_c and ρ are the radius of curvature of the magnetic field line and the particle gyroradius, respectively, and $G = mv/e$ is the particle rigidity. The boundary between the regions of adiabatic and nonadiabatic particle motion in the equatorial current sheet depends only on the equatorial magnetic field and the particle rigidity. If the ratio R_c/ρ exceeds 8, then the particles are not scattered and remain bounding along the field lines.

Newell et al. defined the location of the B2i as the latitude of the maximum total ion energy flux measured by Defense Meterological Satellite Program (DMSP) spacecraft [22]. This often coincides with a sudden decrease in total flux equatorward of the peak. Although the DMSP spacecraft are currently incapable of pitch-angle resolution, a strong

correlation exists between the B2i and the IB and it is reasonable to infer that they are measures of the same magnetospheric boundary [23]. It is probably the best and most direct proxy for the location of the earthward edge of the current sheet. Consider ions in the energy range from a few keV to tens of keV (30 keV for DMSP). Ions in this energy range increase in temperature and energy flux with declining latitude, apparently as a result of adiabatic acceleration as plasma convects earthward in the magnetotail. This steady temperature increase terminates with a relatively sharp equatorward precipitation cutoff. However, in the high-altitude inner magnetosphere, ions do not disappear at the L-shell value of the high- energy ion precipitation boundary. Instead, the ions become trapped and cease to precipitate in measurable quantities. Poleward of the precipitation boundary at any particular energy, the ions are highly isotropic. It has thus been suggested, and even successfully modeled in some detail, that the ions maintain their isotropy by pitch angle scattering in the tail current sheet. The physical mechanism is quite simple: ions cannot maintain pitch angle while bending around field lines that have a radius of curvature comparable to the ion gyroradii. This explanation also accounts for the dispersion in the high-energy ion cut- offs. The larger gyroradii of higher energy ions means that they scatter off field lines with smaller radii of curvature than do the lower-energy ions; hence the higher-energy ions maintain isotropy farther earthward.

Neither the tail current sheet nor the precipitating high energy ions have a sharply defined boundary. Operationally, Newell et al. proposed to use the ion precipitating energy flux peak (integrated over the range 3-30 keV), which universally occurs near the equatorward boundary of the high energy ion precipitation, as the definition of B2i [22]. The geophysical significance of the boundary is that it represents a good approximation to the earthward edge of the tail current sheet. B. B. Gvozdevsky, and V. A. Sergeev have demonstrated that the latitude of this ion isotropy boundary has a very high correlation, with the magnetic field inclination (degree of stretching) measured simultaneously at the geomagnetic equator [20].

The dependence of IB position of equatorial Bz makes it a potential remote sensing

tool for equatorial magnetic field from low altitudes. In addition, the isotropic boundary analysis can be used to map the auroral oval down to the magnetosphere by comparing the IB positions with lower energy auroral precipitation regions. The IB of > 30 keV protons is found in the diffuse region (equatorward half of the oval) on the nightside, and equatorward of the intense auroral precipitation at dayside and dusk. On the other hand, the IB of > 30 keV electrons on the nightside is often found in the structured precipitation region (poleward half), or just equatorward from it. This implies that the diffuse aurora map to the dipole-like region close to earth, while discrete auroras map to the current sheet region ($Bz < 5$nT). Arcs are often found in wide latitudinal range, most likely covering both near-earth plasma sheet and PSBL. Common feature in all cases is the small Bz value indicating current sheet presence.

1.3 Dissertation Overview

Space weather prediction and intensity of geomagnetic storms are generally measured on the basis of certain geomagnetic indices. But since most of these indices rely on ground measurements and are frequently based on magnetic measurements from magnetometers it is essential to understand the effect of each magnetospheric and ionospheric current on the surface of the earth. But it is difficult to separate the contribution of each current on the basis of single measurements. In this work we have used a multi-model and multiple measurement approach to look at this problem. We extensively use the WINDMI model to model the magnetospheric phenomena and improve the reliability of these results by validating them against multiple data sets.

In the first part of this thesis, a set of geomagnetic storms in the period 2000-2007 will be identified for which the IMF B_z abruptly turns northward during the early recovery phase of the storm. For these events ring current particles are expected to be trapped and the initial fast decay of Dst due to flow out losses should not be dominant. The WINDMI model of the magnetosphere is used to estimate the decay period of Dst and Dst^* indices for different periods of the decay phase.

The WINDMI model assigns a fixed decay rate for the ring current particles. The fixed

decay rate is used initially to compare the decay times obtained by either assuming an early recovery phase or by assuming a decay over the entire duration of the storm for analysis, to infer if different decay rates are observed. A Genetic Algorithm (GA) optimization procedure is used for all the curve fitting done in this work. We assume that the ion outflow during periods of northward magnetic field is not as significant as during southward IMF conditions.

The contribution from other magnetospheric current systems to Dst are investigated in order to estimate their effect on the recovery times of the index. Magnetic perturbations at the surface of the earth due to the cross-tail current can be taken to be proportional to the geotail current value evaluated by the WINDMI model. The contribution of magnetopause currents to the Dst index is assumed to be a function of the solar wind dynamic pressure. A parameterized model for the Dst index is obtained by including contributions from magnetopause currents, ring current, and the tail-current. The modeled magnetic disturbances are optimized for all the storms using a genetic algorithm to obtain solutions that simultaneously have least mean square fit to the AL and Dst indices weighted appropriately.

The solar wind velocity, interplanetary magnetic field and proton density all play a role in transferring energy into the magnetosphere. However, an exact coupling function quantitatively describing the contribution from the solar wind parameters is as yet undecided. The y-directed component of the solar wind rectified electric field E_y as seen in the earth's reference frame given by $\mathbf{v} \times \mathbf{B}$ is commonly used as a coupling function, called the rectified vB_s coupling function, but there are many others. Newell et al. derived a coupling function and compared it's performance against many other functions [24], while Siscoe et al., Borovsky, Lyatsky et al., and Balikhin et al. have produced other coupling functions [25–28].

The performance of these coupling functions have often been compared with regard to their correlation to the Dst index. In Spencer et al., the authors compared the performance of the rectified, Siscoe and Newell coupling functions in re-producing and predicting the westward auroral electrojet AL index, as well as the Dst index [29]. It was found that the

rectified vB_s performed more robustly in prediction compared to the others, but did not perform as well in re-producing the AL indices when doing post-event analysis.

The effects of different coupling functions on the WINDMI model calculation of the tail current's contribution to the Dst index is also a subject of debate. Post-event analysis of a selection of large geomagnetic storms between 2000-2002 is performed to test the capability of different coupling functions in reproducing the Dst index faithfully. The contributions from different current systems as implied by the qualitative differences between the coupling functions will be analyzed. In order to do this the coupling functions were scaled appropriately, and used to drive the WINDMI model. The WINDMI model is generally tuned computationally with a genetic algorithm for the best fit against the measured Dst index. The WINDMI model has been successfully used in the past [30, 31] to analyze substorm dynamics and the AL index signatures associated with solar wind forcing. The AL index will be used as a secondary constraint so that the coupling functions could be differentiated when the Dst indexes are similar for different inputs.

The different coupling functions differ from each other in the solar wind parameters used in their calculation. For the rectified vB_s, only the solar wind parameters v_x and B_z are considered geoeffective. For the coupling functions given by Newell et al. and Siscoe et al., the solar wind dynamic pressure, IMF B_y, IMF B_z, and the solar wind velocity v_x are considered geoeffective [24, 25]. The coupling function due to Borovsky is based on the idea that the solar wind dynamic pressure and Mach number largely controls the rate of reconnection at the nose of the magnetopause, and therefore controls the rate of energy transfer into the magnetosphere.

In this work, the possible contribution of the tail current to the fast initial decay of the Dst index is explored. The WINDMI model is improved and used to understand the relative contribution to the magnetic perturbation on the surface of the earth. This work has led to a series of four papers. Each of the next four chapters are reproductions of the papers. Due to the multipaper format of this thesis, there will be some repetitions of the introduction (Chapter 1) and certain sections of the subsequent chapters.

The first two papers have been published in the Journal of Geophysical Research, Space Physics. The third paper (Chapter 4) has been submitted to the Journal of Atmospheric and Solar-Terrestrial Physics and is under review. The initial results from the fourth paper (Chapter 5) have been presented at the fall meeting of American Geophysical Union in december 2011 and the Committee of Space research 2012 assembly.

The second chapter presents results from the improved WINDMI model. The successful modeling of the two phase decay of the Dst index by the WINDMI model for the chosen set of storms is shown.

Chapter 3 discusses the differences in model results when different coupling functions are used inputs to the WINDMI model. The reliable modeling of the AL index is used as an additional constraint to verify the possible contribution of the tail current.

In Chapter 4, the MT index used as a representative of the strength of the tail current in the magnetosphere. The contributions to the Dst index from both the MT index and the WINDMI model are compared. The effect of substorms on the strength of tail current in investigated.

Ring current simulations and magnetometer data are compared in Chapter 5. Any discrepancy between the model and the magnetometer data are reported and possible causes are suggested. Finally, the work done is summarized and some future work is suggested in Chapter 6.

Chapter 2

Study of Dst/Ring Current Recovery Times Using the WINDMI Model

2.1 Introduction

The disturbance storm time (Dst) index has been widely used as an indicator of geomagnetic activity. Dst^*, which is obtained after removing the contributions from magnetopause currents, induced currents in the conducting earth, and the quiet time ring current, is assumed to represent the ring current (RC) activity during geomagnetic storms. The ring current particles are energized during a geomagnetic storm which corresponds to a decrease in the Dst index. The decay time of the ring current energy is important because the particle injection rate cannot be determined without sufficient knowledge of the decay parameter. It has been observed that the Dst decay following a geomagnetic storm shows a two-phase pattern, a period of fast decay followed by a phase where the Dst returns to its quiet time value gradually [32–34].

There are many theories that have been proposed to explain the observations. It has been proposed that differential decay rates of different ion species may lead to the two-phase decay as explained in the review paper by Daglis et al. [3]. This claim was questioned by Liemohn and Kozyra, whose idealized simulations of ring current decay show that for realistic plasma boundary conditions, a two-phase decay can only be created by the transition from flow-out losses when open drift lines are converted to closed ones in a weakening convection electric field resulting in the charge exchange dominance of ring current loss [35]. In a study by Jordanova et al. it was shown that the fast initial ring current decay is controlled not only by the decreased convection electric field, the dayside

outflow through the magnetopause, and the internal loss processes, but also by the time-varying nightside inflow of plasma from the magnetotail [36].

An alternative explanation is that during the recovery phase of the magnetic storm, the Dst decay is controlled by the decay of two different currents: the ring current and the magnetospheric tail current [33, 37]. Recent work of Kalegaev and Makarenkov indicates that the ring current becomes the dominant Dst source during severe magnetic storms, but during moderate storms its contribution to Dst is comparable with the tail current's contribution [38].

According to certain studies, an abrupt northward turning of the interplanetary magnetic field traps ring current ions on closed trajectories, turning off sources and fast flow-out losses, resulting in charge-exchange losses being the dominant loss process. Under these conditions, it is expected that there is no distinctive two-phase decay but a single phase with a slowly increasing decay time period as species with short charge-exchange collision lifetimes are preferentially removed [14, 32].

Mitchell et al. have used ENA images of the earth's inner magnetosphere to compare the ring current morphology during the Bastille day event and a moderate event on June 10, 2000 for which the IMF B_z gradually turned northward [39]. They confirmed that the contribution to the ring current in the small, June 10 storm and associated substorms was much further away from earth, and much more dependent on open drift path dynamics, than in the larger Bastille storm where the ions contributing to Dst drifted primarily on closed paths.

Based on ion flux measurements by the Geotail satellite, Kieka et al. have suggested, that near the earthward side of the low latitude boundary layer, the drift governing the ion outflow is mainly the ∇B drift [40]. They concluded that the ion outflow contributes significantly to the rapid decay of the ring current, even in the case of a sudden northward turning of the interplanetary magnetic field. However, Lee et al. have reported that the magnetospheric compression by a dynamic pressure (P_{dyn}) enhancement usually causes particle fluxes to increase globally around the earth [41]. They argued that changes in the

particle flux at a given energy channel due to the compressional effect of a P_{dyn} enhancement must, in general, be determined by a combination of adiabatic acceleration and the spatial (radial) profile of the source particle distribution at constant first and second adiabatic invariants.

In this work, we identify geomagnetic storms in the period 2000-2007 where the IMF B_z abruptly turns northward during the early recovery phase of the storm. For these events ring current particles should be trapped and the initial fast decay of Dst due to flow out losses should not be dominant. We use the WINDMI model to estimate the decay period of Dst and Dst^* indices for different periods of the decay phase.

The WINDMI model, which is described in the next section, assigns a fixed decay rate for the ring current particles. We use the fixed decay rate to compare the decay times obtained by either assuming an early recovery phase or by assuming a decay over the entire duration of the storm for analysis, to infer if different decay rates are observed.

A Genetic Algorithm (GA) optimization procedure is used for all the curve fitting done in this work. The algorithm is explained in section 2.3. The test for differential decay rates of the Dst and the events used in this study are explained in section 2.4.1. We assume that the ion outflow during periods of northward magnetic field is not as significant as during southward IMF conditions.

The contribution from other magnetospheric current systems to Dst is investigated in section 2.5 to estimate their effect on the recovery times of the index. Magnetic perturbations at the surface of the earth due to the cross-tail current is taken to be proportional to the geotail current value evaluated by the WINDMI model. The contribution of magnetopause currents to the Dst index is assumed to be a function of the solar wind dynamic pressure. The expressions used for the magnetopause contributions are explained in section 2.5. A parameterized model for the Dst index is obtained by including contributions from magnetopause currents, ring current, and the tail-current. The modeled magnetic disturbances are optimized for all the storms using a genetic algorithm to obtain solutions that simultaneously have least mean square fit to the AL and Dst indices weighted appropriately.

2.2 The WINDMI Model

The plasma physics-based WINDMI model uses the solar wind dynamo voltage, V_{sw}, generated by a particular solar wind-magnetosphere coupling function to drive eight ordinary differential equations describing the transfer of power through the geomagnetic tail, the ionosphere, and the ring current. The WINDMI model has been described in some detail in past works [30, 42, 43]. The equations of the model are given by:

$$
\begin{aligned}
L\frac{dI}{dt} &= V_{\rm sw}(t) - V + M\frac{dI_1}{dt}, && (2.1)\\
C\frac{dV}{dt} &= I - I_1 - I_{\rm ps} - \Sigma V, && (2.2)\\
\frac{3}{2}\frac{dp}{dt} &= \frac{\Sigma V^2}{\Omega_{\rm cps}} - u_0 p K_{\parallel}^{1/2}\Theta(u) - \frac{pVA_{\rm eff}}{\Omega_{\rm cps}B_{\rm tr}L_y} - \frac{3p}{2\tau_E}, && (2.3)\\
\frac{dK_{\parallel}}{dt} &= I_{ps}V - \frac{K_{\parallel}}{\tau_{\parallel}}, && (2.4)\\
L_I\frac{dI_1}{dt} &= V - V_I + M\frac{dI}{dt}, && (2.5)\\
C_I\frac{dV_I}{dt} &= I_1 - I_2 - \Sigma_I V_I, && (2.6)\\
L_2\frac{dI_2}{dt} &= V_I - (R_{\rm prc} + R_{A2})I_2, && (2.7)\\
\frac{dW_{\rm rc}}{dt} &= R_{\rm prc}I_2^2 + \frac{pVA_{\rm eff}}{B_{\rm tr}L_y} - \frac{W_{\rm rc}}{\tau_{\rm rc}}. && (2.8)
\end{aligned}
$$

The nonlinear equations of the model trace the flow of electromagnetic and mechanical energy through eight pairs of transfer terms. The remaining terms describe the loss of energy from the magnetosphere-ionosphere system through plasma injection, ionospheric losses, and ring current energy losses.

In the differential equations the coefficients are physical parameters of the magnetosphere-ionosphere system. The quantities L, C, Σ, L_1, C_I, and Σ_I are the magnetospheric and ionospheric inductances, capacitances, and conductances, respectively. A_{eff} is an effective aperture for particle injection into the ring current, that on the dusk side merges with what is known as the Alfven layer [42]. The Alfven layer is defined to be the separatrix between two sets of drift trajectories, one comprising open drift paths extending from the magneto-

spheric tail to the dayside magnetopause and another, nearer set consisting of closed drift paths, encircling the earth [44]. The resistances in the partial ring current and region-2 current, I_2 are R_{prc} and R_{A2}, respectively, and L_2 is the inductance of the region-2 current. The coefficient u_0 in eq. (2.3) is a heat flux limiting parameter. The energy confinement times for the central plasma sheet, parallel kinetic energy and ring current energy are τ_E, τ_k, and τ_{rc}, respectively. The effective width of the magnetosphere is L_y and the transition region magnetic field is given by B_{tr}. The pressure gradient driven current is given by $I_{ps} = L_x(p/\mu_0)^{1/2}$, where L_x is the effective length of the magnetotail. The output of the model are the AL and Dst indices, in addition to the magnetospheric field aligned currents.

The parameters are combined appropriately into a vector P_d where $d = 18$. They can be estimated using semi analytical techniques or they can be considered as variables that need to be optimized within physically allowable ranges to fit the data for a given storm. The parameters have been approximated analytically using the Tsyganenko magnetic field model and then allowed to vary over a physically reasonable range of values as explained in Spencer et al. [30].

The solar wind dynamo voltage used to drive the model is generated using the Rectified IMF Driver [45] coupling function ($v_{sw}B_s$) which is given by:

$$VB_s = 40(kV) + v_{sw}B_s L_y^{eff}(kV), \tag{2.9}$$

where v_{sw} is the x-directed component of the solar wind velocity in GSM coordinates, B_s is the southward IMF component and L_y^{eff} is the effective cross-tail width over which the dynamo voltage is produced. For northward or zero IMF B_z, a base viscous voltage of 40 kV is used to drive the system. The rectified $v_{sw}B_s$ was preferred over other coupling functions as it has been shown to be a more robust driver compared to other coupling functions, while maintaining reasonably good feature reproduction capability [29].

The current I_1 used in the model is that portion of the field aligned region 1 current that maps to the nightside central plasma sheet and is considered to be part of the substorm current wedge that produces the westward auroral electrojet. The Auroral AL index now

follows as a magnetic field perturbation ΔB_{AL} from the ambient terrestrial field due to the westward electrojet current that flows in the E-layer ($\sim 90 - 120km$) in the nightside ionosphere. We estimate the relation between I_1 and the AL index by assuming that the current I_1 is related linearly to the AL index by a constant of proportionality [30].

The Dst signal is obtained from the plasma energy stored in the ring current W_{rc} calculated by the WINDMI model. It is given by the Dessler-Parker-Sckopke (DPS) [46,47] relation:

$$Dst = \frac{\mu_0 W_{rc}(t)}{2\pi B_E R_E^3}, \tag{2.10}$$

where B_E is the earth's surface magnetic field along the equator.

The ring current energy (W_{rc}) injection terms in the WINDMI model are the first and second terms on the right hand side of eq. (2.8). The current I_2 is a region 2 current that leaves the ionosphere on the dawn side, closes in the ring current and returns to the ionosphere on the dusk side. This secondary loop of current has a self inductance L_2 and drives a current through the partial ring current resistance R_{prc} as well as the resistance of the region 2 current loop footprint R_{A2}. The Joule heating through the resistance R_{prc} energizes the ring current particles. The particles injected across the effective aperture A_{eff} is another source of ring current energy. Equation (2.8) of the WINDMI model is similar to the Dst^* decay equations of Burton et al., and O'Brien and MCPherron [13,15]:

$$\frac{dDst^*}{dt} = Q(t) + \frac{Dst^*(t)}{\tau_{rc}}, \tag{2.11}$$

where $Q(t)$ is an injection term and τ_{rc} is the ring current decay rate.

The ring current energy in the model is assumed to be lost by particles drifting out of orbit or by charge exchange processes at a rate proportional to τ_{rc}. It is unclear which of these processes are at work during a particular event. In the model, decay times of around 12 hours indicate that flow out losses dominate, while longer decay times of 18-30 hours indicate that charge exchange processes dominate.

2.3 Optimization with a Genetic Algorithm

The variable coefficients in the WINDMI model are L, M, C, Σ, Ω_{cps}, u_0, I_c, A_{eff}, B_{tr}, L_y, τ_E, $\tau_{||}$, L_I, C_I, Σ_I, L_2, R_{prc}, R_{A2}, τ_{rc}, and α. These parameters are constrained to a maximum and a minimum physically realizable and allowable values and combined to form a 18-dimensional search space $S \subset \mathbb{R}^{18}$ over which an optimization is performed.

Genetic Algorithms are general search and optimization methods that are inspired by the concepts of crossover, random mutation, and natural selection from evolutionary biology. In the current context, one form of the genetic algorithm [48] is applied to search the physical parameter space in order to minimize the error between the model output and the measured geomagnetic indices. In earlier works with simpler models, the alternate-gradient, steepest-descent, and simulated annealing methods were used to find optimal parameters. These methods were found to have problems getting stuck in local minima. Stochastic search methods such as genetic algorithms perform better in search spaces where objective functions have multiple local minima and are consequently suitable for nonlinear state-space systems such as the WINDMI model.

The optimization scheme was used to select a parameter set for which the outputs from the WINDMI model most closely matches the AL index and the Dst index simultaneously. In an earlier work we discussed the results of optimizing against Dst only or AL only, or an equal combination of both [29]. For this work we were more interested in the features of the Dst index, so we have chosen a higher bias of 0.8 for Dst while the AL index was given a weighting of 0.2 in order to maintain a reasonably good fit.

The performance of the algorithm is evaluated by how well the average relative variance (ARV) and correlation coefficient (COR) compare with the measured indices. The average relative variance gives a good measure of how well the optimized model tracks the geomagnetic activity in a normalized mean square sense, while the correlation coefficient shows how well the model tracks the geomagnetic variations above and below its mean value.

The ARV is given by:

$$ARV = \frac{\Sigma_i (x_i - y_i)^2}{\Sigma_i (\bar{y} - y_i)^2}, \tag{2.12}$$

where x_i are model values, y_i are the data values, and $\bar{y}$ is the mean of the data values. In order that the model output and the measured data are closely matched, ARV should be closer to zero. A model giving $ARV = 1$ is equivalent to using the average of the data for the prediction. If $ARV = 0$ then every $x_i = y_i$. ARV values above 0.8 are considered poor for our purposes. ARV below 0.5 is considered very good, and between 0.5 to 0.7 it is evaluated based upon feature recovery.

The correlation coefficient COR is calculated against the AL index only as a measure of performance but not used as a cost function in the optimization process. COR is given by:

$$COR = \frac{\Sigma_i (x_i - \bar{x})(y_i - \bar{y})}{\sigma_x \sigma_y}. \tag{2.13}$$

COR is better when closer to 1. It indicates anti-correlation if the value is close to -1. σ_x and σ_y are the model and data variances, respectively. Typically, if the correlation coefficient is above 0.7, the performance is considered satisfactory for the physics-based WINDMI model. Both the ARV and COR values are calculated over the period when the most geomagnetic activity occurs.

When these criteria are observed to be acceptable, the optimization process is assumed to have reached convergence. Here we do not explicitly report the ARV or COR values, since we are more interested in the qualitative fit, and the relative contributions from the various current systems.

2.4 Events and Data

We selected geomagnetic disturbance events in the recent solar cycle that resulted in the Dst index dropping off by at least -60 nT (i.e., $Dst < -60$ nT), and for which the IMF B_z was positive (i.e, $v_{sw}B_s = 0$) during the early recovery phase of the storm for relatively long periods of time (at least 12 hours). This will turn off the input, $v_{sw}B_s$ into the WINDMI model for some time during the recovery phase so that the initial decay phase is exponential and can be easily analyzed. We note that when there is no energy input, as may occur during an ideal recovery phase of geomagnetic storm, eq. (2.8) has the following

simple exponential solution:

$$W_{rc}(t) = W_{rc0}e^{-(t-t_0)/\tau_{rc}}, \tag{2.14}$$

from which one can obtain reasonably accurate values for the decay time τ_{rc}. Storms with relatively long positive IMF B_z conditions during the recovery phase will be termed as having a clean recovery phase.

A total of thirteen events have been identified in the period between the years 2000-2007, for which the IMF B_z turned northward abruptly after the peak in Dst index was observed. Here we use the term "peak in Dst" to represent the minimum Dst value reached during a storm period since this corresponds to the peak energization level of the ring current particles.

Under the northward IMF turning conditions for the chosen events, the ring current particles are most likely to be trapped and the suggested fast "flow-out" losses on the dayside are probably not significant during the early recovery phase of a storm. Charge exchange losses is then expected to be the dominant mechanism for ring current decay under these conditions. The observed Dst decay should then be due to the different charge exchange lifetimes of ions in the ring current and possibly the contributions from other currents in the magnetosphere.

The solar wind parameters in GSM coordinates required as input to the WINDMI model are obtained from the ACE satellite orbiting at the L1 point between the sun and the earth. Missing or unusable data from the satellite measurements was dealt with by retaining the previous data value whenever the data was unusable. We discuss this again in section 2.5. Hourly AL and Dst index values were obtained from the World Data Center for Geomagnetism, Kyoto website.

Most of the events were found during the solar maximum and were caused by coronal mass ejections (CMEs) and flares. Only the event in 2007 (days 81-88) was caused by the passage of a corotating interaction region (CIR) across earth. The largest storm matching our criteria had a maximum peak in Dst of -300 nT, while the smallest storm had an

associated Dst peak of just -70 nT.

During three of the thirteen events the IMF B_z turned northward gradually some time after the peak in Dst was observed, but did not change its polarity during the next 12 hours. These events were on days 100-104 (2001), 265-268(2001) and 142-146 (2002). The initial recovery of these three storms could have a more significant contribution from fast flow out losses before charge exchange losses dominate as the IMF B_z turns northward. All thirteen events had an associated increase in solar dynamic pressure during the storm main phase. Of the thirteen events, six showed an increase in solar wind forcing before complete recovery of Dst ($Dst > -20$ nT), as indicated by corresponding increase in VB_s values. These events were on days 158-166 (2000), 260-265 (2000), 100-104 (2001), 80-88 (2002), 245-260 (2002), and 81-88 (2007).

2.4.1 Decay Times of Dst and Dst^* Using WINDMI

One of the outputs of the WINDMI model is the ring current energy which is related to the Dst index by the Dessler Parker-Sckopke relation through eq. (2.10). The contribution to the Dst index due to the magnetopause currents and other induced currents is not calculated by the model. For this reason it is more appropriate to match the WINDMI Dst output against Dst^* which is calculated using the following expression [10]:

$$Dst* = \frac{Dst - Dst_{mp} + D_{qrc}}{C_{IC}}, \tag{2.15}$$

where C_{IC} is a correction factor due to induced currents in the earth, which is taken to be 1.3. Dst_{mp} is the perturbation from the Chapman-Ferraro currents on the magnetopause, taken to be $a * \sqrt{P_{dyn}}$ (solar wind dynamic pressure in nPa), and D_{qrc} is the contribution from the quiet time ring current (subtracted out as a baseline offset of the Dst). The factor a is a scaling factor to be explained below.

The WINDMI model does not account for the currents induced on the surface of the conducting earth due to currents in the magnetosphere. The traditional definition of Dst^* as mentioned by Burton et al. [13], subtracts the contributions from magnetopause currents

and the quiet time Dst values. This definition of Dst^* is the same as the numerator of eq. (2.15). Induced currents flowing inside the earth's core enhance the measured magnetic field of each external current approximately by C_{IC}. Since the WINDMI model does not model these induced currents, it is more appropriate to divide out this enhancement due to induced currents from the Dst, following eq. (2.15) [14]. For this work we have assumed Dst^* to represent the contribution mainly from the ring current and possibly from other magnetospheric currents (other than magnetopause and induced currents).

We used two combination of values for a and D_{qrc}. The first one was obtained by Burton et al., and corresponds to values of 15.5 and -20 nT for a, and D_{qrc}, respectively [10, 13]. The Dst^* obtained using this formula will be henceforth referred to as Dst^*_B in this work. O'Brien and McPherron estimated values of 7.26 for a and 11 nT for D_{qrc}, which was the second combination used and the Dst^* calculated with these values will be referred to as Dst^*_O [15]. We therefore obtain two sets of Dst^* values for the 13 selected events.

We optimized the WINDMI model against the AL and Dst indices giving an 0.8:0.2 preference to Dst importance over AL. We mention that it is important to optimize against the AL index with some minimal weighting for all cases because the state variables p, V, and I_2 in eq. (2.8) depend on the first seven equations but not vice versa. By including some bias towards AL optimization, the parameters in the first seven equations are constrained consistently.

On the other hand, we want especially to capture the features in the Dst index, so we set a higher bias towards Dst. The higher bias given towards Dst for all our cases makes the parameters in the last two WINDMI eqs. (2.7) - (2.8) have a stronger influence on the results.

Each of the 13 events was optimized twice, once for a period encompassing only the main phase and the initial Dst recovery phase (period 1), and once for the entire duration of the storm (period 2). Recovery of a storm was assumed to be complete after Dst reached values greater than -20 nT. The period selection scheme is illustrated in fig. 2.1. The scheme was chosen to distinguish between different decay phases of the Dst index during

the course of a geomagnetic storm.

This optimization process was repeated for Dst^*_B and Dst^*_O under the same set of criteria as was done for just Dst. Period 1 and period 2 were the same for each event as was estimated for Dst optimization. The optimization results are summarized in Table 2.1. We make some observations about the selected events and discuss the results of the optimizations in the next section.

2.4.2 Events and Optimization Results

The selected geomagnetic events are discussed in chronological order below. The optimized plots for all the events can be found in the auxiliary file published with this paper. The reason why we discuss the details of each storm event is because we wish to draw attention to similarities and differences between events that might influence the interpretation of the results. Note that Dst recovery periods after northward turning of the IMF tend to give more direct and simpler interpretations, based on the discussion earlier.

Days 158-166, 2000. For this event a sudden jump in ACE solar wind velocity and proton density data was observed at 0936 UT on day 159. An associated sudden storm commencement (SSC) was observed in the Dst data. The IMF B_z turns northward at 2200 UT on day 160 and stays mostly northward for almost 24 hours (up to day 161), following which it turns southward again. Period 1 for this event was from days 158-160.5 in the year 2000. The best WINDMI Dst fit to Dst data during period 1 yielded a decay time of $\tau_{rc} = 11.1$ hours. The entire storm duration which was the same as period 2 for this event was from days 158-164 and the corresponding decay time was $\tau_{rc} = 18.5$ hours.

Days 195-202, 2000. This is the extensively studied Bastille day storm that was caused by a solar flare on July 14, 2000. Velocity and proton density data from the ACE satellite were corrupted during the main phase of this event. Around 2000 UT, the IMF B_z at earth became less negative (increasing to about - 10 nT), before turning northward about an hour into 16 July. This effectively ended the convective phase of the storm, and the ring current (as monitored by Dst index) began a steady decay during the third hour of the day. The IMF B_z remains mostly northward for a significant duration in the recovery

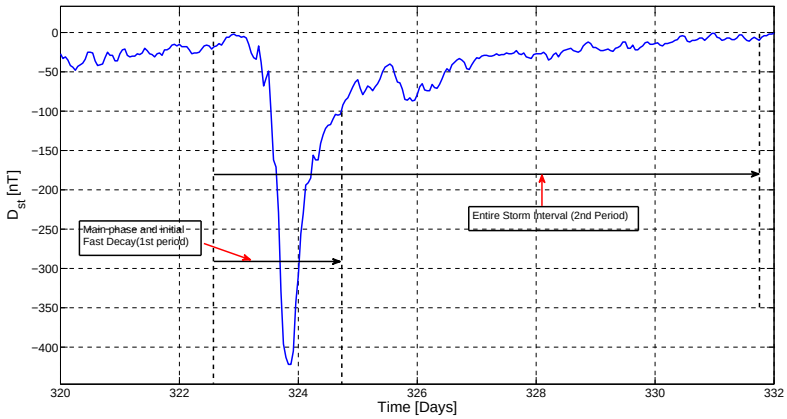

Fig. 2.1: A typical storm time Dst measurement showing the two matching periods used in this work. Period 1 includes the main and the initial fast decay phase and Period 2 is the entire duration of the storm which relates to the overall ring current decay rate.

Table 2.1: Ring current decay rates estimated over period 1 and 2 for the thirteen events by optimizing against Dst, Dst^*_O, and Dst^*_B using the WINDMI model. Dst -In, $Dst^*_{O/B}$ -In lists the values for period 1 (initial phase) and Dst -En, $Dst^*_{O/B}$ -En lists the values for period 2 (entire storm).

Event day	Dst-In	Dst-En	Dst^*_O-In	Dst^*_O-En	Dst^*_B-In	Dst^*_B-En
$2000-158$	11.1	18.5	10.27	13.57	14.4	24.3
$2000-195$	16	22.7	15.65	19.35	14.4	26.77
$2000-260$	16	25.1	11.1	25.9	17.7	42.45
$2001-100$	5.3	17.7	4.5	14.4	4.5	21
$2001-225$	16.8	27.6	13.75	16	16.87	42.45
$2001-264$	15.2	21	14.4	16	21.8	32.55
$2001-325$	20.1	28.4	20.17	25.95	24.3	48.22
$2002-80$	14.4	16.1	12.75	13.57	20.1	38.32
$2002-142$	19.3	33.4	14.4	26.77	15.2	53.17
$2002-245$	11.9	21.8	11.1	21	13.57	26.77
$2004-93$	8.6	7.8	7.8	8.62	14.4	16.87
$2005-6$	16	32.5	16	25.1	12.75	46.57
$2007-81$	4.5	7.8	5.3	6.97	15.2	38.3

phase (about 48 hours).

Due to the prolonged northward IMF period this event shows what we consider as an ideal recovery of Dst. The best fits against Dst data, for the Bastille day event are shown in fig. 2.2 corresponding to period 1 of days 195-197.8, and fig. 2.3 for period 2 comprising the days 195-200. These figures illustrate the matching technique employed and typical results. From Table 2.1 it is evident that an increase in decay under all three matching conditions is observed.

Days 260-265, 2000. Period 1 for this event was from days 260-261.8. Period 2 for this event was from days 260-265. At about 1600 UT on day 260, the Dst index showed a positive excursion in value, which corresponds to an associated increase in proton density. The IMF B_z turned southward at 2024 UT on day 260 which triggered the main phase of the storm. The IMF B_z turned northward shortly after the start of day 261 leading to the recovery phase of the event. The best fit values for Dst as well as Dst^* show that the WINDMI model ring current estimates a delayed Dst minimum as compared to the Dst data.

Days 100-105, 2001. This is one of the three events for which the IMF B_z did not turn northward, right after the peak in Dst was observed. A 3-5 hour delay in attaining the Dst minimum was observed in the best fits for all the three indices (Dst, Dst^*_B, and Dst^*_O). Period 1 for this event was from 100-101.5 days, while period 2 was from 100-104 days.

Days 225-235, 2001. An SSC event was observed at 1200 UT on day 228, the Dst value rose up to almost 50 nT due to this. The IMF B_z turned southward almost immediately signaling the start of the storm. This is another example of a clean event as the IMF B_z turned northward after the peak in the Dst index was observed and stayed northward. The recovery was clean as there is no energy input from VB_s, the fluctuation observed in the recovery of the Dst index correlate highly with changes in P_{dyn} and is probably due to changing currents in magnetopause.

Days 265-268, 2001. This is the second event for which the IMF B_z turned northward

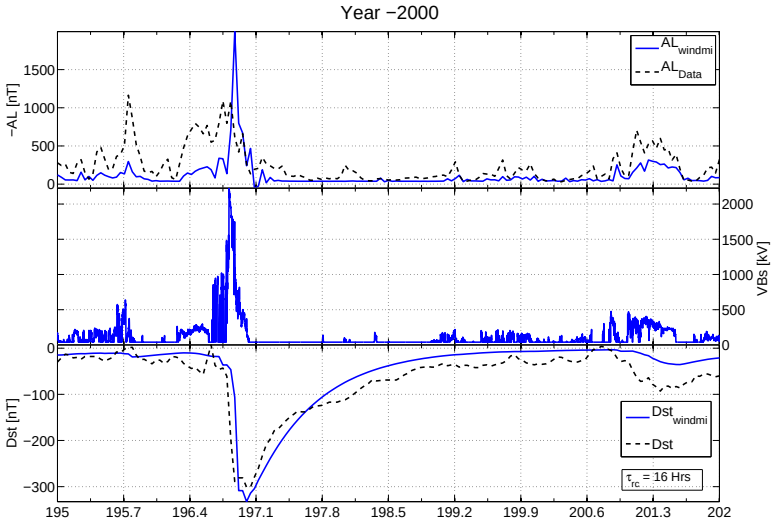

Fig. 2.2: The best fit for days 195-197.8 (main and early recovery phase, period 1) of the event (195-200 days) in the year 2000, obtained by optimizing with a 0.8*Dst:0.2*AL preference to measured data.

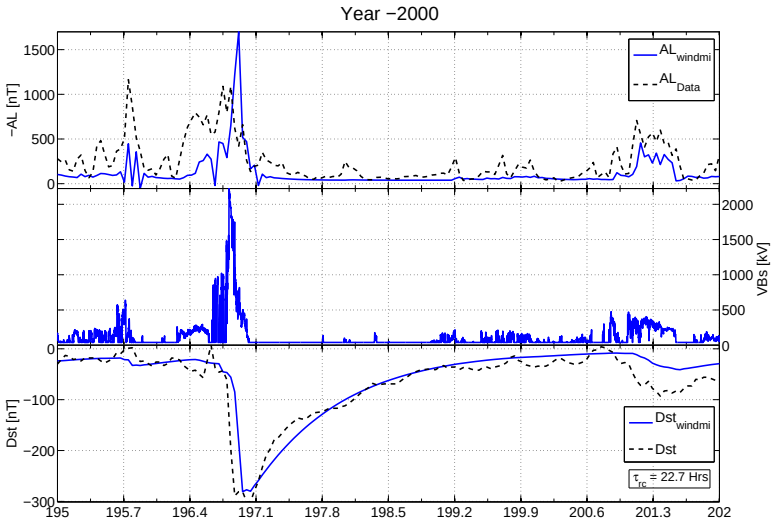

Fig. 2.3: The best fit for the event on days 195-200 (entire storm, period 2) in the year 2000, obtained by optimizing with a 0.8*Dst:2*AL preference to measured data.

some time after the peak in Dst was observed. A significant delay in attaining the Dst minimum was observed after finding the best fits for all the three Dst indices (Dst, Dst^*_O and Dst^*_B). This is one of the smaller storms investigated as indicated by a Dst minimum of -70 nT.

Days 325-335, 2001. This event is similar to the Bastille day storm with respect to its recovery phase although it is of lesser intensity. The recovery phase during the long period of northward IMF was clean. ACE solar wind proton and velocity data were corrupted during the storm main phase. Period 1 extends from 327-328.5 and period 2 was taken to be from 327-333 days. A clear increase in decay times was observed for the results of best fits for period 1 to period 2 for all three Dst indices.

Days 80-88, 2002. The main phase of this twin peaked Dst event started at 1424 UT on day 81 when the IMF B_z turned southward. Days 81-84 was assumed to be period 1 and the days from 81-88 was taken to be period 2. On days 84-85 during the recovery phase of this event, the IMF B_z turned southward and the solar wind forcing was large enough to affect the recovery. This activity in the Dst index is not predicted by WINDMI, when contributions only from ring current energy is used for matching against Dst. Increase in decay from period 1 to period 2 is not evident for Dst or Dst^*_O but for Dst^*_B a clear increase in decay time is observed. The optimized results for this event are shown in figs. 2.4 - 2.9.

Pressure enhancements during the recovery phase of the Dst index probably had a role to play in the faster recovery of the measured Dst. The contributions of magnetopause currents to the measured Dst are higher according to the values of Burton et al. [13] compared to the numbers suggested by O'Brien and McPherron [15]. This difference can be seen in the Dst^*_B and Dst^*_O plots shown in figs. 2.6, 2.7, 2.8, 2.9.

Days 142-146, 2002. This is the third event of the thirteen events for which the IMF B_z turned northward 9.6 hours after the peak in Dst was observed. The storm duration was relatively short compared to the other events. The SSC at the start of the main phase of this event resulted in Dst reaching values higher than +50 nT. The plots for Dst^*_O and Dst^*_B which are included in the auxiliary file, show significant differences in accounting for

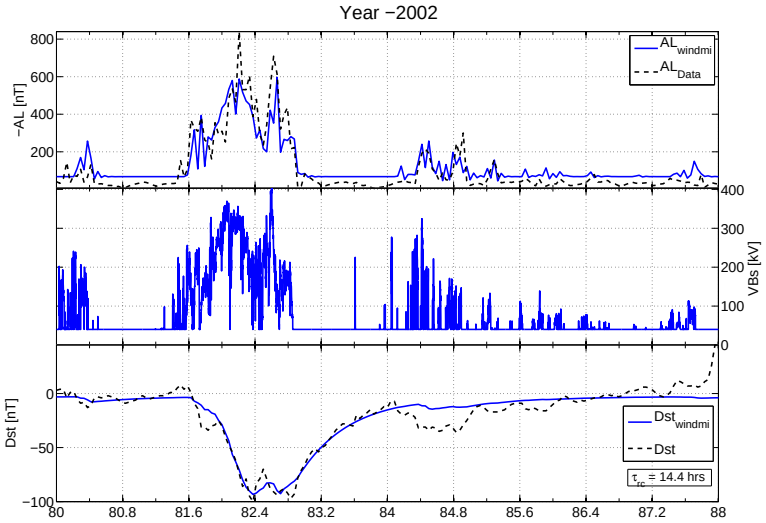

Fig. 2.4: The best fit for days 81-84 (main and early recovery phase) of the event on (81-87 days) in the year 2002, obtained by optimizing with a 0.8*Dst:2*AL preference to measured Dst data.

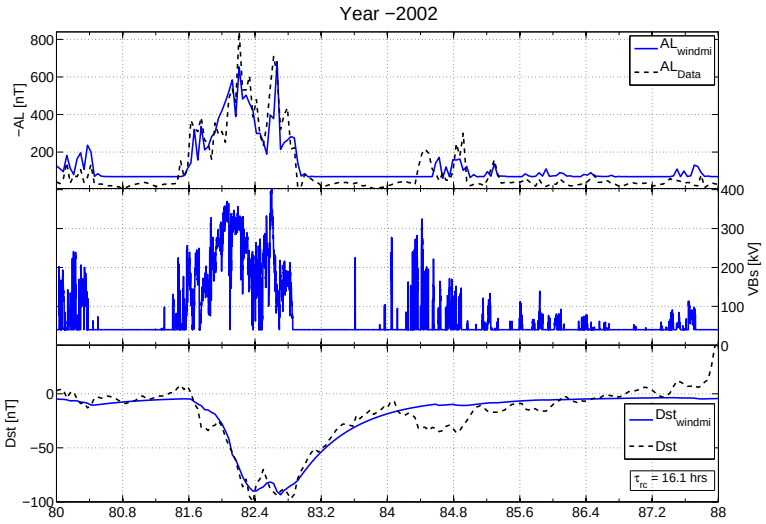

Fig. 2.5: The best fit for the event of days 81-87 (entire storm) in the year 2002, obtained by optimizing with a 0.8*Dst:0.2*AL preference to measured Dst data.

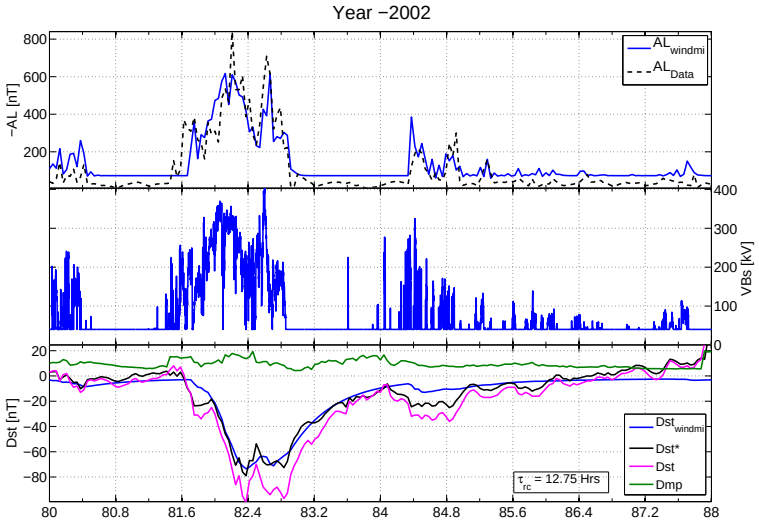

Fig. 2.6: The best fit for days 81-84 (main and early recovery phase) of the event on (81-87 days) in the year 2002, obtained by optimizing with a 0.8**Dst*:2*AL preference to *Dst**O data.

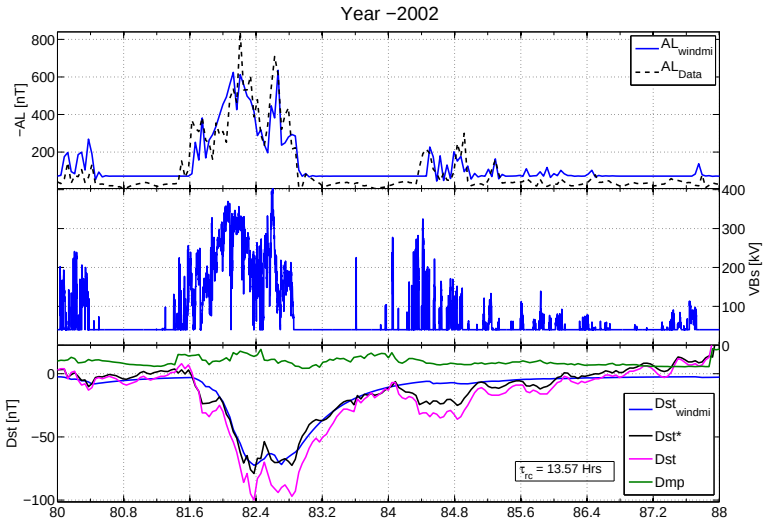

Fig. 2.7: The best fit for the event of days 81-87 (entire storm) in the year 2002, obtained by optimizing with a 0.8**Dst*:0.2*AL preference to measured *Dst**O data.

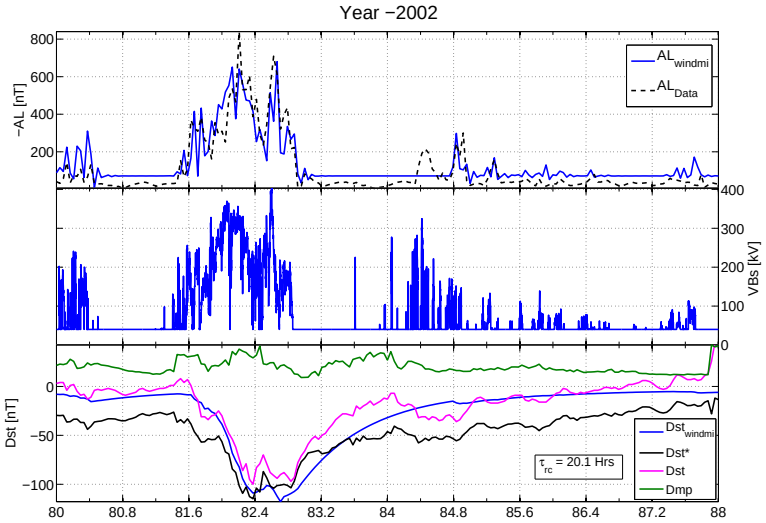

Fig. 2.8: The best fit for days 81-84 (main and early recovery phase) of the event on (81-87 days) in the year 2002, obtained by optimizing with a 0.8**Dst*:2*AL preference to *Dst**B data.

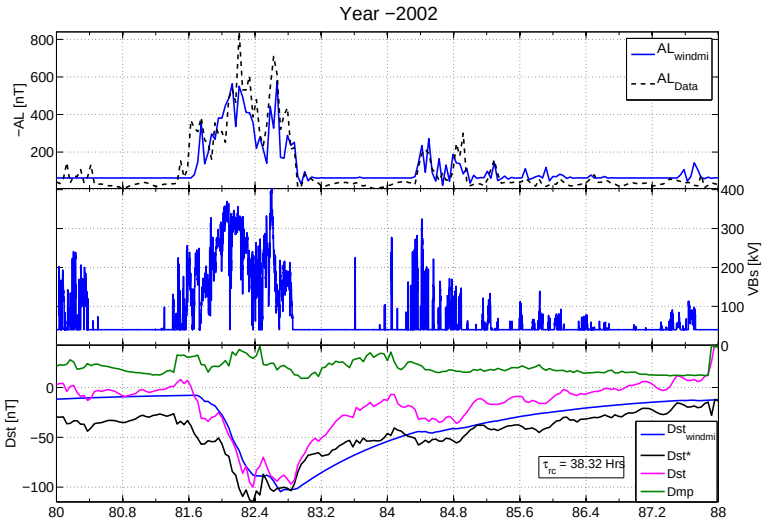

Fig. 2.9: The best fit for the event of days 81-87 (entire storm) in the year 2002, obtained by optimizing with a 0.8**Dst*:0.2*AL preference to measured *Dst**B data.

the SSC effects. Dst^*_O estimates the contribution of pressure enhancements to be lower and hence still shows large positive excursion in its values. The larger contribution of P_{dyn} to Dst^*_B ensures that the resulting values remain negative.

Days 245-260, 2002. This was a multistage event. The first stage had an SSC associated with it. The IMF B_z turned northward for a short while after the peak in Dst for the second and the largest event. The IMF B_z was again southward during the recovery phase while the Dst recovered to its quiet time values. The optimization ranges are short compared to the total event duration. Period 1 is from 249-251 while period 2 is from 249-252. The increase in decay time observed is obtained during the period of northward IMF B_z in the recovery phase.

Days 93-95.5, 2004. This is one of the shortest duration events that we analyzed, lasting only 3 days. The Dst recovered from its peak value to a value of -20 nT within just one and a half days. The event on days 93-95.5 (2004) was followed by increased solar wind forcing as the IMF B_z again changed direction to become southward on day 95.5, thus complete de-energization of ring current particles may not have occurred. Increase in P_{dyn} during the recovery phase also affected the recovery rates.

Days 6-10, 2005. During the storm main phase, ACE proton density values were missing. The IMF B_z was mostly northward for almost the complete duration of the storm recovery. Again an increase in decay times from period 1 to 2 is observed for all the three indices.

Days 81-88, 2007. On days 81-88 (2007), the IMF B_z turned northward for a short duration during a CIR event while the rest of the time the IMF B_z fluctuated between two polarities. P_{dyn} enhancement during the period of northward B_z is the dominant contributor to Dst recovery in this case. The increase in τ_{rc} observed by optimizing against both Dst and Dst^* for this case is because of continuous injection of energy from the solar wind as B_z fluctuates, resulting in an increased effective decay time. Noticeable differences can be found in the Dst^*_O and Dst^*_B plots, which we discuss below.

2.4.3 Two-Phase Decay Observations

From Table 2.1, we observe that for most of the cases an increase in the decay period of Dst indices are obtained, from optimizing the model during period 1 compared to period 2. However, for the events on days 80-88 (2002), 93-95.5 (2004), and days 81-88 (2007), an almost insignificant difference was obtained.

Matching results using Dst^*_B for the event on days 80-88 (2002) show an increase in decay time from period 1 to period 2, which was not evident for Dst and Dst^*_O. The decay times optimized for period 2 of Dst^*_B is consistently higher compared to Dst and Dst^*_O values.

From Table 2.1 we notice that the event in 2004 is the only event for which a clear increase in decay time for the entire storm duration is not observed. All three best fits against Dst, Dst^*_O, and Dst^*_B data for this event show only a marginal increase in decay times.

Using Dst^*_B for the event on days 81-88 (2007) shows that the increase in decay times is because of CIR induced IMF B_z fluctuations. The higher contribution of pressure enhancements effects in Dst^*_B almost completely removes the fast decay during the period of northward IMF for this event. This is in contrast to the results obtained using Dst and Dst^*_O, which are significantly affected by the sharp recovery due to P_{dyn}.

It should be noted that the τ_{rc} numbers estimated by the WINDMI model by optimizing against Dst are not true representations of the recovery of ring current particles. Contributions from magnetopause currents due to pressure enhancements and other magnetospheric currents affect the decay rates. Using pressure corrected Dst^* does not completely resolve this issue, as the relative contribution of Dst_{mp} is not accurately known yet. However these values are a more accurate representation of the contribution of the near earth current systems.

The increase in decay times observed agree with the findings of O'Brien et al. [49], who show that storms with abrupt northward turning of IMF B_z, show the same amount of recovery in the first 6 hours or slightly faster recovery than do the storms with gradual

northward turnings. This could be attributed to a gradual increase in decay times of ring current particles or a manifestation of the recovery times of the other magnetospheric current systems. The tail current in particular, is known to decay on a much smaller time scale compared to the ring current.

In the next section, we describe how the inclusion of the tail current and magnetopause currents influences the observed decay rates.

2.5 Contribution of Magnetospheric Currents

The major current systems in the magnetosphere are: (1) the magnetopause currents shielding earth's dipolar magnetic field; (2) the symmetric ring current; (3) the partial ring current; and (4) the cross-tail current along with the closure currents on the magnetopause. All these currents cause magnetic perturbations on the earth's surface. The results in the last section indicate that there is an increase in decay times as the Dst recovers during a magnetic storm even under abrupt northward turning of IMF B_z. To contrast the contribution of other currents to this observation we add the magnetopause current and cross tail current contributions in addition to the WINDMI ring current in order to calculate the simulated Dst index. The quiet time values for each current system is included in the WINDMI model calculations.

Liemohn et al. obtained the contribution of the partial ring current (PRC) to Dst during the storm main phase to be as large as 80% [50]. Y. Maltsev estimates the contribution of the PRC with the induction currents inside the earth to be 15% [2]. They argue that neglecting the polarization electric field originating from charge separation in the course of particle sunward convection led to the substantially higher values obtained by Liemohn et al. [50]. According to Tsyganenko and Sitnov the westward near-equatorial part of the PRC is largely offset in the dawn sector by the opposite effect of the field-aligned closure currents, hence their contribution to the Dst is very small compared to the ring current and tail current contributions [51]. WINDMI models the PRC as flowing partially in the ring current and closing through the region 2 current I_2 (refer to eq. (2.7)). In the model, the time scale and dynamics of the I_2 current are very close to the time scale and dynamics

of the geotail current I. Here we have lumped together the effects of the region one and two currents, I_1, I_2, and the geotail current and proceed to use αI of the geotail current to represent both. The contributions from the magnetopause and tail current systems are given by:

$$Dst_{mp} = a * \sqrt{P_{dyn}}, \tag{2.16}$$

$$Dst_t = \alpha I(t), \tag{2.17}$$

where Dst_{mp} is the perturbation due to the magnetopause currents and Dst_t is the magnetic field contribution from the tail current $I(t)$ which is modeled by WINDMI as I. P_{dyn} is the dynamic pressure exerted by the solar wind on the earth's magnetopause. We used two values 15.5 and 7.26 for a as estimated by Burton et al. [13] and O'Brien and McPherron [15], respectively (hereafter referred to as Burton's and O'Brien's formula). Burton's formula estimates the contribution of Dst_{mp} to be more than twice that estimated by O'Brien's formula. The factor α is an unknown geometrical factor that is optimized, and accounts for the errors introduced due to the assumed structure of the geotail. The simulated Dst is then given by:

$$Dst_{windmi} = Dst_{rc} + Dst_{mp} + Dst_t. \tag{2.18}$$

Using this expression to calculate the simulated Dst, we optimized the physical parameters of the WINDMI model and the geometrical factor α for all the events again. The optimized ring current decay periods are compared against the results from section 2.4.1. We obtain two set of results one each for the two values of a.

Estimates for the value of α can be inferred from calculations similar to as given in the popular book edited by Kamide and Chian [1] (pp. 364-365), but we chose to make it an optimization variable here. We optimized the value of α for the event that occurred on days 325-335 in the year 2001. The best fit value was found to be 4.3 per MA. This value of α was then kept fixed for all the other events. It was estimated that, assuming the PRC and near-earth cross tail currents are confined within 18 to 06 local time sector in the nightside,

at a distance of 6 R_E, each MA of the combined currents produce a disturbance of 10.4 nT on the earth's surface at low latitudes [1]. Since the effects of the individual currents are unclear, we leave a comparison of our values of α with the values found in the book by Kamide and Chian [1] for future work.

2.5.1 Results After Including Magnetopause and Tail Current Contributions

Following the procedure that we used in reporting our results in subsection 2.4.2, we discuss all the 13 individual events again but now using the results from the modified Dst formula. The ring current decay times τ_{rc} estimated after including the contributions from other magnetospheric currents for all the events for both the Dst_{mp} values is compiled in Table 2.2. All the 26 plots generated and discussed in this section have been included as auxiliary material.

Days 158-166, 2000. Addition of contributions from the magnetopause currents now allow the modeled Dst to predict the SSC at the start of this event. During the medium activity following the period of northward decay, optimization results using O'Brien's formula for Dst_{mp} fit the data better compared to those using Burton's formula. The best fit using the modified Dst formula yields decay times of 26 hours using Burton's formula and 21.4 hours using O'Brien's formula. Any positive deflections for the estimated Dst values is only due to contributions from Dst_{mp}, since tail current $I(t)$ and ring current (represented by W_{rc}) weaken the earth's magnetic field and are negative contributions in the model. The SSC is slightly under predicted by O'Brien's formula while it is over predicted by Burton's formula.

Days 195-202, 2000. For the Bastille day storm, during the storm main phase the contribution from the tail current to the Dst exceeds that of the ring current for both the formulas. The ring current seems to take a longer time to energize and also decays on a much longer time scale. Figure 2.10 shows the Bastille day event optimized using Burton's formula for Dst_{mp} contribution. Possible errors in the results due to missing or unusable data is highlighted in this event. Solar wind proton density and velocity data as measured by ACE was missing during the main phase of this storm. We retained the previous data

Table 2.2: Ring current decay rates obtained after including the effects of magnetopause and tail current contributions to Dst simulated by WINDMI. $\tau_{rc}Burt$ stands for the ring current decay rates obtained using Burton's formula for Dst_{mp}. $\tau_{rc}O'Brien$ are the result using O'Brien's values for Dst_{mp}.

Event day	$\tau_{rc}Burt$ (in hours)	$\tau_{rc}O'Brien$(in hours)
$2000-158$	26.0	21.4
$2000-195$	39.8	31.5
$2000-260$	43.4	34.27
$2001-100$	40.7	26.92
$2001-225$	33.4	23.25
$2001-264$	30.6	26.0
$2001-325$	37.9	33.35
$2002-80$	40.7	25.0
$2002-142$	54.4	38.86
$2002-245$	39.8	36.1
$2004-93$	22.3	14
$2005-6$	54.48	36.11
$2007-81$	34.3	24.16

value for all the solar wind measurements that are either missing or corrupted. The Dst_{mp} values during the initial and main phase are probably underestimated due to our choice of data reconstruction, as the quiet time values are generally smaller. This leads to the over estimation of the Dst peak value as can be seen in fig. 2.10.

Days 260-265, 2000. As described earlier, optimizing using just the ring current contribution from the WINDMI model against Dst data resulted in the delayed prediction of the Dst peak location. The faster dynamics of the tail current help the modified Dst optimized results to predict the rise and peak location of the Dst more accurately. The tail current also helps in capturing the moderate activity during days 262-263.

Days 100-105, 2001. The main phase is not that well reproduced by the modified Dst for the first event in 2001. The faster decay time of the tail current helps the modified Dst formula in predicting the minimum in Dst earlier than what was possible with just Dst from the WINDMI ring current. This was one of the events for which the IMF B_z did not turn northward abruptly after the peak in Dst. The results for the main phase suggest that there are probably more physical processes which still need to be accounted for to get a more realistic representation.

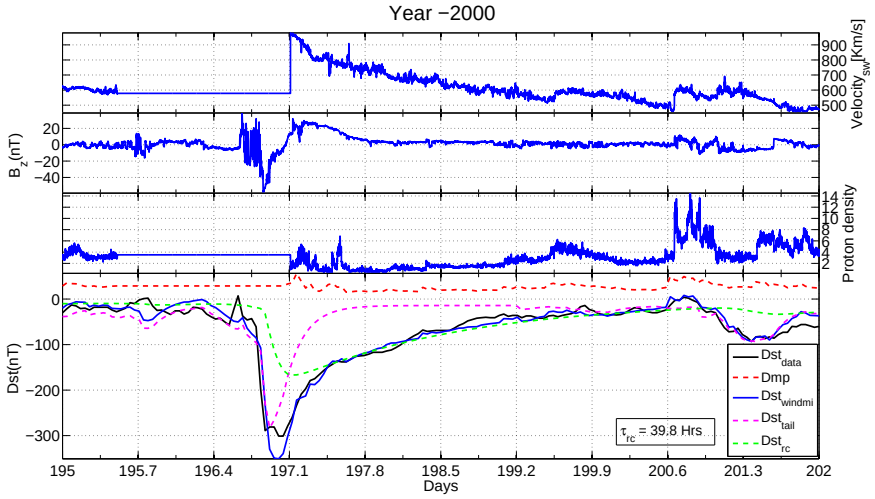

Fig. 2.10: Modeled results using the modified WINDMI Dst formula, for the storm that occurred on days 195-200 in the year 2000. Colored lines correspond to individual contributions to the storm-time Dst from the major currents in the magnetosphere. Burton's formula was used to estimate Dst_{mp}.

Days 225-235, 2001. The simulated results for the event is shown in fig. 2.11. Burton's formula was used in estimating Dst_{mp} for the figure. Several improvements over the previous model can be immediately observed. The sudden storm commencement due to the initial pressure enhancement caused by the shock front is reproduced. Minor variations in Dst index are now better predicted as the contribution from faster recovering tail currents and P_{dyn} are included. IMF B_z was northward for a long time for this event and changes in the Dst_{mp} are well correlated with fluctuations in the recovery phase. The model over predicts the Dst peak by -40 nT using Burton's formula. The ring current recovery time τ_{rc} is predicted to be 33.4 hours, which is significantly higher than the 16.5 hours estimated for the same event by matching against Dst for period 1 (refer Table 2.1). The induced disturbance due to the ring current is predicted to be a lot higher in this case, but is compensated by the associated increase in magnetopause currents due to pressure enhancements.

Using O'Brien's formula for this event the model underpredicts the SSC before the start of the main phase. But it does not overpredict the value of minimum Dst. The ring current recovery time for O'Brien's formula is 23.25 hours, which is less than what

was predicted using Burton's formula, but still substantially higher than that predicted by matching during period 1 for all the Dst indices shown in Table 2.1. The modified Dst for this case captures the moderate event on days 232-234.

Days 265-268, 2001. The best fits for this event, as discussed in section 2.4.2, showed that the WINDMI model predicts a delay in the Dst peak location. The modified Dst formula now predicts a peak location which is much closer to measured data. This is another event where the faster dynamics of the tail current helps in predicting the Dst minimum earlier and closer to the measured Dst, than was possible with just Dst from WINDMI ring current energy.

Days 80-88, 2002. In section 2.4.1 we discussed that for the event on days 80-88 (2002), the effect of increased solar wind forcing observed on day 84 was not properly predicted by the optimized Dst results. Pressure enhancements during the recovery phase of the Dst index helped in the faster recovery of the measured Dst. The modified model result using Burton's coefficient for Dst_{mp} for this event is shown in fig. 2.12. The modeled values suggest that the ring current particles lost energy on a much longer time scale as indicated by the effective τ_{rc} value of 40.7 hours. Complete deenergization of the ring current particles was not possible before the moderate storm, which is now fairly well reproduced.

With the modified Dst using Burton's formula we are able to obtain the moderate event on day 84. Using O'Brien's formula the results for the main phase and early recovery phase of the storm are good, but the ring current recovers a lot faster and is not able to capture this drop in Dst during the recovery phase as the ring current appears to have deenergized completely when using O'Brien's formula.

Days 142-146, 2002. This was the third event with a gradual northward turning of the IMF B_z. The ring current takes much longer to decay compared to the tail current. The best fit using Burton's formula for Dst_{mp} suggests a longer decay time for the ring current. The different contributions of P_{dyn} as estimated by Burton and O'Brien can now be seen to affect the SSC at the start of this storm. Both the formulas under predict the SSC but Burton's values are closer to data while contributions from O'Brien's values barely

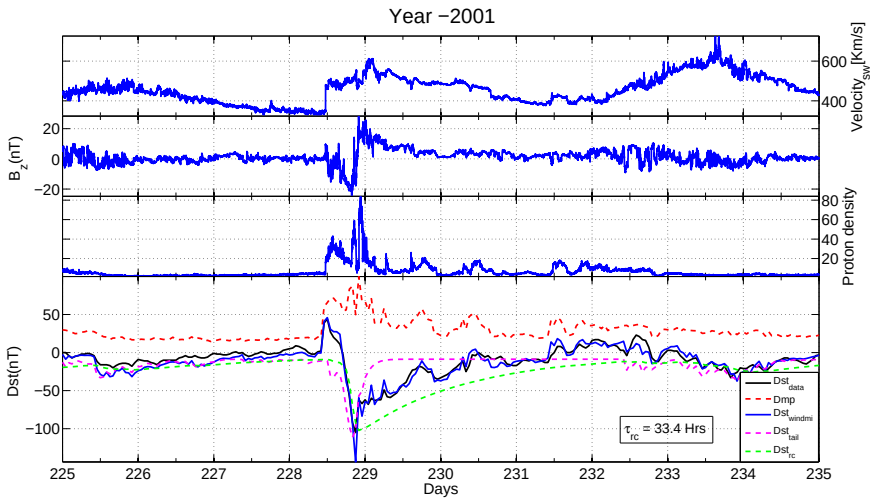

Fig. 2.11: The best fit for the storm that occurred on days 228-233 in the year 2001 obtained using the modified model. Colored lines correspond to individual contributions to the storm-time Dst from the major currents in the magnetosphere. Burton's formula was used to estimate Dst_{mp}.

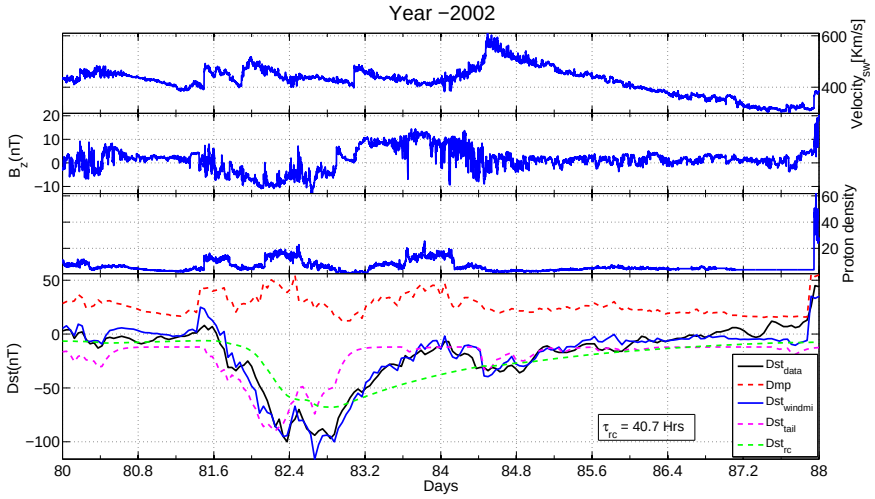

Fig. 2.12: Modeled Dst results for a storm that occurred on days 80-88, 2002 using the modified WINDMI Dst expression. Colored lines correspond to individual contributions to the storm-time Dst from the major currents in the magnetosphere. Burton's formula was used to estimate Dst_{mp}.

show positive values of Dst.

Days 245-260, 2002. This multistage event had an associated SSC at the start of the storm. Using Burton's formula for Dst_{mp}, the SSC is captured but not with O'Brien's. Ring current recovers on a much longer time scale. The duration of this event was from days 245-260. The period of northward IMF was only during the initial recovery phase of the second and largest peak in Dst between days 249-250.

Days 93-95.5, 2004. The fast decay of the tail current helps in predicting both the main event and second event following the storm. The ring current decay times predicted are smaller especially for Dst_{windmi} with O'Brien's formula for this particular event.

Days 6-10, 2005. This is one of the smallest events that we have analyzed. Due to missing solar wind proton density data during the storm main phase, the contribution of Dst_{mp} is probably underestimated. The modified Dst values significantly over predict the Dst values during the main phase of the storm as well as the minimum in Dst. The decay period is modeled well.

Days 81-88, 2007. This was the only CIR event that matched our criterion in the period under consideration. In section 2.4.3, where we discussed the increase in decay times from the best fits for Dst and Dst^*, we expected that the fast decay during the period of northward IMF during the recovery phase was probably due to pressure enhancement and not actual ring current recovery.

The results in this section indicate that the variation can be accounted for by the faster time scale Dst_{mp} and tail current dynamics. The ring current decay times predicted are 34.13 hours and 24.16 hours for Burton's and O'Brien's formulas, respectively. Using O'Brien's formula we are not able to get the positive excursions of the Dst index during the initial recovery phase from 82.7-83.2 days. Proton density data were lost during the start of the storm and the probable underestimation of Dst_{mp} during that period probably causes under prediction of Dst values over that period.

2.5.2 Discussion

The results compiled in Table 2.2 suggest that the ring current may decay on a much

longer time scales than previously estimated. Contributions from the tail current combined with contributions from other fast ring current decay mechanisms can account for the initial fast decay of the Dst index. For all cases, using O'Brien's formula for estimating Dst_{mp} gave us values for τ_{rc} which were less compared to using Burton's formula.

The errors in the modeled Dst can be expected to increase during events when southward IMF B_z slowly turns northward, as the fast decay of Dst is due to both the tail current recovery as well as the flow out loss of particles from the ring current during B_z south. In addition, it has been reported that when the component of the E_y due to VB_s is large, the ram pressure contribution to Dst might decrease [52], leading to a greater variation in our results.

To test the performance of the model we use an out of sample event, a strong storm that occurred between $6-10$ April 2000 with a peak Dst of -300 nT. The IMF B_z turns northward abruptly after the peak in Dst is observed, but only for a short duration after which it turns southward again and gradually fluctuates to its quiet time values. The optimized WINDMI results for this event are shown in fig. 2.13. This event was studied in detail by Tsyganenko and Sitnov, who included contributions from all the major magnetospheric systems in estimating their Dst index [51]. They report symmetric ring current and tail current decay times that are similar to our results. The tail current contributions as estimated by WINDMI during the main phase of this storm exceeds that of the ring current which agrees with their findings.

Our results for this out of sample event, suggest significantly higher values for both ring current and tail current contribution to Dst for this event, as compared to the results of Tsyganenko and Sitnov [51]. The higher estimate could be due to the faster ring current decay mechanisms which are not included in our model, may have a major role to play during the early recovery phase of the storm. Since the decay rates of the tail current and these faster mechanisms are approximately on the same time scale, the optimization algorithm boosts the tail current contributions to compensate for the absence of other effects.

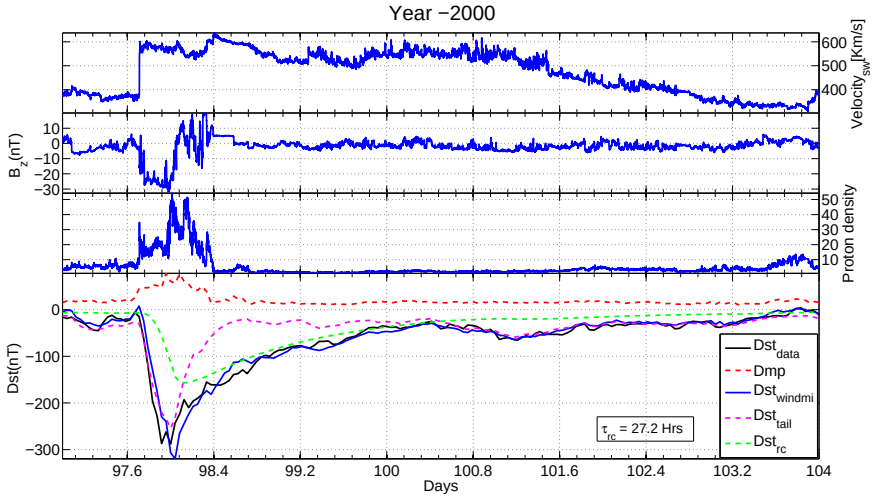

Fig. 2.13: Modeled Dst results for a storm that occurred on $6-10$ April 2000. IMF B_z was not northward for any significant length of time during the early recovery phase of this storm. Burton's formula was used to estimate Dst_{mp}.

2.6 Conclusion

In this work we analyzed thirteen events in the recent solar cycle where the IMF B_z was northward during the early recovery phase of the storm. We separated our investigation into two parts, first we tested to confirm whether a two phase decay is evident even for abrupt northward IMF turning cases, and second, we included contributions from different magnetopsheric current systems to the measured Dst index. The analysis indicates that the two phase decay is evident even after abrupt northward turning of IMF B_z during the storm recovery phase. This result agrees with the findings of O'Brien and McPherron, who also observed a similar recovery trend for both northward and southward B_z cases [49].

We used two different formulas for estimating the pressure corrected Dst^*, one due to O'Brien and the other using Burton's coefficients. The two contributions for Dst_{mp} were also included in calculating the total contribution from the magnetospheric currents to the Dst index. Optimization with the two different formulas for the modified Dst gives mixed results as far as the extent of the contributions from Dst_{mp} is concerned. The optimization algorithm chooses the amount of contribution from each component in order to get a best fit to the total Dst. At this time we cannot conclude whether one formula should be preferred over the other.

The storm-time dynamics of individual contributions of principal external field sources to the ground magnetic disturbance is modeled well by including the contributions from magnetopause and tail currents in the WINDMI model. Our results support the findings of previous researchers, who report that the tail current and the ring current dynamics are the most important contributors to the Dst index [37, 51, 53, 54]. In most cases, the tail field even exceeds the contribution due to the ring current during the main phase, but then quickly subsides, leaving the symmetrical ring current as the dominant source through the rest of the recovery phase. The modeled results indicate longer decay times for the symmetric ring current.

The WINDMI model can be improved further by accounting for the different loss processes of the ring current particles by making τ_{rc} a function of the factors affecting the individual loss processes. Results obtained in this paper were made under the assumption that particles are trapped on closed field lines when the IMF B_z becomes northward.

Chapter 3

The Influence of Solar Wind-Magnetosphere Coupling Functions on the Dst Index

3.1 Introduction

The *Dst* index is an indicator of the change in magnetic field observed on the surface of the earth due to changes in the magnetospheric current systems. The ring current and the cross-tail current produce southward or negative perturbations to the dipole magnetic field measured on the surface of the earth. In addition to this, compression of the day-side magnetosphere from solar wind dynamic pressure contributes to positive perturbations of the *Dst* index. The largest changes in the *Dst* occur during the geomagnetic storms triggered by Coronal Mass Ejections (CME's) and Corotating Interaction Regions (CIR's) originating from the sun.

How much of the measured *Dst* is due to each of the different current systems remains to be understood. It has been reported previously [33, 37, 51, 53, 54] that the tail current is a major contributor to the *Dst* index during storm time, although the relative contribution is still debated [55, 56]. The *Dst* decay during a geomagnetic storm is observed to follow a two-phase pattern, a period of fast decay followed by a phase where the *Dst* returns to its quiet time value gradually [32–34]. The role of different current systems and decay mechanisms in explaining this observation is still under investigation.

Alexeev et al. [37] and Maltsev et al. [54] report equal or even higher tail current contribution to *Dst*. According to Turner et al. [55] and Baker et al. [57], there is only a 25% contribution of magnetotail current (Dt) to *Dst* during magnetic storms. On the other hand, Maltsev and Ostapenko [56] suggest about 80% contribution of Dt, although using a slightly different definition of the tail current to Turner et al. [55]. Liemohn et

al. [50] and Kozyra et al. [14] reported a strong agreement between modeled Dst due to ring current and observed Dst fields, which implies a minimal (even no) contribution of Dt to Dst at the maximum of the storm main phase. Tsyganenko and Sitnov [51] found out that the symmetric and the tail current are the most significant contributors to the Dst index. According to them, in most cases the tail field even exceeds that of the ring current during the main phase, but then quickly subsides, leaving the symmetrical ring current as the dominant source through the rest of the recovery phase.

Using the low order physics-based WINDMI model, we showed earlier that the two phase decay could be explained by including the magnetic field due to the geotail current [58]. The geotail current contributed significantly to the initial fast decay while the ring current provided the slower decay in the Dst signal. We also found that by including the magnetic contributions from the magnetopause currents through the calculation of the Dmp [13], the resultant total calculated Dst from the WINDMI model showed a remarkably high fidelity to the actual measured Dst for thirteen 3-10 day long geomagnetic storm events that occurred between 2000-2007.

The solar wind velocity, interplanetary magnetic field and proton density all play a role in transferring energy into the magnetosphere. However, an exact coupling function quantitatively describing the contribution from the solar wind parameters is as yet undecided. The y-directed component of the solar wind rectified electric field E_y as seen in the earth's reference frame given by $\mathbf{v} \times \mathbf{B}$ is commonly used as a coupling function, called the rectified vB_s coupling function, but there are many others. Newell et al. derived a coupling function and compared its performance against many other functions [24], while several other researchers have produced other coupling functions [26–28, 59].

The performance of these coupling functions have often been compared with regard to their correlation to the Dst index. In Spencer et al. we compared the performance of the rectified, Siscoe and Newell coupling functions in re-producing and predicting the westward auroral electrojet AL index as well as the Dst index [29]. There we found that the rectified vB_s performed more robustly in prediction compared to the others, but did not perform as

well in re-producing the AL indices when doing post-event analysis.

In this work we perform a post-event analysis of a selection of large geomagnetic storms between 2000-2002 to test the capability of different coupling functions in reproducing the Dst index faithfully. We also analyze the contributions from different current systems as implied by the qualitative differences between the coupling functions. In order to do this we scale the coupling functions appropriately, and use each of them in turn to drive the WINDMI model. The WINDMI model is tuned computationally with a genetic algorithm for the best fit against the measured Dst index. The resulting curves are then analyzed and compared between the different inputs. Because the WINDMI model has been successfully used in the past [30, 31] to analyze substorm dynamics and the AL index signatures associated with solar wind forcing, we used the AL index as a secondary constraint so that the coupling functions could be differentiated when the Dst indexes were similar.

The coupling functions that are evaluated in this work differ from each other in the solar wind parameters used in their calculation. We chose these coupling functions because they have been reported to correlate well to the Dst index. For the rectified vB_s, only the solar wind parameters v_x and B_z are considered geoeffective. For the coupling functions given by Siscoe and Newell, the solar wind dynamic pressure, IMF B_y, IMF B_z and the solar wind velocity v_x are considered geoeffective. The coupling function due to Borovsky is based on the idea that the solar wind dynamic pressure and Mach number largely controls the rate of reconnection at the nose of the magnetopause, and therefore controls the rate of energy transfer into the magnetosphere.

This paper is divided into sections as follows. In section 3.2, we give a description of the WINDMI model. The formulas for the calculation of the Dst index due to different contributors is also given in this section. In the third section, we describe briefly how the model is optimized for different storm data. In section 3.4, we give a synopsis of the different coupling functions that are evaluated in the remainder of the work. In section 3.5, we give a short explanation of the storm events chosen and the criteria we required for their inclusion. In section 3.6, we explain our results and categorize the behavior of the different coupling

functions. Finally, we summarize and conclude the work in section 3.7.

3.2 Description of the WINDMI Model

The plasma physics based WINDMI model uses a solar wind based voltage, V_{sw}, generated by a particular solar wind-magnetosphere coupling function, to drive eight ordinary differential equations describing the transfer of power through the geomagnetic tail, the ionosphere and the ring current. The WINDMI model is described in some detail in Spencer et al. [30]. The equations of the model are given by:

$$
\begin{aligned}
L\frac{dI}{dt} &= V_{\rm sw}(t) - V + M\frac{dI_1}{dt}, && (3.1)\\
C\frac{dV}{dt} &= I - I_1 - I_{\rm ps} - \Sigma V, && (3.2)\\
\frac{3}{2}\frac{dp}{dt} &= \frac{\Sigma V^2}{\Omega_{\rm cps}} - u_0 p K_{\parallel}^{1/2}\Theta(u) - \frac{pVA_{\rm eff}}{\Omega_{\rm cps}B_{\rm tr}L_y} - \frac{3p}{2\tau_E}, && (3.3)\\
\frac{dK_{\parallel}}{dt} &= I_{ps}V - \frac{K_{\parallel}}{\tau_{\parallel}}, && (3.4)\\
L_I\frac{dI_1}{dt} &= V - V_I + M\frac{dI}{dt}, && (3.5)\\
C_I\frac{dV_I}{dt} &= I_1 - I_2 - \Sigma_I V_I, && (3.6)\\
L_2\frac{dI_2}{dt} &= V_I - (R_{\rm prc} + R_{A2})I_2, && (3.7)\\
\frac{dW_{\rm rc}}{dt} &= R_{\rm prc}I_2^2 + \frac{pVA_{\rm eff}}{B_{\rm tr}L_y} - \frac{W_{\rm rc}}{\tau_{\rm rc}}. && (3.8)
\end{aligned}
$$

The nonlinear equations of the model trace the flow of electromagnetic and mechanical energy through eight pairs of transfer terms. The remaining terms describe the loss of energy from the magnetosphere-ionosphere system through plasma injection, ionospheric losses and ring current energy losses.

In the differential equations the coefficients are physical parameters of the magnetosphere-ionosphere system. The quantities L, C, Σ, L_1, C_I, and Σ_I are the magnetospheric and ionospheric inductances, capacitances, and conductances, respectively. A_{eff} is an effective aperture for particle injection into the ring current, that on the dusk side merges with what

is known as the Alfven layer [42]. The Alfven layer is defined to be the separatrix between two sets of drift trajectories, one comprising open drift paths extending from the magnetospheric tail to the dayside magnetopause and another, nearer set consisting of closed drift paths, encircling the earth [44]. The resistances in the partial ring current and region-2 current, I_2 are R_{prc} and R_{A2}, respectively, and L_2 is the inductance of the region-2 current. The coefficient u_0 in eq. (3.3) is a heat flux limiting parameter.

The energy confinement times for the central plasma sheet, parallel kinetic energy and ring current energy are τ_E, τ_k, and τ_{rc}, respectively. The effective width of the magnetosphere is L_y and the transition region magnetic field is given by B_{tr}. The pressure gradient driven current is given by $I_{ps} = L_x(p/\mu_0)^{1/2}$, where L_x is the effective length of the magnetotail. The output of the model are the AL and Dst indices, in addition to the magnetospheric field aligned currents. The effect of delayed density enhancements of the plasma sheet due to solar wind forcing, which will add a time variation to C in eq. (3.2), is not included in the present model.

The parameters are combined appropriately into a vector P_d where $d = 18$. They can be estimated using semi analytical techniques or they can be considered as variables that need to be optimized within physically allowable ranges to fit the data for a given storm. Some parameters, e.g. Ω_{cps}, L, have been approximated analytically using the Tsyganenko magnetic field model and then allowed to vary over a physically reasonable range of values as explained in Spencer et al. [30].

The current I_1 used in the model is that portion of the field aligned region 1 current that maps to the nightside central plasma sheet and is considered to be part of the substorm current wedge that produces the westward auroral electrojet. The Auroral AL index now follows as a magnetic field perturbation ΔB_{AL} from the ambient terrestrial field due to the westward electrojet current that flows in the E-layer ($\sim 90 - 120km$) in the nightside ionosphere. We estimate the relation between I_1 and the AL index by assuming that the current I_1 is related linearly to the AL index by a constant of proportionality [30].

The portion of the Dst index due to plasma energy stored in the ring current W_{rc} is given by the Dessler-Parker-Sckopke (DPS) [46, 47] relation:

$$Dst_{rc} = \frac{\mu_0 W_{rc}(t)}{2\pi B_E R_E^3}, \tag{3.9}$$

where B_E is the earth's surface magnetic field along the equator.

The ring current energy (W_{rc}) injection terms in the WINDMI model are the first and second terms on the right hand side of eq. (3.8). The current I_2 is a region 2 current that leaves the ionosphere on the dawn side, closes in the ring current and returns to the ionosphere on the dusk side. This secondary loop of current has a self inductance L_2 and drives a current through the partial ring current resistance R_{prc} as well as the resistance of the region 2 current loop footprint R_{A2}. The Joule heating through the resistance R_{prc} energizes the ring current particles. The particles injected across the effective aperture A_{eff} is another source of ring current energy. The ring current energy in the model is assumed to be lost by particles drifting out of orbit or by charge exchange processes at a rate proportional to τ_{rc}. The various loss processes of the ring current particles can be represented by a time dependent τ_{rc}, but we chose a fixed value for it during a given storm.

The major current systems that are considered to contribute to the total Dst in the magnetosphere are: (1) the magnetopause currents shielding earth's dipolar magnetic field; (2) the symmetric ring current; (3) the partial ring current; and (4) the cross-tail current along with the closure currents on the magnetopause. All these currents cause magnetic perturbations on the earth's surface. We add the magnetopause current and cross tail current contributions in addition to the WINDMI ring current in order to calculate the complete simulated Dst index. The quiet time values for each current system is included in the WINDMI model calculations. Following Patra et al. we have lumped together the effects of the region one and two currents, I_1, I_2, and the geotail current and proceed to use αI of the geotail current to represent both [58]. The contributions from the magnetopause and tail current systems are given by:

$$Dst_{mp} = a * \sqrt{P_{dyn}}, \tag{3.10}$$

$$Dst_t = \alpha I(t), \tag{3.11}$$

where Dst_{mp} is the perturbation due to the magnetopause currents and Dst_t is the magnetic field contribution from the tail current $I(t)$ which is modeled by WINDMI as I. We used the value of $a = 15.5$ as suggested by Burton et al. [13]. For a look at the results obtained by using the value ($a = 7.25$), as estimated by O'Brien and McPherron [15], refer to the work done by Patra et al. [58]. P_{dyn} is the dynamic pressure exerted by the solar wind on the earth's magnetopause. The simulated Dst is then given by:

$$Dst_{windmi} = Dst_{rc} + Dst_{mp} + Dst_t. \tag{3.12}$$

Estimates for the value of α can be inferred from calculations similar to as given in book edited by Kamide and Chian [1] (pp. 364-365), but we chose to make it an optimization variable here. We optimized the value of α for the event that occurred on days 325-335 in the year 2001. This event was chosen because the different storm phases were distinct. The best fit value was found to be 4.3 per MA. This value of α was then kept fixed for all the other events.

3.3 Optimization of the WINDMI Model

The variable coefficients in the WINDMI model are L, M, C, Σ, Ω_{cps}, u_0, I_c, A_{eff}, B_{tr}, L_y, τ_E, $\tau_{||}$, L_I, C_I, Σ_I, L_2, R_{prc}, R_{A2}, τ_{rc}, and α. These parameters are constrained to a maximum and a minimum physically realizable and allowable values and combined to form a 18-dimensional search space $S \subset \mathbb{R}^{18}$ over which optimization is performed.

To optimize the WINDMI model, we use one form of the genetic algorithm [48] to search the physical parameter space in order to minimize the error between the model output and the measured geomagnetic indices. The optimization scheme was used to select

a parameter set for which the outputs from the WINDMI model most closely matches the AL index and the Dst index simultaneously. For this work we are interested in the features of the Dst index, so we have chosen a higher bias of 0.8 for Dst while the AL index was given a weighting of 0.2 in order to maintain a reasonably good fit. There is a strong direct correlation between solar wind parameters and the AL index during geomagnetic activity over hour time scales, so a coupling function that does well on predicting the Dst index but produces a poor AL index can be differentiated from the others.

The performance of the algorithm is evaluated by how well the average relative variance (ARV) and correlation coefficient (COR) compare with the measured indices. The average relative variance gives a good measure of how well the optimized model tracks the geomagnetic activity in a normalized mean square sense, while the correlation coefficient shows how well the model tracks the geomagnetic variations above and below its mean value. The ARV is given by:

$$ARV = \frac{\Sigma_i (x_i - y_i)^2}{\Sigma_i (\bar{y} - y_i)^2}, \tag{3.13}$$

where x_i are model values, y_i are the data values, and $\bar{y}$ is the mean of the data values. In order that the model output and the measured data are closely matched, ARV should be closer to zero. A model giving $ARV = 1$ is equivalent to using the average of the data for the prediction. If $ARV = 0$ then every $x_i = y_i$. ARV values for the AL index above 0.8 are considered poor for our purposes. ARV below 0.5 is considered very good, and between 0.5 to 0.7 it is evaluated based upon feature recovery. For the Dst index, and ARV of 0.25 is considered good. Below $ARV = 0.15$ is considered very good, and evaluation is based on mostly qualitative criteria.

The correlation coefficient COR is calculated against the AL index only as a measure of performance but not used as a cost function in the optimization process. COR is given by:

$$COR = \frac{\Sigma_i (x_i - \bar{x})(y_i - \bar{y})}{\sigma_x \sigma_y}. \tag{3.14}$$

COR is better when closer to 1. It indicates anti-correlation if the value is close to

-1. σ_x and σ_y are the model and data variances, respectively. Typically, if the correlation coefficient is above 0.7, the performance is considered satisfactory for the physics-based WINDMI model. Both the ARV and COR values are calculated over the period when the most geomagnetic activity occurs. When these criteria are observed to be acceptable, the optimization process is assumed to have reached convergence.

3.4 Solar Wind Coupling Functions

The input into the WINDMI model is a voltage that is proportional to a combination of the solar wind parameters measured at L1 by the ACE satellite. These parameters are the solar wind velocity v_x, the IMF B_x, B_y, B_z, and the solar wind proton density n_{sw}, measured in GSM coordinates. The input parameters are time delayed to account for propagation of the solar wind to the nose of the magnetosphere at $10R_E$ as given in Spencer et al. [30].

In order to properly compare the Dst produced by each input processed by the WINDMI model, we adopted a procedure to normalize the coupling functions, which we discuss in section 3.6.1. This ensured that only the qualitative differences contributed to the different Dst curves produced by each function. Additionally, the same offset voltage of 40 kV was added to each scaled coupling function to drive the ring current and tail current total contribution to the Dst index to nominally 2-5 nT of activity during quiet times. In the next five subsections we describe each coupling function in turn, and we make note of some key similarities and differences between them.

3.4.1 Rectified IMF Driver

The first input function chosen for this study is the standard rectified vB_s formula [45], given by:

$$V_y = v_{sw} B_s^{IMF} L_y^{eff} (kV), \tag{3.15}$$

$$V_{sw}^{Bs} = 40(kV) + V_y, \tag{3.16}$$

where v_{sw} is the x-directed component of the solar wind velocity in GSM coordinates, B_s^{IMF} is the southward IMF component, and L_y^{eff} is an effective cross-tail width over which the dynamo voltage is produced. For northward or zero B_s^{IMF}, a base viscous voltage of 40 kV is used to drive the system.

3.4.2 Siscoe Driver

The second input function is using a model given by Siscoe and coworkers for the coupling of the solar wind to the magnetopause using the solar wind dynamic pressure P_{sw} to determine the standoff distance [59–61]. This model includes the effects of the east-west component of the IMF through the clock angle θ_c. The Siscoe formula is given by:

$$V_{sw}^S(kV) = 40.0(kV) + \nu_s 57.6 E_{sw}(mV/m) P_{sw}^{-1/6}(nPa), \tag{3.17}$$

where

$$E_{sw} = v_{sw} B_T \sin^2(\theta_c/2), \tag{3.18}$$

is the solar wind electric field with respect to the magnetosphere and the dynamic solar wind pressure $P_{sw} = n_{sw} m_p v_{sw}^2$. Here m_p is the mass of a proton. The magnetic field strength B_T is the magnitude of the IMF component perpendicular to the x-direction. The IMF clock angle θ_c is given by $\tan^{-1}(B_y/B_z)$. The solar wind flow velocity v_{sw} is taken to be approximately v_x. This voltage is described by Siscoe et al. as the potential drop around the magnetopause that results from magnetic reconnection in the absence of saturation mechanisms [59]. ν_s is a scaling factor used to normalize the varying part of the Siscoe coupling function to a specific reference level.

3.4.3 Newell Driver

The third input function is based on a recent formula from Newell et al. that accounts for the rate of merging of the IMF field lines at the magnetopause [24]. The Newell formula is given by:

$$\frac{d\Phi_{MP}}{dt} = v_{sw}^{4/3} B_T^{2/3} \sin^{8/3}(\theta_c/2). \tag{3.19}$$

This formula is re-scaled to the mean of (3.15) and given the same viscous base voltage of 40 kV. We obtain the re-scaled Newell formula as:

$$V_{sw}^{N} = 40(kV) + \nu_n \frac{d\Phi_{MP}}{dt}, \tag{3.20}$$

where ν_n is a scaling factor used to normalize the varying part of the Newell coupling function to a specific reference level.

3.4.4 Newell Driver with Dynamic Pressure

In Newell et al., it was found that a modification of the Newell coupling function, $p^{1/2} d\Phi_{mp}/dt$, yielded better correlation results with the Dst [24]. We call this modified coupling function the Newell-P function which is then produced as:

$$V_{sw}^{NP} = 40(kV) + \nu_{np} p^{1/2} \frac{d\Phi_{MP}}{dt}, \tag{3.21}$$

where ν_{np} is a scaling factor used to normalize the varying part of the Newell-P coupling function to a specific reference level.

3.4.5 Borovsky Control Function

We also evaluate the performance of the control function derived by Borovsky which expresses the dayside reconnection rate in terms of upstream solar wind parameters [26]. According to Borovsky, the reconnection rate at the dayside magnetopause is governed by four local plasma parameters: B_m, B_s, ρ_m, and ρ_s, where B_m is the z-component of the magnetic field strength in the magnetosphere just outside the reconnection site, B_s is the z-component of the magnetic field strength in the magnetosheath just outside the reconnection site, ρ_m is the plasma mass density in the magnetosphere just outside the reconnection site, ρ_s is the plasma mass density in the magnetosheath just outside the reconnection site. The

magnetosheath parameters are then cast in terms of the upstream solar wind parameters through the use of the Rankine Hugoniot relations.

The coupling function for solar wind/magnetospheric coupling is derived as:

$$R = 0.4\mu_0^{1/2} sin(\theta/2)\rho_o v_o^2(1 + 0.5M_{ms}^{-2}) \times \quad (3.22)$$
$$(1+\beta_s)^{-1/2}.[C\rho_o + (1+\beta_s)^{-1/2}\rho_m]^{-1/2} \times$$
$$[(1+\beta_s)^{1/2} + 1]^{-1/2},$$

where ρ_o is the mass density of the solar wind upstream of the bow shock, v_o is the velocity of the solar wind upstream of the bow shock, C is the compression ratio of the bow shock, β_s is the plasma-β value of the magnetosheath plasma near the nose, and M_{ms} is the magnetosonic Mach number of the solar wind. Expression (3.23) is supplemented with

$$\beta_s = 3.2 \times 10^{-2} M_A^{1.92}, \quad (3.23)$$
$$C = \{[1/4]^6 + [1/(1 + 1.38log_e(M_A))]^6\}^{-1/6}, \quad (3.24)$$
$$M_{ms} = v_o((B_o^2/\mu_o\rho_o) + 5P_o/3\rho_o)^{-1/2}, \quad (3.25)$$
$$M_A = v_o(\mu_o\rho_o)^{1/2}/B_o. \quad (3.26)$$

We normalize the Borovsky function with a scaling parameter ν_b to scale it to a specific reference level. With this scaling modification the Borovsky function becomes proportional to a voltage yielding:

$$V_{sw}^B = 40(kV) + \nu_b R. \quad (3.27)$$

In using the Borovsky coupling function, we neglected the thermal pressure P_o in eq. (3.25) following Borovsky and used only the dynamic pressure to calculate V_{sw}^B [26]. We did this because we expected that the ratio of thermal pressure to dynamic pressure to be low in the solar wind for the events under consideration.

3.4.6 Discussion on Coupling Functions

First, while the rectified vB_s includes only the southward component of the IMF B_z, the Newell function has the total IMF perpendicular to the x-direction in GSM, and so effectively has $B_y^{2/3}$ when $B_z = 0$. This explains the contribution of B_y to coupling energy into the magnetosphere from this function. For purely northward IMF the Newell function evaluates to zero. The velocity component in the Newell formula is only the x-directed velocity of the solar wind, which is the same as the rectified vB_s, but it is raised to an exponent of 4/3.

The Siscoe coupling function has the solar wind velocity and IMF B_T raised to the exponent 1, but additionally includes the solar wind dynamic pressure explicitly, $\rho_{sw}v_x^2$, which changes the exponent of the solar wind velocity to effectively 2/3. This modification to the exponent for v_x parallels that of the Newell function which also has some solar wind dynamic pressure built into it via pressure balance with the earth's dipolar magnetic field. The Newell-P coupling function includes the solar wind dynamic pressure explicitly. We chose to include the Borovsky coupling function because of its good correlation to the Dst index reported by Borovsky [26]. This function attributes the solar wind coupling efficiency into the magnetosphere largely to solar wind dynamic pressure and Mach number, which is related to the reconnection rate during southward IMF.

3.5 Storm Events

A set of 13 events were selected by Patra et al. where the IMF Bz turned northward abruptly after the peak in Dst index was observed [58]. Under these conditions it is assumed that the flow out losses will be less dominant and the recovery would be governed by the contributions from the tail current and ring current. For this study, we have chosen six events out of the initial 13 events reported, based on the particular characteristics of each storm. First, we wanted to rate the performance of each coupling function on the storms where the WINDMI model performed best. Second, on some storm events there was data drop out, especially in the proton density over the main phase of the storm.

The six events chosen for this study from the previous group of 13 are 1) Days 158-166,

2000; 2) Days 258-266, 2000; 3) Days 225-235, 2001; 4) Days 325-335, 2001; 5) Days 80-88, 2002; and 6) Days 245-260, 2002. In addition to the six out of the 13 events from Patra et al. [58], we also selected the October 2000 and April 2002 storm events used previously in Spencer et al. [29], since now the inclusion of the tail current contribution and the Dmp contribution adds to the interpretation of the calculated Dst.

The solar wind parameters in GSM coordinates required as input to the WINDMI model are obtained from the ACE satellite orbiting at the L1 point between the sun and the earth. Missing or unusable data from the satellite measurements was dealt with by retaining the previous data value whenever the data was unusable. Hourly AL and Dst index values were obtained from the World Data Center for Geomagnetism, Kyoto website.

3.6 Results and Discussion

3.6.1 Normalization Methods

The rectified vB_s produces a voltage when v_xB_z is multiplied by an effective width of the magnetosphere of $10R_E$. The Siscoe coupling function already produces a voltage in its original form. The Newell function and Borovsky function are not suitable in their original formulation for use with the WINDMI model.

The importance of the normalization is that it determines the overall energy that is transferred to the magnetosphere as predicted by a particular coupling function. During various attempts, we tried normalizing the Siscoe, Newell, and Borovsky functions to the rectified vB_s (which we will from here on refer to as vBs), first against the vBs mean throughout a year, then against the vBs mean during a storm event, then against the vBs maximum during a storm event. Using these three methods produced some variation in how well each coupling function performed, but did not drastically alter the results.

The most effective method was found to be by using the Siscoe coupling function as a separate basis for normalization. We normalized the Newell, Newell-P, and Borovsky coupling functions to the mean of the Siscoe function over a storm interval as reference. The vBs coupling function was not included. This is because the vBs was most different

from the other four coupling functions in most of the cases, going to zero whenever the IMF Bz has no southward component. This resulted in large time periods over the data set when vBs was zero (with a 40 kV offset), while the other coupling functions were all somewhat similarly active. The normalization scheme used ensured that the final form of the coupling functions were different from each other only qualitatively, or in curve shape only, as far as possible. As much potential bias with regards to total energy content of each coupling function was removed.

To calculate the different normalization constants, we set ν_s for the Siscoe driver to be 1. Then we evaluate ν_n, ν_{np}, and ν_b, the normalization factors for each of the Newell, Newell-P, and Borovsky functions as:

$$\nu_X = (V_{sw}^X - 40kV)\frac{\overline{V_{sw}^S - 40kV}}{\overline{V_{sw}^X - 40kV}}, \tag{3.28}$$

where X represents the one of the Newell, Newell-P, or Borovsky functions, V_{sw}^S is the Siscoe voltage over a storm interval, while $\overline{V_{sw}^X - 40kV}$ represents the mean of the appropriate function to be normalized over the same interval.

3.6.2 Overall Results

With the different normalization schemes, the optimized results are summarized in Table 3.1 and Table 3.2. A full set of figures for every result is provided with the supplementary material for this paper.

Each coupling function is evaluated over a storm interval using the vBs function as a reference for performance quality. When the results were good, the correlation values for such cases exceed 0.8, so the correlation coefficient does not provide a meaningful measure for comparison between the coupling functions. The ARV values for good fits to the Dst index are mostly below 0.2, differences below this value are also difficult to identify quantitatively. For this reason qualitative comparisons are done for the most part. The AL index is used to evaluate whether the geotail current signatures are allowable.

The vBs function does well enough on all the events to be a reliable coupling function

Table 3.1: Summary of results using different coupling functions with the WINDMI model fit against the measured Dst index. In the columns under each input, the ARV values of the calculated Dst and the measured Dst index for each coupling function is listed. The final column shows the categorization of the result for the storm event.

Year	Storm Event	Dst_{min}	vBs	Siscoe	Newell	Borovsky	Newell-P	Cat
2001	225-235	-105	0.082	0.16	0.13	0.12	0.25	I
2001	325-335	-221	0.037	0.033	0.038	0.071	0.042	I
2002	245-260	-181	0.083	0.11	0.1	0.18	0.13	I
2000	158-166	-90	0.16	0.26	0.13	0.17	0.45	II
2000	Oct 3-7	-182	0.088	0.066	0.062	0.13	0.2	II
2000	258-266	-201	0.083	0.17	0.12	0.18	0.16	II
2002	80-88	-100	0.069	0.23	0.09	0.17	0.055	II
2002	Apr 15-24	-149	0.18	0.29	0.15	0.11	0.15	II

Table 3.2: Summary of results using different coupling functions with the WINDMI model fit against the measured AL index. In the columns under each input, the ARV values of the calculated AL and the measured AL index for each coupling function is listed. The final column shows the categorization of the result for the storm event.

Year	Storm Event	Dst_{min}	vBs	Siscoe	Newell	Borovsky	Newell-P	Cat
2001	225-235	-105	0.33	0.39	0.34	0.45	0.42	I
2001	325-335	-221	0.57	0.63	0.7	0.74	0.67	I
2002	245-260	-181	0.45	0.43	0.4	0.57	0.57	I
2000	158-166	-90	0.32	0.39	0.32	0.62	0.86	II
2000	258-266	-182	0.64	0.69	0.56	0.78	0.89	II
2000	Oct 3-7	-201	0.3	0.31	0.32	0.4	0.36	II
2002	80-88	-100	0.23	0.51	0.35	0.59	0.25	II
2002	Apr 15-24	-149	0.35	0.37	0.33	0.48	0.59	II

for analysis or predictive purposes. The only function that does as well as vBs overall is the Newell coupling function. However, in some cases, one of the other coupling functions fit the features of the storm event better than either vBs or Newell. For this reason, we attempted to further refine the evaluation process to get a better representation of the qualities of each coupling function.

The results can be divided into two categories. In the first category (Category I), we have storm events where the coupling functions look qualitatively different from each other, but using any coupling function resulted in a good fit to the measured Dst data. The events that fall into this category are marked with a "I" in the last column of Table 3.1. In these events, the relative contributions from each current system due to the different inputs remained roughly the same through the optimization process. We also observed that for the storms in this category, the reproduced Dst curves were very good, having an ARV of less than 0.2 in most instances. These storm events were characterized also by their classical nature in that the onset, main phase, and decay phase are distinct. We discuss one of these events, between days 225-235 in 2001, in a subsection below.

The results in Category I do not point to reasonable conclusions about the confidence in each of the coupling functions. In a prediction scheme, using each input with a version of the model that is optimized to that particular function on past training data will result in similar looking Dst curves. The best AL index reproduction was obtained mostly by vBs. The dynamics of the AL index and therefore the implied geotail current dynamics were acceptable for all storms in this category.

For another category of events, the results were more uncertain. In some cases, the optimization process was able to find different states of the WINDMI model that compensated for the differences between the coupling functions so as to produce a good fit to the measured Dst data, but in some cases, either such states did not exist, or the AL index results were not acceptable even though the Dst index was reproduced well.

In the case of days 158-166, 2000, for instance, the WINDMI model was not able to produce a good fit to the Dst index with the Newell-P function. Further, the AL Index was

unusually poor when using this coupling function, giving an ARV of 0.86, compared to vBs giving 0.32. In another instance, for the April 15-24 storm event, the Borovsky function produced the best Dst index. However, both the Borovsky function and the Newell-P function produced very poor AL indices compared to vBs and $Newell$. We classify these cases as falling into Category II. We discuss two of these events, days 80-88, 2002, and the April 15-24, 2002 storm, in a subsection below.

The results in Category II are difficult to interpret. In this case, if the input coupling functions look different, the output Dst curves will be different, and each Dst curve may predict different levels of geomagnetic activity over 6-8 hour time scales. In addition, it becomes unclear which version of the optimized model to use for prediction purposes. One possible compromise is to use multiple versions of the model and predict different possible geomagnetic storm scenarios.

The most significant difference in contributions from the ring current and geotail current systems was observed because of the use of vBs versus the other three coupling functions. Since vBs turns off during periods when there is no southward component of the IMF, the total energy content in vBs will be low. In contrast, all the other coupling functions use $B_T = \sqrt{B_z^2 + B_y^2}$, so they do not necessarily turn off during these periods. We found that the overall ring current contribution when using vBs was lower than the tail current contribution for these cases. The other coupling functions produce Dst curves with a higher ring current contribution compared to the tail current contribution. This is most noticeable in the main phase and decay phase of a storm. The direct interpretation is that the optimized model compensates for lack of total available energy in the coupling function by emphasizing the tail current component when using vBs.

The second difference was the fact that the solar wind dynamic pressure is incorporated into the Siscoe, Borovsky, and Newell function (both Newell and Newell-P), but not in vBs. Since the solar wind dynamic pressure is also accounted for in the calculation of Dmp, this indicates two possible ways through which the solar wind dynamic pressure contributes. One way is through the depression of the magnetopause, increasing the magnetopause currents

and subsequently giving a positive contribution to Dst through the Dmp component, and secondly through control of the reconnection rate at the magnetopause, as suggested by Borovsky [26]. This path results in a negative contribution to Dst through either the tail current component or the ring current component.

In the following subsections the results in each category are discussed in more detail. For each category we choose some representative events, and proceed to discuss some of its features.

3.6.3 Category I Events

The representative case for this type of result is the storm event occurring between days 225-235, 2001. To illustrate the differences between the input coupling functions during this event, we show a comparison of the Newell, Newell-P, and Borovsky functions against the vBs and Siscoe coupling function for this storm in fig. 3.1. The Siscoe function is shown in both the upper and lower panels of the figure in order to aid in comparison.

During this event, the initial period between days 226-228 had density data drop-out, but this did not affect the results because the density data became available before the sudden storm commencement occurred. The reproduced Dst for this event using each of the different coupling functions is shown in fig. 3.2.

For this storm the sudden storm commencement (SSC), the main phase, and the decay phase, are very well defined. The SSC is captured due to the Dmp contribution, and the ring current and tail current contributions both decay after northward turning occurs as shown by vBs, and their relative strengths do not vary significantly from using different coupling functions. The Dmp takes care of most of the short time scale Dst dynamics after northward turning. The AL index is fit well (see supplementary material) with all the coupling functions for this particular event. Similar results were obtained for the rest of the Category I events. One exception to this was the results from days 245-260 with the Newell-P coupling function, where the geotail current contribution was larger than the geotail currents produced by the other coupling functions. The AL prediction for the storm on days 325-335, 2001 are affected by the loss of solar wind data during the initial phase

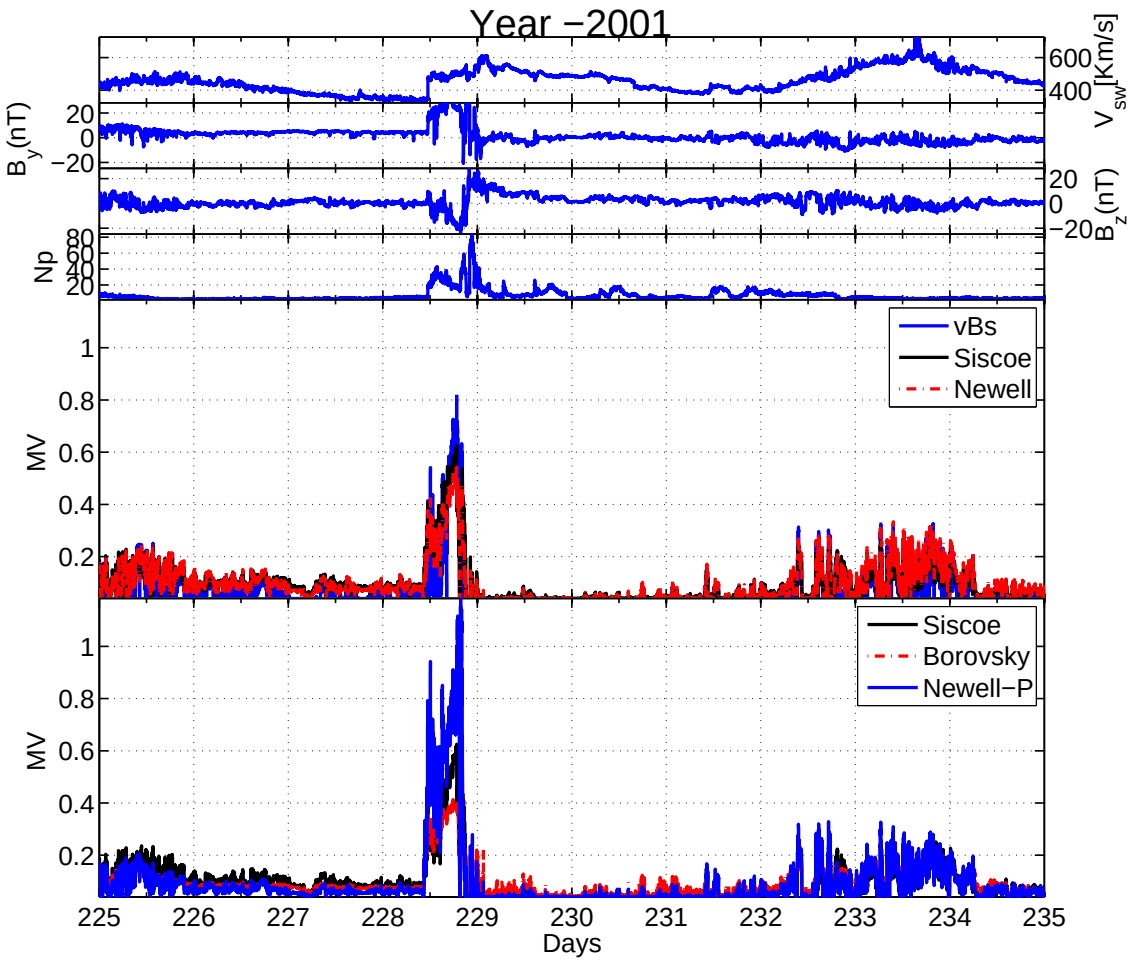

Fig. 3.1: The coupling functions compared for the Category I representative event occurring in year 2001, Days 225-235. Panels 1-4 show the input ACE data. Panel 5 shows the vBs and Newell coupling functions compared to the Siscoe function as reference. Panel 6 shows the Borovsky and Newell-P coupling functions compared to the Siscoe function as reference.

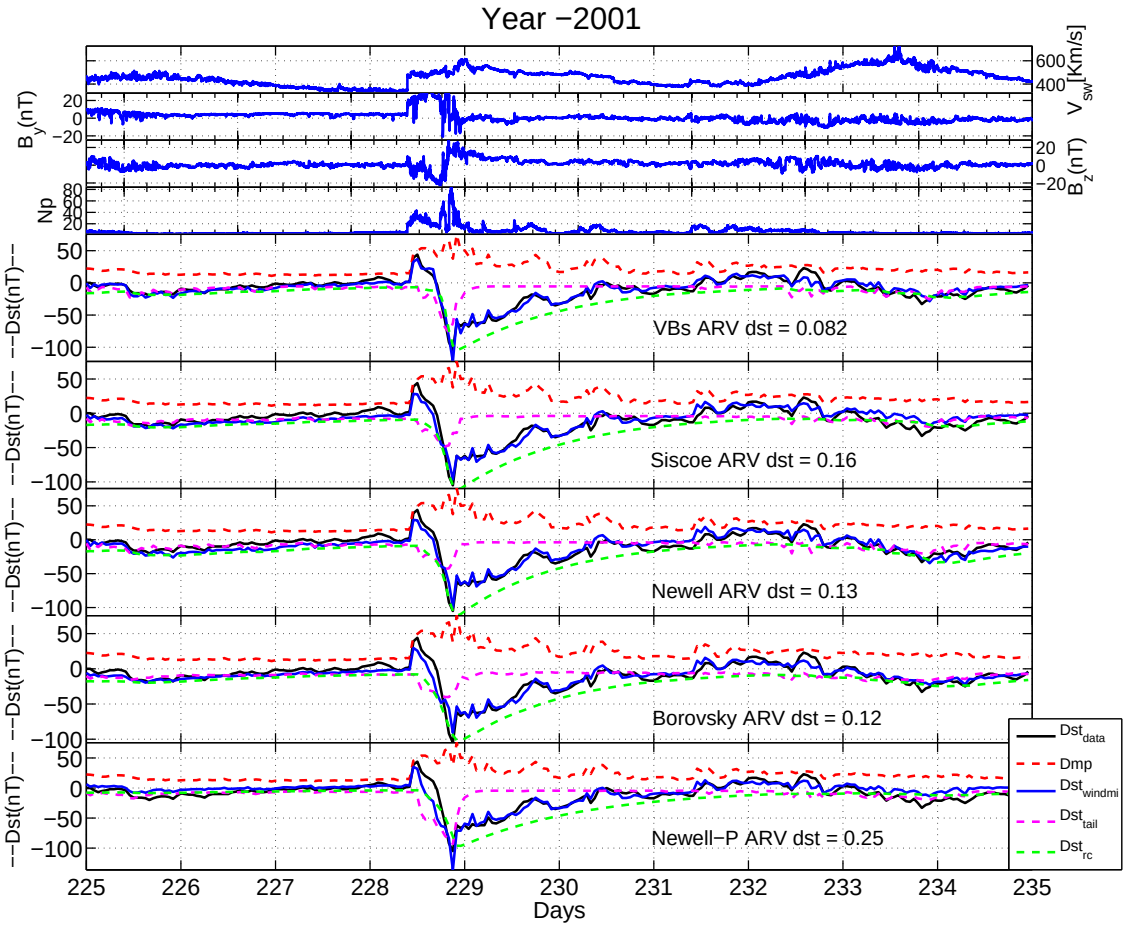

Fig. 3.2: The optimized *Dst* index fits for each coupling function compared for the Category I representative event occurring in year 2001, Days 225-235. Panels 1-4 show the input ACE data. Panels 5-9 show the *Dst* fits for each coupling function.

of the storm. This is reflected in the ARV numbers of AL for the storm as shown in Table 3.2.

3.6.4 Category II Events

In this category, the coupling functions are qualitatively different, and the results also look different. Here we have events on which some coupling functions do well, but others do not. We choose two events that fall into this category, the April 15-24, 2002 storm, and days 80-88, 2002, to illustrate some of the differences in performance.

The first representative event for this category is the April 15-24, 2002 geomagnetic storm. For this event, the input coupling functions are shown in fig. 3.3. The output Dst curves for this event are shown in fig. 3.4. On this event, the Siscoe coupling function produced the poorest Dst index, compared to vBs or Newell fits.

There are qualitative differences between the fits to the measured Dst produced by vBs, Newell and Borovsky coupling functions, but in our estimation they are good fits, with slightly different qualitative features. The slight differences in tail current and ring current contributions differ between each coupling function, which gives rise to the overall difference in the calculated Dst between them. Note that the Dmp contribution due to magnetopause currents are exactly the same whatever coupling function is used.

For the Borovsky and Newell-P functions, during the storm main phase, days 107-108, the AL index was very poorly represented. This is an obvious characteristic entirely due to the shape of the two coupling functions, but the physical reasons are unclear. The other coupling functions, including Siscoe, produce good AL indices. From fig. 3.3, it can be seen that the Siscoe and Newell functions are very close in overall character, but their resulting Dst curves are very different. The reason is that the Dst curves are a result of time integration of the input coupling functions, so the slight differences that are sustained over 12-24 hours become amplified.

We contrast the results of the April storm with the results obtained for the storm event on days 80-88, 2002. For this event, the input coupling functions are shown in fig. 3.5. The output Dst plots for all the different coupling functions are shown in fig. 3.6.

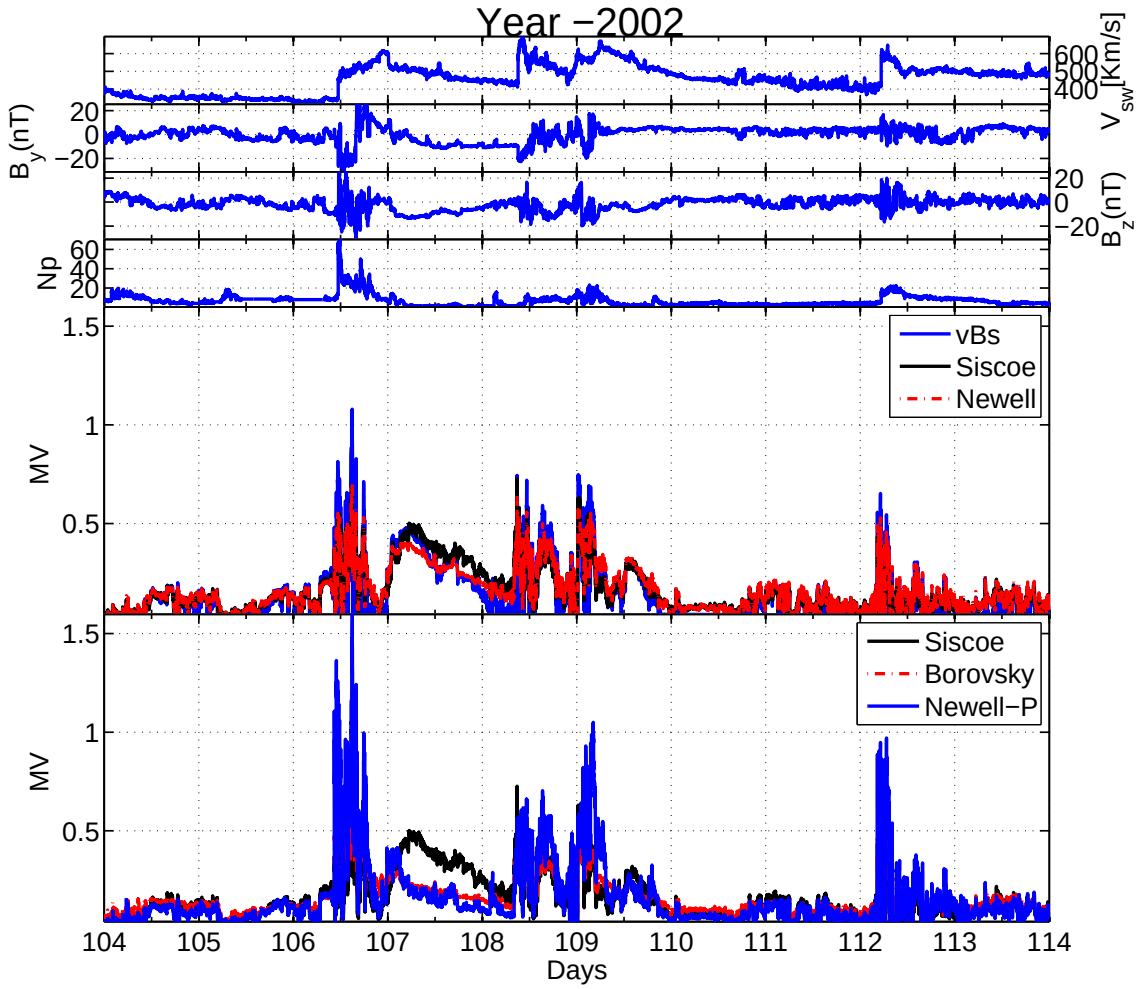

Fig. 3.3: The coupling functions are compared for the Category II representative event occurring in year 2002, on Days 104-114 (April 15 - 24, 2002). Panels 1-4 show the input ACE data. Panel 5 shows the vBs and Newell coupling functions compared to the Siscoe function as reference. Panel 6 shows the Borovsky and Newell-P coupling functions compared to the Siscoe function as reference.

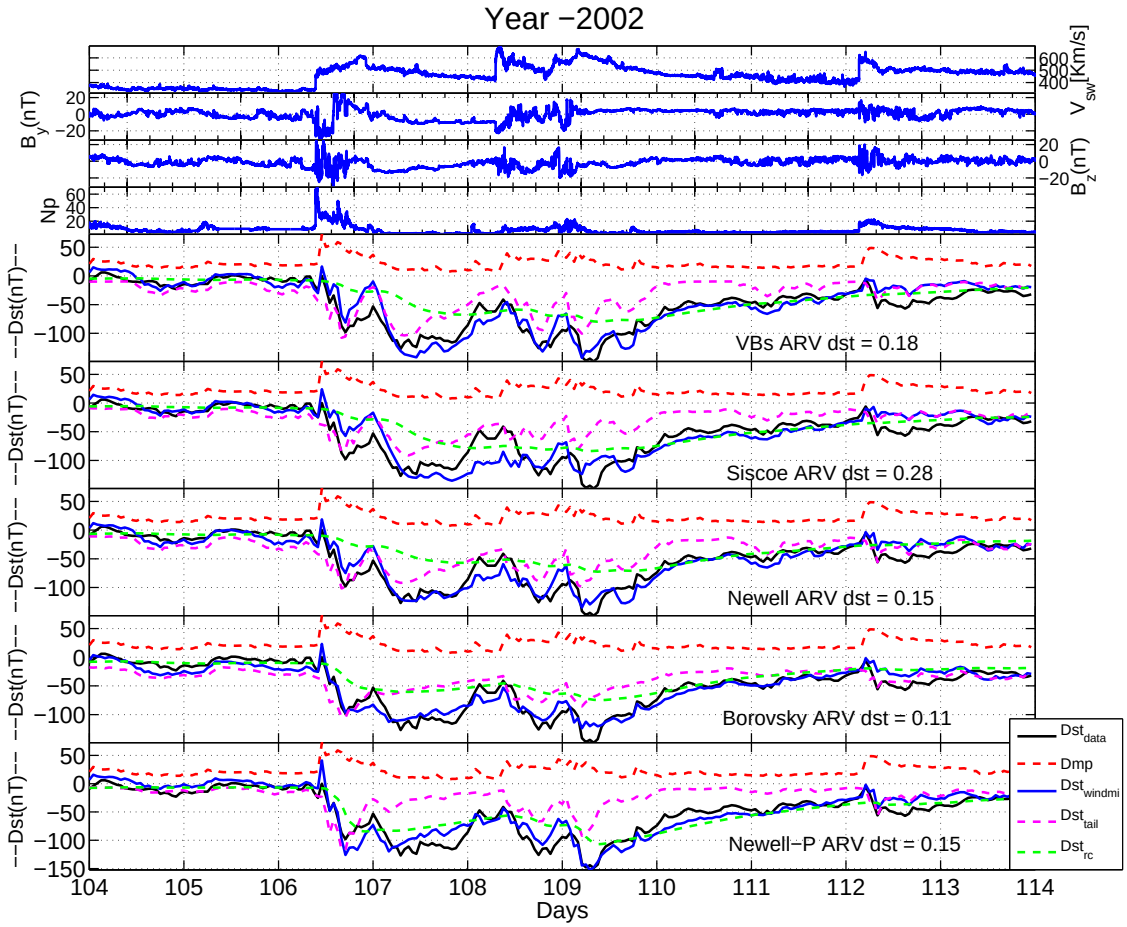

Fig. 3.4: The optimized *Dst* index fits for each coupling function compared for the Category II representative event occurring in year 2002, Days 104-114 (April 15 - 24, 2002). Panels 1-4 show the input ACE data. Panels 5-9 show the *Dst* fits for each coupling function.

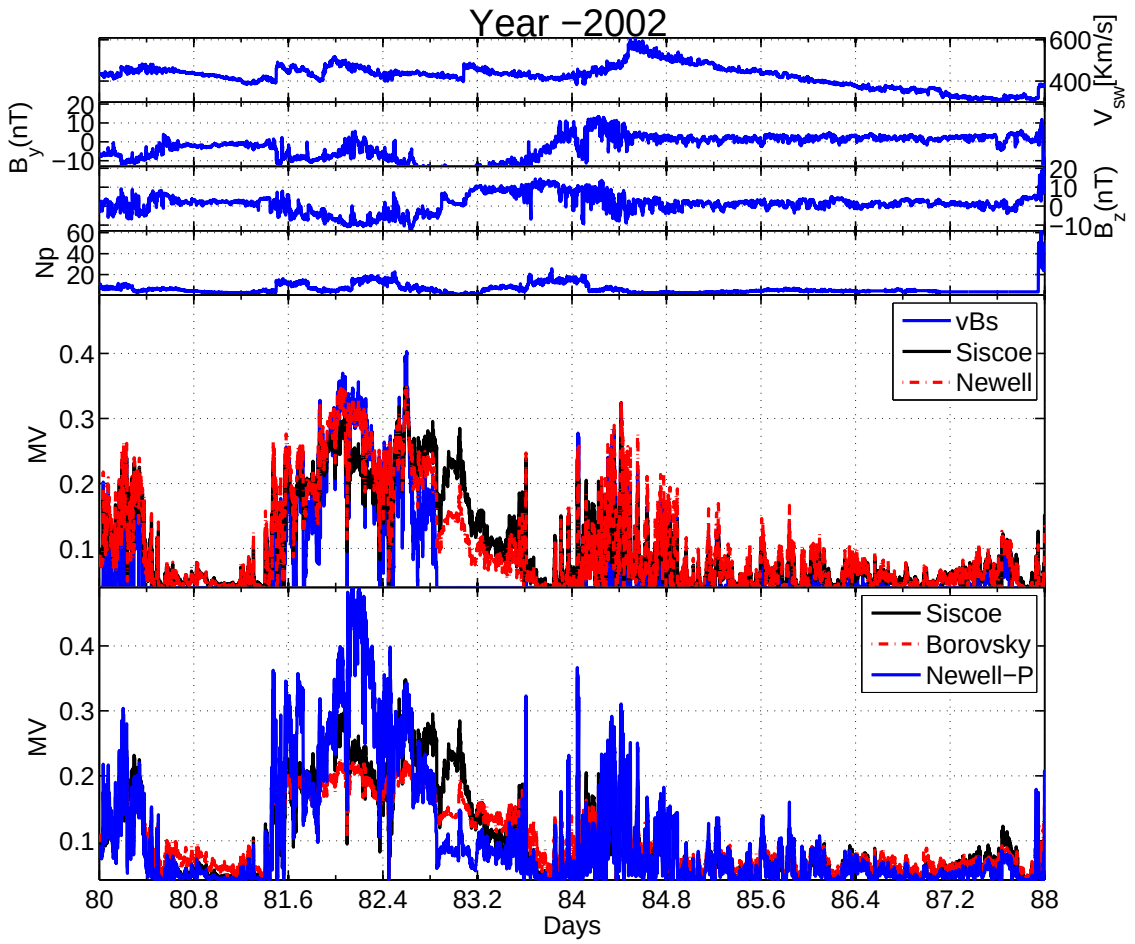

Fig. 3.5: The coupling functions compared for a Category II event that occurred in year 2002, Days 80-88. Panels 1-4 show the input ACE data. Panel 5 shows the vBs and Newell coupling functions compared to the Siscoe function as reference. Panel 6 shows the Borovsky and Newell-P coupling functions compared to the Siscoe function as reference.

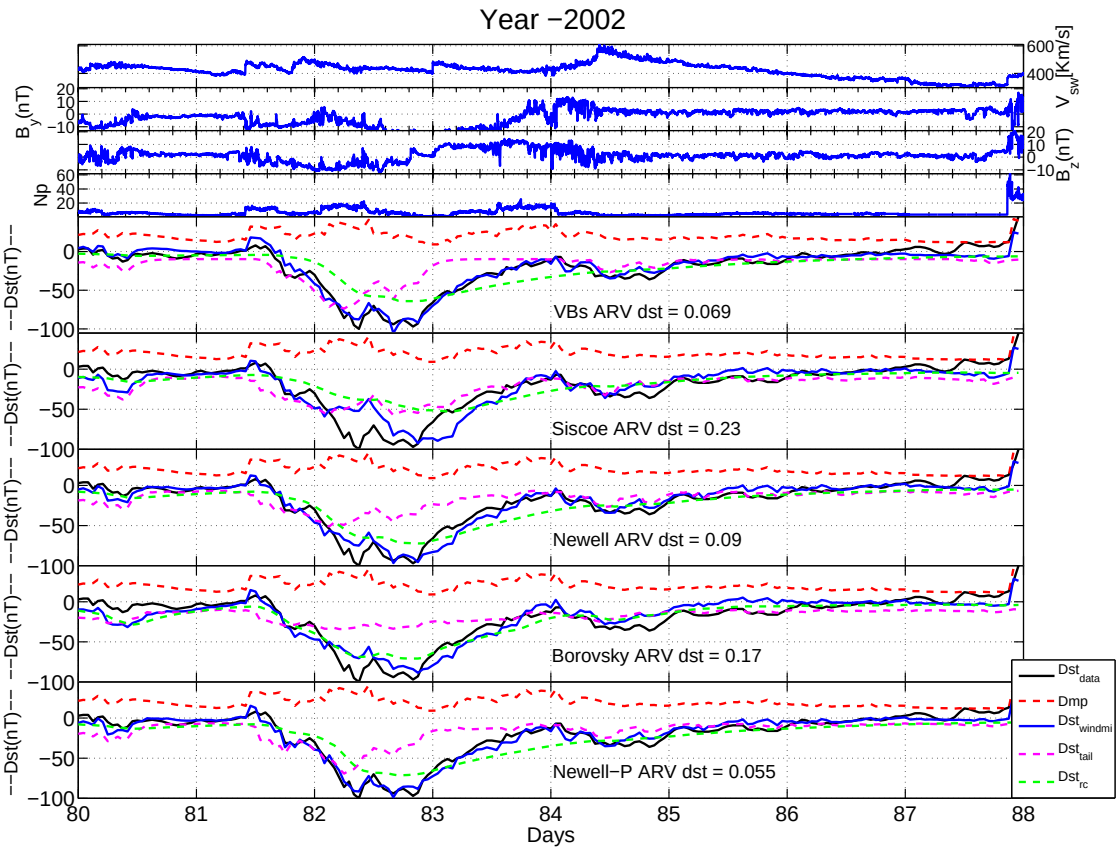

Fig. 3.6: The optimized *Dst* index fits for each coupling function are compared for the Category II event that occurred on Days 80-88, in the year 2002. Panels 1-4 show the input ACE data. Panels 5-9 show the *Dst* fits for each coupling function.

For this event, the surprising result was that the Newell-P function produced an output Dst as good as that of the Dst produced by vBs, and in fact slightly better than the Newell coupling function. In this instance the factor $p^{1/2}$ contributes favorably to improve the Newell-P Dst calculation. Again, for this storm event, the Siscoe coupling function does not produce a good fit both in Dst as well as AL. During this storm, between days 81-82, a density enhancement drives the AL index significantly, because only the Newell-P function amplifies the effect enough to fit the observed AL index.

The Borovsky coupling function, although producing a good fit, is worse than vBs, Newell, and Newell-P. All of the four coupling functions that produce good fits have slight differences in the tail to ring current contributions, the Borovsky function producing the highest ring current component. Since the Borovsky, Newell, and Newell-P functions are normalized to the Siscoe coupling function, their energy content is fixed relative to the Siscoe input. The optimization process changes the gain of the WINDMI model in addition to the plasma confinement time constants in order to fit against the data.

Finally, although the Borovsky function produces a good Dst index, it does very poorly on the AL index. For this reason we do not accept the Borovsky result with a high degree of confidence for this event. The Borovsky function produced poor AL index curves in all storm datasets except the October 3-7 2000 storm. The Borovsky function performs well when density enhancements due to shock interfaces are clearly present in the AL and Dst signatures.

3.6.5 Discussion

In both categories of results, the vBs and Newell coupling function produce consistently good fits against the data. There are instances where the Borovsky coupling function performs qualitatively as well these two functions, but there are also instances where it does not. Whenever the result is in Category I, all functions do well, but for the Category II, the Siscoe and Newell-P functions were most inconsistent.

The WINDMI model diverts a portion of the crosstail current into the ionosphere along magnetic field lines (FAC). The AL index therefore becomes proportional to direct solar

wind driving unless substorms are triggered. For this reason a coupling function that does not show the ionospheric current enhancements on hour time scales will not produce a good AL index. The tail current contribution is most closely correlated directly to solar wind activity, with time scale dynamics on the order of 5-20 minutes, while the ring current represents time integrated energy content that is on the order of 6 hours or more. Thus, the fast variations in the Dst are a combination of magnetopause Dmp and tail current dynamics, while the slower variations are due to ring current dynamics.

The relative contributions of the tail current to Dst for the Category I storms is almost similar to the contribution of symmetric ring current to the Dst index in the main phase of the storm. The contribution reduces drastically in the recovery phase, as the tail current recovers quickly in the recovery phase leaving the symmetric current as the dominating contributor. The results for Category II storms are more variable.

Because the vBs function goes to zero during non-southward IMF, the level of energy injection into the ring current is lower with this function over an entire storm than with the Newell function. Because of this, the model produces a larger ring current with the Newell coupling function, and chooses longer decay rates of the ring current during the recovery phase with vBs.

Here we note some questions for which the answers are as yet unclear: 1) Why do the vBs and Borovsky coupling functions, while appealing to different physics, both produce good results in many cases? 2) Why does the inclusion of $p^{1/2}$ to the Newell function produce a bad fit in some cases, but then produce a very good fit in others? 3) Is there a way to get an absolute scale for the energy input instead of using the normalizing procedure used in this work? 4) Is there a conditioning of the magnetosphere from energy injections that explains the differences between Category I and Category II results? Attempts to answer these questions will motivate our future work.

3.7 Conclusions

In this work we have examined several different coupling functions and their influence on the Dst calculated by the low order physics based WINDMI model. We chose events from

the previous set of 13 by Patra et al. [58], and two additional large geomagnetic storms that were studied in Spencer et al. [29]. We found that the qualitative character of each coupling function affected the response of the WINDMI model in multiple but categorizable ways. First, the popular rectified vB_s coupling function stands apart in it's qualitative character, because it turns completely off when there is no southward component of the IMF. The other coupling functions were grouped into a second class. These functions variously depended upon IMF B_z as well as B_y, the IMF clock angle, and the solar wind dynamic pressure.

The optimized model results fell into two categories. In the first category, the storm events were such that although the input coupling functions looked qualitatively different from each other, the output results were good fits to the ground measurements of the Dst index. In the second category, we had different input coupling functions, but the model was able to compensate for the differences in some instances and still produce good fits to the measured Dst indices, while in other cases, it could not. However, if two coupling functions looked very similar, they produced identical results.

Regardless of our classification procedure for the input coupling functions and the categorization of the results, we have been able to draw conclusions as far as the reliability for Dst prediction is concerned. In all cases, the rectified vBs and the Newell coupling function produced consistently good fits to the measured data. This is evident from Table 3.1. The extent to which the IMF B_y included in the Newell coupling function exerts an influence on the results cannot be discerned with the WINDMI model unless there is a way to constrain the level of geotail current contribution from satellite data or perhaps some other technique. In most cases, its inclusion slightly over-emphasizes the ring current contribution and under-emphasizes the geotail current contribution. Further, since the Newell function contains a component of the solar wind dynamic pressure through pressure balance with the magnetic field across the magnetopause, the separation of effects becomes more difficult.

The Siscoe, Borovsky, and Newell-P coupling functions were most inconsistent in their performance. In some events the results using these coupling functions were not good at all,

yet during other events, some of them produced even better fits than either vBs or Newell to the measured data. The reason for this is unclear, but the results suggest that either there is an unknown component needed to modulate the coupling functions to produce better results, or that the state of the global magnetosphere varies from event to event in some way that makes one coupling mechanism preferred over the others.

Chapter 4

Magnetotail Current Contribution to the *Dst* Index Using the MT Index and the WINDMI Model

4.1 Introduction

Geomagnetic storms are typically caused by an increase in the solar wind earth directed velocity (600 - 1000 km/s) and a strongly southward IMF (10-30 nT), under which dayside reconnection is enhanced. During such conditions the earth's ring current, geotail curent, magnetopause currents, and field aligned currents are intensified. The rise and decay of each current system is controlled by the energy coupled into the magnetosphere by the solar wind and the subsequent dynamics of the solar wind driven magnetosphere ionosphere system. The *Dst* index is used as an indicator of the strength of a geomagnetic storm. After removing the effects of current systems other than ring current from the *Dst* index, it can be used as a measure for the ring current intensity.

The time development of the ring current during storms has been studied in the past by different modelling approaches. Ring current models like the Comprehensive Ring Current Model (CRCM) [62, 63] or the Ring current-Atmosphere interaction Model (RAM) [35, 36] model, solve the time-dependent, gyration- and bounce-averaged Boltzmann equation for the phase-space distribution function $f(t, R, \varphi, E, \mu_0)$ of a chosen ring current species. Each species is described by two adiabatic invariants m, K (CRCM) or,equivalently, energy and equatorial pitch angle (RAM). The anisotropic pitch angle dependence of distribution function is calculated from the model.

Global energy balance models, like the models proposed by Burton et al. [13], O'Brien and McPherron [15], and the WINDMI model [30, 64–66], use the solar wind parameters as input to the magnetosphere system, which is then translated to the energization of the

total energy of the ring current particles. The Dessler-Parker-Sckopke (DPS) formula [46,47] is then used to relate the energy to the Dst index. Empirical models like the models of Temerin and Li [67,68], and Asikainen et al. [69] have also been proposed. In addition some predictive models use neural networks to predict the Dst index [70, 71].

The Dst index, being computed from measured magnetometer data on the surface of earth, is also bound to be affected by other major magnetospheric current systems. The contributions of other current systems to the Dst index, have been reported by various authors [2, 50, 51, 69]. In particular, the magnetotail current has been known to contribute significantly to the Dst index [33, 37, 38, 54].

It has been reported that during the recovery phase of a magnetic storm, the Dst decay is controlled by the decay of two different currents: the ring current and the magnetospheric tail current [33,37]. This decay is in addition to all the different ring current losses that affect the decay of the Dst index. Recent work of some researchers indicates that the ring current becomes the dominant Dst source during severe magnetic storms, but during moderate storms its contribution to Dst is comparable with the tail current's contribution [38, 51, 72]. Using magnetic field modeling based on Tsyganenko T89 and T96 magnetic field models, Turner et al. [55] showed that the tail current contribution to the Dst index is on an average about 25%. It is important to note that, since their results are based on the T89/T96 magnetic field models the results only apply to the small and moderate magnetic storms with peak $Dst > -100$ nT where the models are valid.

It has been observed that the Dst decay following a geomagnetic storm shows a two-phase pattern, a period of fast decay followed by a phase where the Dst returns to its quiet time value gradually [32–34]. While the fast decay of the tail current in the early recovery phase can partly explain this observation, various ring current loss processes have also been proposed as an explanation. Liemohn and Kozyra , used idealized simulations of ring current decay to show that for realistic plasma boundary conditions, a two-phase decay can only be created by the transition from flow-out losses when open drift lines are converted to closed ones in a weakening convection electric field resulting in the charge exchange dominance of

ring current loss [35]. In a study by Jordanova et al., it was shown that the fast initial ring current decay is controlled not only by the decreased convection electric field, the dayside outflow through the magnetopause, and the internal loss processes, but also by the time-varying nightside inflow of plasma from the magnetotail [36]. Aguado et al. have proposed that a hyperbolic function describes the decay of Dst index better than the exponential functions, which are generally preferred [73]. Other loss processes have also been proposed as contributors to the storm-time ring current decay: Coulomb collisions between the hot ring current ions and plasmaspheric particles [74, 75]; and ion precipitation into the upper atmosphere due to the strong pitch angle scattering of particles into the loss cone by wave-particle interactions (especially electromagnetic ion cyclotron waves) [34, 76, 77]. Walt and Voss concluded that wave-particle interactions elevate particle precipitation losses to a level capable of producing a rapid initial recovery of the ring current [78].

In a previous work, we quantified the effects of ring current decay mechanisms versus the decay of magnetospheric currents [58]. Geomagnetic storms for which an abrupt northward turning of the IMF Bz right after the peak of the Dst index were chosen and modeled. Under this condition, it is expected that the fast flow out losses will be minimal and the ring current recovery would be mainly due to charge exchange process. The WINDMI model was used to model these storms after including contributions from various magnetospheric currents. In most cases, the tail field exceeded the contribution due to the ring current during the main phase, but then quickly subsides, leaving the symmetrical ring current as the dominant source through the rest of the recovery phase.

In another work, we further quantified the effect of using different solar wind magnetosphere coupling functions on the calculation of the Dst index, and determined the sensitivity of the relative contribution between the ring current and the tail current to functions that employ the IMF By versus the more usual rectified solar wind input [79]. The inclusion of the IMF B_y component in a coupling function slightly overemphasized the ring current contribution and slightly underemphasized the geotail current contribution.

The earth's magnetotail varies in accordance with changing solar wind conditions.

In particular, the night side stretching of the magnetosphere is due to an enhanced tail current. Correctly estimating the level of tail current provides another means of constraining magnetospheric magnetic field models. The intensity of the tail current can be monitored by the latitude of the isotropic boundary of energetic protons which is obtained from energetic particle observations by low altitude satellites [19,69], 2010). Removing the systematic MLT variation in the isotropic boundary gives the MT index which can be used as an indicator of tail current intensity.

In this paper, we use the MT index to determine the contribution of the tail current to the Dst index (Dt). The Dt values inferred are used to impose an additional constraint on the tail current contribution to the modeling of the Dst index by the WINDMI model. In the next section we discuss the MT index and Asikainen et al.'s [69] method to determine the contribution of the tail current to the Dst index in detail. Section 4.3 introduces the WINDMI model and the modeling of magnetospheric currents are discussed. In section 4.5 we show the Dst, AL, and Dt obtained from the WINDMI model. The Dt values obtained from the WINDMI model and the MT index derived Dt values are also compared in this section.

4.2 MT-Index

The extent of nightside stretching of the earth's magnetic field has been a subject of interest for many years [80,81]. Several different measurements have been proposed as proxies to estimate the tail stretching, such as the isotropic boundary (IB). The IB is the latitude which separates the region of the magnetosphere close to the earth on quasi dipolar lines, where protons bounce between mirror points without (or with a low) scattering (adiabatic motion) and the further tailward region where the pitch angle scattering is efficient enough to keep the loss cone full (non-adiabatic behavior) [18,82]. The IB is known to correlate well with the magnetic field inclination at geosynchronous orbit around 00 MLT, and therefore provides a way to monitor magnetotail stretching.

The ion precipitating energy flux maxima (b2i), which generally occurs near the equatorward edge of the main nightside oval, was shown to be associated with the ion isotropy

boundary (IB) [22]. Note, however, that while the b2i index describes the tail stretching it is not directly comparable with the MT index which has been defined differently and is based on particle observations of different energies.

Two particular situations can complicate the relationship between the precipitation maximum (b2i) and IB [23]. First, during the expansion phase of some substorms the protons can be so strongly accelerated in the midtail that their maximal energy flux can be recorded poleward of the true isotropic boundary. Also, during strong substorm activity, a structure of detached strong precipitation (corresponding to high-altitude "nose events" [83]) may appear equatorward of the main body of precipitation [84].

According to the numerical simulations of trajectories of small pitch angle particles done by Sergeev and co-workers [18, 21], the threshold condition for strong pitch angle scattering in the tail current sheet (scattering to the center of loss cone) is approximately as follows:

$$R_c/\rho = B_z^2(GdB_x/dz)^{-1} \leq 8, \tag{4.1}$$

where the equality sign corresponds to the isotropic boundary. Here R_c and ρ are the radius of curvature of the magnetic field line and the particle gyroradius, respectively, and $G = mv/e$ is the particle rigidity. The boundary between the regions of adiabatic and nonadiabatic particle motion in the equatorial current sheet depends only on the equatorial magnetic field and the particle rigidity. If the ratio R_c/ρ exceeds 8, then the particles are not scattered and remain bounding along the field lines.

Donovan et al. have used ion data from 29 DMSP overflights of the Canadian Auroral Network for the OPEN Program Unified Study (CANOPUS) Meridian Scanning Photometer (MSP) located at Gillam, Canada, to develop an algorithm to identify the b2i boundary, named as "optical b2i" in latitude profiles of proton auroral (486 nm) brightness [85]. Using the algorithm proposed by Donovan et al. [85], Meurant et al. find the auroral oval's Equatorial Limit (EL) and consider it as a potential indicator of field stretching and not as a boundary between two physically different regions of the tail [82]. Jayachandran and coworkers have shown that the SuperDARN E-region backscatter in the dusk-midnight sector

is from the region of ion precipitation/proton aurora and that its equatorward boundary coincides with the b2i boundary and can be used as a tracer of the equatorward boundary of the proton auroral oval in the dusk-midnight sector [86, 87].

Sergeev and Gvozdevsky used one month of data from the NOAA-6 satellite to determine the MLT dependence of the IB latitude [19]. They defined the IB as the corrected geomagnetic latitude poleward of which the pitch angle distribution of 80 keV protons becomes isotropic. They constructed a measure of the tail current, the MT-index, by removing the MLT dependence from the measured IB latitudes. Asikainen et al. have used particle precipitation data from low-altitude polar orbiting NOAA/POES 15, 16, 17, and 18 satellites during $1.1.1999 - 31.12.2007$, to identify the isotropic boundary [69]. Using a modified algorithm inspired by Sergeev and Gvozdevsky [19], and after accounting for radiation damage in proton detectors on the MEPED instrument onboard NOAA/POES satellites, the IB values are estimated. The MLT dependence of the IB latitude was removed using expressions appropriate for their dataset rather than using the expressions provided by Sergeev and Gvozdevsky [19]. The IB location for the northern and the southern hemispheres were separately determined. Based on local linear regression techniques, they developed a semi-empirical model to describe the contributions of the ring, tail, and magnetopause currents to the Dcx index. The Dcx index is a corrected version of the Dst index [88]. The modeled expression for the tail current contribution (Dt) was chosen so that the $Dt = 0$ nT when MT = 75.5 (the maximum value of the MT index in the data corresponding to the quietest state of the tail current). The expression obtained was

$$Dt = -5.495 * 10^7 \left[\frac{1}{cos^2 MT} + 2.633\right]^{-7.871},$$

when $MT \leq 75.5°$,

$$Dt = 0, \text{ otherwise.} \tag{4.2}$$

Because the hourly MT values are typically calculated only from a few individual measurements within each hour the MT index has a relatively much larger variance than

the corresponding solar wind parameters and the *Dst* index which are averages computed from 1 min data. Newell et al. showed that the location of the isotropic boundary as measured by the b2i index displays small seasonal and diurnal variation with a range of a couple of degrees [89]. It is expected that a similar variation is present in the MT index as well. We note that such variations may introduce small seasonal and diurnal differences between the Dt computed from the MT index and from the WINDMI model (which does not include seasonal effects other than those related to driving solar wind parameters). However, such differences are expected to be very small compared to the storm time disturbances in the Dt.

4.3 WINDMI Model

The solar WIND Magnetosphere-Ionosphere (WINDMI) interaction model is driven by an equivalent voltage derived from an appropriate solar wind magnetosphere coupling function.

The eight ODEs comprising the WINDMI model are

$$L\frac{dI}{dt} = V_{\rm sw}(t) - V + M\frac{dI_1}{dt}, \tag{4.3}$$

$$C\frac{dV}{dt} = I - I_1 - I_{\rm ps} - \Sigma V, \tag{4.4}$$

$$\frac{3}{2}\frac{dp}{dt} = \frac{\Sigma V^2}{\Omega_{\rm cps}} - u_0 p K_{\parallel}^{1/2}\Theta(u) - \frac{pVA_{\rm eff}}{\Omega_{\rm cps}B_{\rm tr}L_y} - \frac{3p}{2\tau_E}, \tag{4.5}$$

$$\frac{dK_{\parallel}}{dt} = I_{ps}V - \frac{K_{\parallel}}{\tau_{\parallel}}, \tag{4.6}$$

$$L_I\frac{dI_1}{dt} = V - V_I + M\frac{dI}{dt}, \tag{4.7}$$

$$C_I\frac{dV_I}{dt} = I_1 - I_2 - \Sigma_I V_I, \tag{4.8}$$

$$L_2\frac{dI_2}{dt} = V_I - (R_{\rm prc} + R_{A2})I_2, \tag{4.9}$$

$$\frac{dW_{\rm rc}}{dt} = R_{\rm prc}I_2^2 + \frac{pVA_{\rm eff}}{B_{\rm tr}L_y} - \frac{W_{\rm rc}}{\tau_{\rm rc}}. \tag{4.10}$$

The nonlinear equations of the model trace the flow of electromagnetic and mechanical

energy through eight pairs of transfer terms. The remaining terms describe the loss of energy from the magnetosphere-ionosphere system through plasma injection, ionospheric losses and ring current energy losses.

In Spencer et al. [79],we showed that the most reliable Dst results were obtained when we use the solar wind rectified electric field (VB_s) or the coupling function derived by Newell et al. [24]. The input coupling function chosen for this study is the standard rectified vB_s formula [45], given by:

$$V_y = v_{sw} B_s^{IMF} L_y^{eff} (kV), \tag{4.11}$$

$$V_{sw}^{Bs} = 40(kV) + V_y, \tag{4.12}$$

where v_{sw} is the x-directed component of the solar wind velocity in GSM coordinates, B_s^{IMF} is the southward IMF component, and L_y^{eff} is an effective cross-tail width over which the dynamo voltage is produced. For northward or zero B_s^{IMF}, a base viscous voltage of 40 kV is used to drive the system.

In the differential equations the coefficients are physical parameters of the magnetosphere-ionosphere system. The quantities L, C, Σ, L_1, C_I, and Σ_I are the magnetospheric and ionospheric inductances, capacitances, and conductances, respectively. A_{eff} is an effective aperture for particle injection into the ring current. The resistances in the partial ring current and region-2 current, I_2 are R_{prc} and R_{A2}, respectively, and L_2 is the inductance of the region-2 current. The coefficient u_0 in eq. (4.5) is a heat flux limiting parameter. The energy confinement times for the central plasma sheet, parallel kinetic energy and ring current energy are τ_E, τ_k and τ_{rc}, respectively. The effective width of the magnetosphere is L_y and the transition region magnetic field is given by B_{tr}. The pressure gradient driven current is given by $I_{ps} = L_x(p/\mu_0)^{1/2}$, where L_x is the effective length of the magnetotail. The outputs of the model are the AL and Dst indices, in addition to all the magnetospheric field aligned currents. The contributions from the magnetopause and tail current systems

are given by:

$$Dst_{mp} = a * \sqrt{P_{dyn}}, \tag{4.13}$$

$$Dst_t = \alpha I(t), \tag{4.14}$$

where Dst_{mp} is the perturbation due to the magnetopause currents and Dst_t is the magnetic field contribution from the tail current $I(t)$ which is modeled by WINDMI as I. P_{dyn} is the dynamic pressure exerted by the solar wind on the earth's magnetopause. We used two values 15.5 and 7.26 for a as estimated by Burton et al. [13] and O'Brien and McPherron [15], respectively . Burton's formula estimates the contribution of Dst_{mp} to be more than twice that estimated by O'Brien's formula.

The factor α is an unknown geometrical factor that is also an optimization parameter. The optimized value of α is a first order approximation to the actual relationship between the geotail current and Dt. It is likely that the factor α is not constant but changes with external conditions (solar wind dynamic/thermal/magnetic pressure which shapes the tail lobe) and with the I(t) itself (location of the tail current sheet may correlate with the intensity of the tail current). Estimates for the value of α can be inferred from calculations similar to those given in the book edited by Kamide and Chian [1] (pp. 364-365). It has been estimated that, assuming the PRC and near-earth cross tail currents are confined within 18 to 06 local time sector in the nightside, at a distance of 6 R_E, each MA of the combined currents produce a disturbance of 10.4 nT on the earth's surface at low latitudes [1]. Since the effects of the individual currents are unclear, we leave a comparison of these different methods to find values or functional forms of α for future work.

The simulated Dst is given by:

$$Dst_{wmi} = Dst_{rc} + Dst_{mp} + Dst_t. \tag{4.15}$$

Using this expression to calculate the simulated Dst, we optimized the physical parameters of the WINDMI model and the geometrical factor α for all the events. Induced

currents flowing inside the earth's core enhance the measured magnetic field of each external current approximately by a factor C_{IC}, which is generally taken to be 1.3 [51, 90].

The Dst index is calculated after removing the baseline H and quiet time (Sq) from the H value measured at each station. The input to the WINDMI model includes a base viscous voltage in addition to the rectified solar wind Ey 4.12. This additional viscous voltage generates the quiet time values for the various magnetospheric currents (other than the magnetopause currents) for the WINDMI model. The Dt values obtained with this model include the quiet time values when IMF Bz was northward.

In order to compare these results directly with the Dt_{MT} values, the quiet time values were subtracted from the WINDMI Dt (Dt_{wmi}) values. In the rest of the paper, the contribution of the tail current as estimated from the WINDMI model and the MT index will be mentioned as Dt_{wmi} and Dt_{MT}, respectively. The base viscous voltage of 40 KV drives the WINDMI model, when IMF Bz is northward. This value also accounts for any viscous coupling during southward IMF Bz conditions. The results obtained are discussed in section 4.5.

4.4 Optimization of the WINDMI Model

The variable coefficients in the WINDMI model are L, M, C, Σ, Ω_{cps}, u_0, I_c, A_{eff}, B_{tr}, L_y, τ_E, $\tau_{||}$, L_I, C_I, Σ_I, L_2, R_{prc}, R_{A2}, τ_{rc}, and α. These parameters are constrained to a maximum and a minimum physically realizable and allowable values and combined to form a 18-dimensional search space $S \subset \mathbb{R}^{18}$ over which optimization is performed.

To optimize the WINDMI model, we use one form of the genetic algorithm [48] to search the physical parameter space in order to minimize the error between the model output and the measured geomagnetic indices. The optimization scheme was used to select a parameter set for which the outputs from the WINDMI model most closely matches the AL index and the Dst index simultaneously.

For this work we are primarily interested in the features of the Dst index, so we have chosen a higher bias of 0.5 for the Dst index. The contribution of the tail current is an important parameter in the modeling of the Dst index, while the fit against AL index

is important as the physical parameters in eqs. (4.3) - (4.9) are dependent on it. The weighting for the AL index and Dt values were set to 0.3 and 0.2, in order of relative importance. There is a strong direct correlation between solar wind parameters and the AL index during geomagnetic activity over hour time scales, and the Dst matches of the model are more believable if the additional data is represented well, too.

The performance of the algorithm is evaluated by how well the average relative variance (ARV) compares with the measured indices. The average relative variance gives a good measure of how well the optimized model tracks the geomagnetic activity in a normalized mean square sense. The ARV is given by:

$$ARV = \frac{\Sigma_i (x_i - y_i)^2}{\Sigma_i (\bar{y} - y_i)^2}, \tag{4.16}$$

where x_i are model values, y_i are the data values, and $\bar{y}$ is the mean of the data values. In order that the model output and the measured data are closely matched, ARV should be closer to zero. A model giving $ARV = 1$ is equivalent to using the average of the data for the prediction. If $ARV = 0$ then every $x_i = y_i$. ARV values for the AL index above 0.8 are considered poor for our purposes. ARV below 0.5 is considered very good, and between 0.5 to 0.7 it is evaluated based upon feature recovery. For the Dst index, an ARV of 0.25 is considered good.

The ARV values for all the three constraints are calculated over the period when the most geomagnetic activity occurs. When these criteria are observed to be acceptable, the optimization process is assumed to have reached convergence.

In previous works, the WINDMI model has been used to model isolated substorms [64, 65], and classify them in some cases as being driven by a northward turning of the IMF Bz [91]. During storm time, periodic substorms have been analyzed by Spenecr and co-workers [30, 92]. In the first part of the results section below we have turned off the substorm effect in the WINDMI model by setting the critical geotail current parameter Ic at a level such as to preclude a substorm trigger. The nature of this trigger and the effect of including substorms on the modeled Dt values will be detailed later in section 4.5.

4.5 Results and Discussion

A set of 13 events were selected by Patra et al. [58] where the IMF Bz turned northward abruptly after the peak in Dst index was observed. Under these conditions it is assumed that the flow out losses will be less dominant and the recovery would be governed by the contributions from the tail current and ring current.

Later in Spencer et al., we chose six events out of the initial 13 events [79]. In addition to the 6 out of 13 events, we also selected the October 2000 and April 2002 storm events used previously in Spencer et al. [92]. For this work, we have analyzed the same six events chosen from the previous group of 13. These are 1) Days 158-166, 2000, 2) Days 258-266, 2000, 3) Days 225-235, 2001, 4) Days 325-335, 2001, 5) Days 80-88, 2002, and 6) Days 245-260, 2002. In addition, we also analyzed the April 2002 storm. However, in what follows we will discuss four out of the seven events. This is in order to determine the relative contribution of the geotail current to the observed Dst index.

The MT index for the seven storms analyzed were obtained from particle precipitation data from low-altitude polar orbiting NOAA/POES 15, 16, 17, and 18 satellites. The isotropic boundary (IB) was identified from the particle precipitation measurements. The MT index was derived after removing the MLT dependence of the IB latitude derived [69]. These seven storms were found to fall into two categories [79]. In the first category (Category I) were storm events where the coupling functions look qualitatively slightly different from each other, but using any solar wind magnetosphere coupling function resulted in a good fit to the measured Dst data. In these events, the relative contributions from each current system due to the different inputs remained roughly the same through the optimization process. These storm events were characterized also by their classical nature in that the onset, main phase and decay phase are distinct. In another category (Category II), the storms are much more dependent on the input coupling function used. For coupling functions that are significantly different from each other, the output Dst curves were different, and each Dst curve predicted a different level of geomagnetic activity over 6-8 hour time scales. Here we have chosen to just use the standard rectified solar wind input for our

analysis.

Figure 4.1 shows the comparison of Kyoto Dst and the Dst generated by the WINDMI model for the storm on days 261-267 in the year 2000. This storm fell into Category II from our previous work. The optimized result shown was obtained after using Dt_{MT} as an additional matching criteria. The solar wind velocity v_x, IMF B_z, and the proton density N_p, are shown in the top three panels. Contributions from the magnetopause current, the ring current and the tail current are shown in the fourth panel of fig. 4.1. In fig. 4.2 the modeled westward Auroral Electrojet (AL) index and the magnetotail contribution Dt are shown. The top panel compares the hourly averaged Kyoto AL index with the AL calculated by the WINDMI model from the region 1 current. The bottom panel of fig. 4.2 plots the Dt_{wmi} and Dt_{MT} values.

The degree of correspondence between the modeled and measured Dst, AL, and Dt values is very similar for the four other storms (days 159-167 in 2000, days 229-236 in 2001, days 326-336 in 2001, and days 247-261 in 2002) as for the storm shown in figs. 4.1 and 4.2. The fact that the dynamics of the tail current contribution are similar in the two very different modeling approaches (MT and WINDMI based) corroborates that the tail current and its dynamics can be robustly monitored by the MT index and that the WINDMI model is able to represent the overall variation in the tail current as well. However, it seems that the good agreement between Dt_{MT} and Dt_{wmi} is sometimes broken during storm time substorms. We will next discuss two such events.

The first is the storm on days 81-89, 2002, which was categorized as a Category-II storm [58, 79]. The Dst, AL, and Dt fits for this storm are shown in figs. 4.3 and 4.4. The Dt matches are good in the initial phase of the storms as well as during the entire recovery period. However, during the main phase on days 83 and 84 (fig. 4.4), a sequence of sawtooth events were found to occur [93]. During this time, soon after the substorm onset in the beginning of day 83, the Dt_{wmi} significantly overestimates the tail current intensity being about 2 times larger than Dt_{MT}.

Another event for which the Dt fits obtained by the model were not corresponding

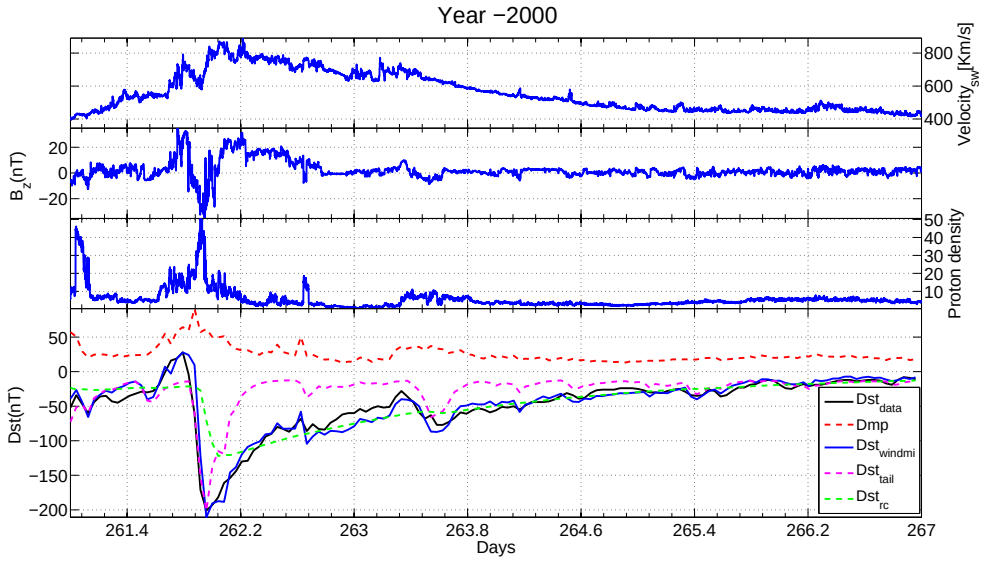

Fig. 4.1: The top three rows of the figure show the solar wind velocity, B_z, and proton density respectively, during the storm starting on day 261, 2000. The fourth row shows the best fit obtained by the WINDMI model. The contributions from other magnetospheric currents are also shown.

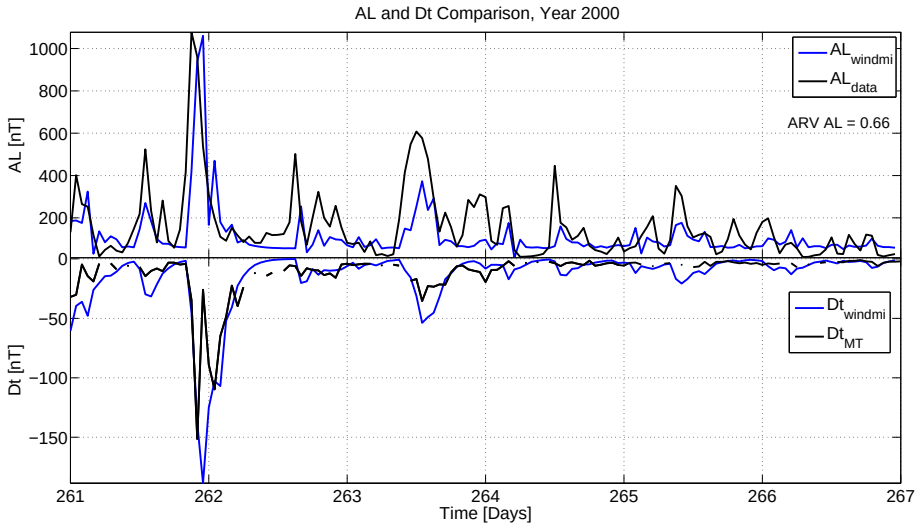

Fig. 4.2: The top panel shows the comparison of the AL index and the modeled values. The bottom panel of this figure shows the comparison between the Dt_{MT} values derived from the MT index and the Dt_{wmi} for the storm starting on day 261, 2000.

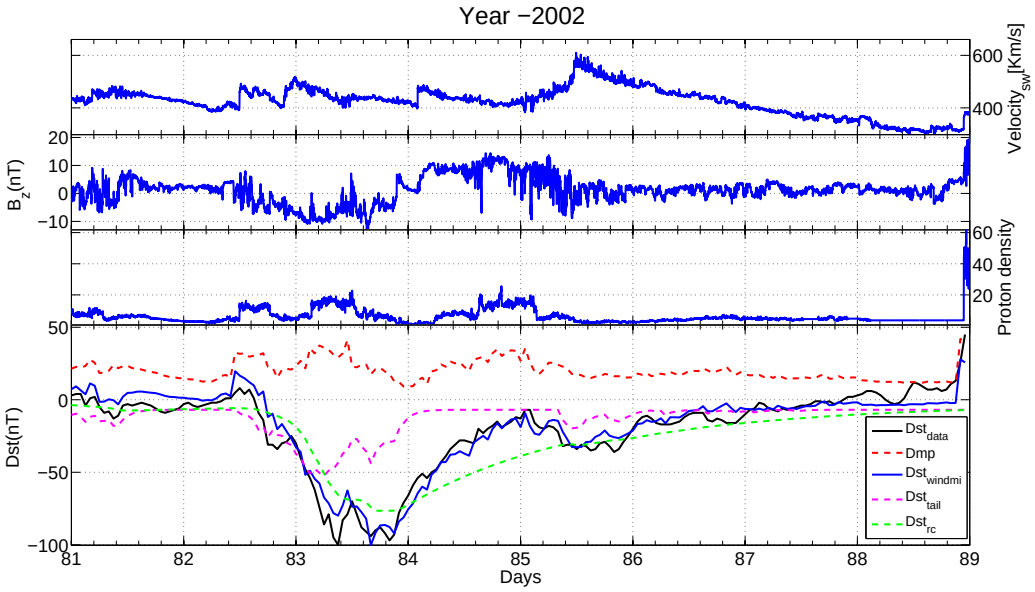

Fig. 4.3: The top three rows of the figure show the solar wind velocity, B_z, and proton density respectively, during the storm starting on day 81, 2002. The fourth row shows the best fit obtained by the WINDMI model. The contributions from other magnetospheric currents are also shown.

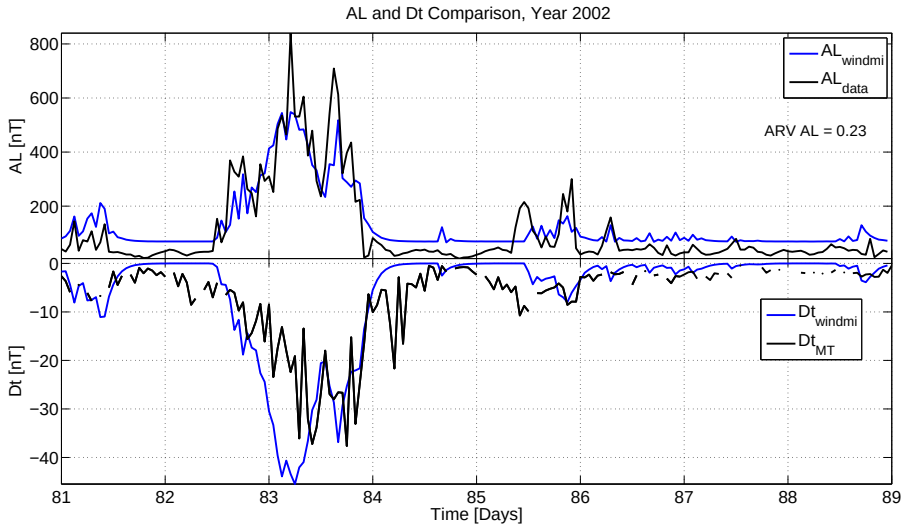

Fig. 4.4: The top panel shows the comparison of the AL index and the modeled values. The bottom panel of this figure shows the comparison between the Dt_{MT} values derived from the MT index and the Dt_{wmi} for the storm starting on day 81, 2002.

well with the Dt_{MT} values was during the sequence of sawtooth events between days 108 and 109, 2002 (figs. 4.5 and 4.6). Here, again the Dt matches are good everywhere, except during the time when periodic substorms occur (fig. 4.6). From fig. 4.6 we observe that during days 108-109, even though the Dt_{MT} values are smaller, the corresponding values of the Kyoto AL are elevated which corresponds to substorms.

Note that the WINDMI model has the capability to produce substorm phenomena through the $\Theta(u)$ switching function in eq. (4.5), which switches a pressure relieving energy unloading component when the geotail current reaches a certain critical value. However, for this part of the work we have turned the switch off. The reason for this is that in order to correctly optimize the model to capture substorm activity, we will have to perform optimizations over intervals in the order of hours, and not over a storm period of many days. We do not expect the substorm switch to be accurate over long periods of time, since the state of the magnetosphere may change considerably over a day. For predicting and analyzing the Dst index over a multiple day period the model has been found to be more consistent and reliable when the substorm effect is excluded. In the following section, we will discuss some results from the WINDMI model with the substorms turned on to illustrate the difference in model behaviour.

During substorms, the particle distribution may become more isotropic due to increased precipitation. However, it is expected that the region of precipitation penetrates closer to earth (to lower latitudes) which would lead to the IB (MT index), being closer to the earth than it should be [23]. This would lead to larger values of Dt_{MT}. The observations are to the contrary. The Dt_{MT} values during substorms are smaller in magnitude than the Dt_{wmi} values. When the substorm mechanism in WINDMI is turned off, Dt_{wmi} overestimates the Dt because the model will not unload magnetic and plasma thermal energy into the ionosphere through the field aligned currents or the earthward parallel flow of plasma.

The MT index is mostly defined at any time by only a couple of (sometimes even just one) point observation within the hour. This may lead to the fact that small scale local disturbances in the IB are misinterpreted as global changes in the Dt. In Asikainen et

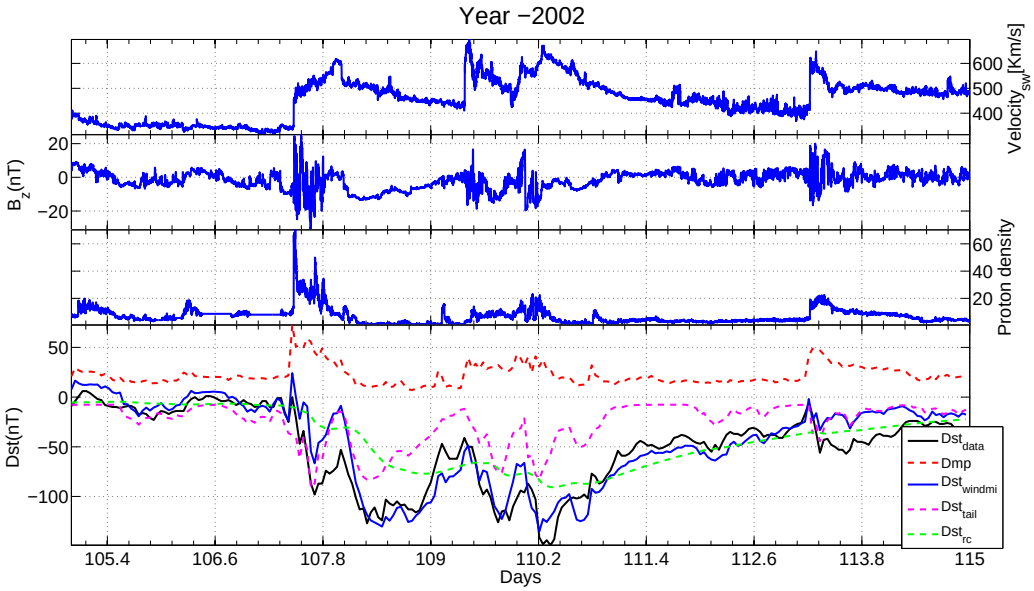

Fig. 4.5: The top three rows of the figure show the solar wind velocity, B_z, and proton density respectively, during the storm starting on day 105, 2002. The fourth row shows the best fit obtained by the WINDMI model. The contributions from other magnetospheric currents are also shown.

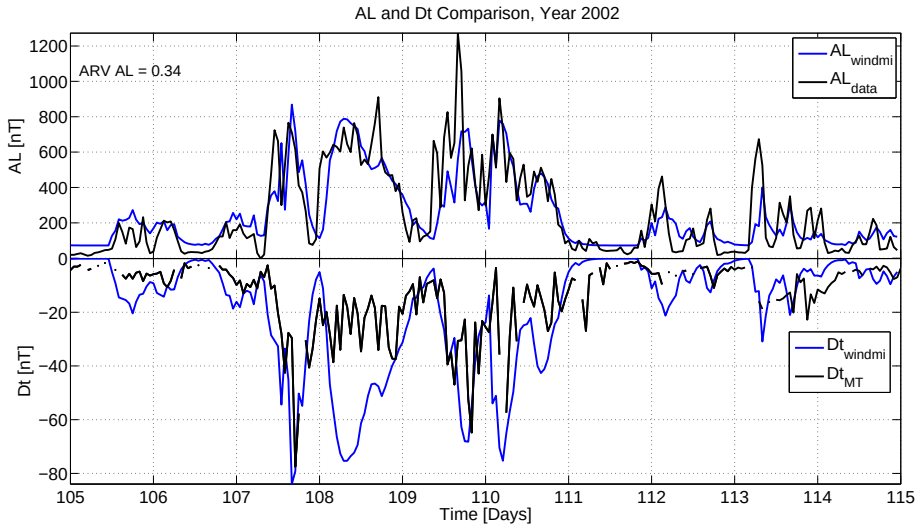

Fig. 4.6: The top panel shows the comparison of the AL index and the modeled values. The bottom panel of this figure shows the comparison between the Dt_{MT} values derived from the MT index and the Dt_{wmi} for the storm starting on day 105, 2002.

al. to avoid this effect, a 3-hour running mean of the MT time series was taken, before determining the Dt_{MT} values [69]. This would decrease the small scale local variations in the tail current/IB and emphasize the smoother time evolution of the global tail current.

In this work we have used the unsmoothed MT index. This was done in order to retain some of the information that can be obtained with the higher resolution data. The MT index values show more variation in the hourly time scale, in the tail current, some of which may be due to local effects. However, the differences in the Dts during the storms are rather large and long lived which suggests that the main differences are probably not due to local effects but due to the substorm effects.

Substorm Effects

In order to account for the difference between Dt_{wmi} and Dt_{MT} during the periods where substorm activity was reported, we repeated the optimizion procedure for the storms on days 81-89, 2002 and 105-114, 2002 with the substorm trigger allowed to activate. All other parameters were allowed the same flexibility as before, but the critical geotail current Ic was allowed to take low enough values so that a substorm could be triggered. Ic appears in the $\Theta(u)$ switching function in eq. (4.5), which is given by:

$$\Theta(u) = \frac{1}{2}\left[1 + tanh\left(\frac{I - I_c}{\Delta I}\right)\right]. \tag{4.17}$$

The values of I_c and the interval ΔI in eq. (4.17) represent the rate at which a transition to loss of plasma along newly opened magnetic field lines occurs. The function $\Theta(u)$ changes from zero to unity as a function of the geotail current I compared to I_c. The unloading function follows from current gradient driven tearing modes or cross-field current instabilities, see for example the paper by Yoon et al. [94].

In the WINDMI model, ring current energization is produced by two mechanisms (eq. (4.10)), the flow of plasma thermal energy from the near earth plasma sheet, and the current I_2 (region 2 current), that leaves the ionosphere on the dawnside, closes in the ring current and returns to the ionosphere on the duskside. This secondary loop of current has a self

inductance L_2 and drives a current through the partial ring current resistance R_{prc} as well as the resistance of the region 2 current loop footprint R_{A2}. The Joule heating through the resistance R_{prc} energizes the ring current particles. A_{eff} is an effective aperture for particle injection into the ring current, that on the duskside merges with what is known as the Alfven layer [42]. The Alfven layer is defined to be the separatrix between two sets of drift trajectories, one comprising open drift paths extending from the magnetospheric tail to the dayside magnetopause and another, nearer set consisting of closed drift paths, encircling the earth [95].

The model was optimized over the main phase for the two storms, which were chosen to be from days 82.5-85, 2002, and 108-110, 2002. $SymH$ and minute resolution AL were used in addition to Dt_{MT} as the constraining parameters. The resulting Dt plots are shown in figs. 4.7 and 4.8. These results should be compared with the plots shown in figs. 4.4 and 4.6.

The results indicate that during the main phase of the storms the disruption of the tail current leads to reduction in the strength of the crosstail current. This reduction is reflected well in the Dt_{MT} values. The decrease in the Dt intensity is compensated by energization of the ring current particles due to increased particle injection during a substorm. The effect of substorms on Dst index has been reported earlier as small decreases in its magnitude [96]. The sudden enhancement in the nightside ion fluxes is a consequence of particle energization during substorm expansion. The energy (or momentum) of a particle gyrating along a stretched field line will increase when the field line relaxes to more dipole-like, in order to conserve the first and second adiabatic invariants [97].

But the enhanced inductive electric field during a substorm alone is not completely effective in energizing the ring current. Sanchez et al. propose that dipolarization and accompanying current disruption cause ions within the reconfiguration region to be prevented from further earthward penetration, thus creating a temporary void of plasma sheet particles in the inner edge of the plasma sheet [84]. This could lead to lower enhancement of the ring current particles during a substorm.

In our simulations, the optimization procedure makes the energy input due to $I_2^2 R_{prc}$ into the ring current during substorms become dominant. The pVA_{eff} energy input becomes small because the thermal pressure decreases substantially in the plasma sheet when a substorm is triggered (eq. (4.10)). Whether this is accurate can only be determined by means of another measurement constraint imposed on the model. We will address this issue in future modeling work.

4.6 Conclusion

In this work we have used the MT-index, which is an indicator of the ion-isotropic boundary location, to constrain the WINDMI model geotail current. The best fit WINDMI values were compared with the magnetic disturbance estimated on the surface of the earth due to the strength of the tail current. The magnetotail current contribution to the Dst index as calculated by the WINDMI model has a very good correlation with the values calculated from the empirical expression relating the MT index to the ground perturbation due to geotail current.

The addition of this additional constraint on the WINDMI model makes the calculated magnetospheric currents more reliable. We observed that for most storms, the relative contribution from the geotail current and ring current to the Dst index obtained from our earlier studies are consistent with the present work. The most significant difference was observed for the storms where periodic substorms were observed during the storm. During such storms the MT index and the resulting Dt values show a significant drop in magnitude that is attributed to the current disruption during a substorm, leading to lower strength of the geotail current.

The WINDMI model is able to confirm this observation when the substorms are triggered in the model. The corresponding drop in contribution to the $Dst/SymH$ indices is compensated by the enhancement in the energization of the ring current due to the increased inductive E-field during a substorm dipolarization. The observed $SymH$ correlates favorably with these substorm dynamics. This work suggests that the contribution from tail current to ground perturbation is important.

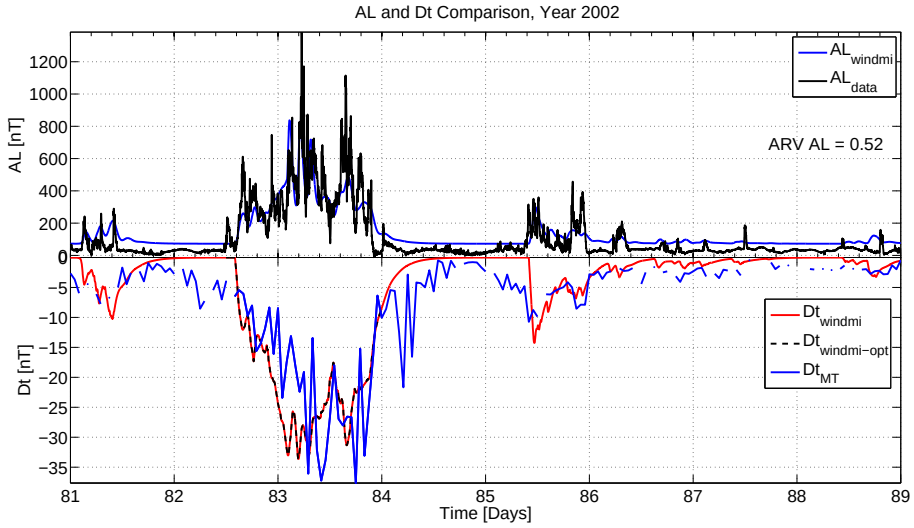

Fig. 4.7: The best fits of AL and Dts for the storm on days 81-89,2002. The AL is estimated every minute. Optimization was performed over days 82.5-84.

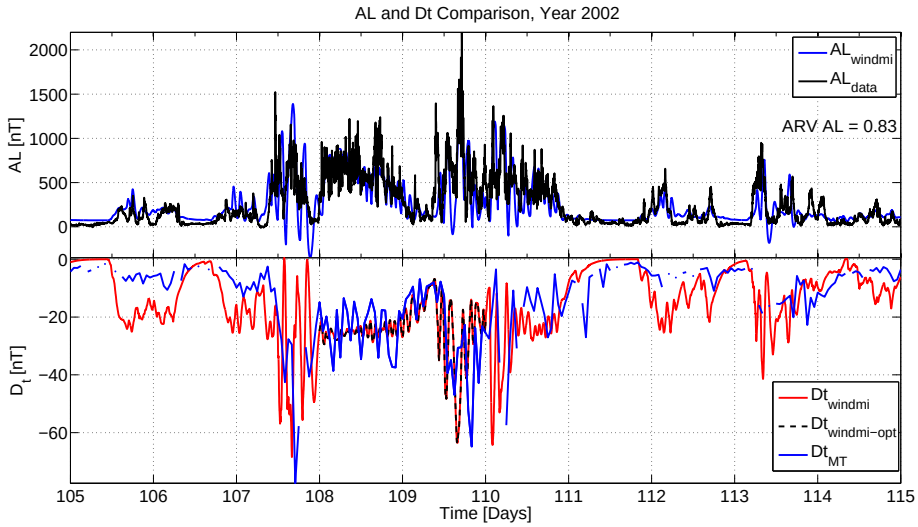

Fig. 4.8: The best fits of AL and Dts for the storm on days 105-115,2002. The AL is estimated every minute. Optimization was performed over days 108-110.

More work needs to be done to confirm the exact mechanism for the energization of the ring current during a substorm. The conditions that trigger a substorm in the magnetosphere is still an open question and further studies are required. The combination of the right trigger condition as well as the correct energization mechanism for the ring current will enable the WINDMI model to reproduce the Dst index more realistically.

Chapter 5

The Effect of Nonlinear Ionospheric Conductivity Enhancement on Magnetospheric Substorms

5.1 Introduction

The substorm is a fundamental geomagnetic process in the earth's magnetosphere that has been a topic of intense research over several decades. Of particular interest is how the ionosphere, inner magnetosphere, and geotail dynamics influence the growth, onset, expansion, and recovery phases of a typical substorm. These components may interact differently under varying solar wind conditions, or different classes of substorm activity. Currently there are three accepted classes of substorms: isolated substorms, storm time substorms, and sawteeth events also known as periodic substorms [98].

In this work, we modify the equations of a low order physics based nonlinear model of the magnetosphere called WINDMI [30, 64], in order to account for the contribution of ionospheric conductivity enhancement to substorm behaviour. The current version of the model is available at the NASA Community Coordinated Modeling Center for near real time forecasts of space weather activity [99].

The standard explanation for ground based observations of substorm development is through a nonlinear energy loading and unloading process [100]. The growth phase occurs when the IMF turns southward for a period of time, plasma sheet thinning develops, then reconnection occurs, followed by dipolarization. This growth phase is not always observable because of the fluctuations in the IMF. The precise mechanisms for substorm onset is still under investigation [101], but reconnection in the tail is understood to be the point when the dipolarization occurs, which marks the expansion phase of a substorm. Finally, as the plasma energy is lost, the substorm goes into its recovery phase. We note that a strongly

fluctuating solar wind may trigger bursts in the AE index [102], but this effect is not represented in the nonlinear dynamical WINDMI model.

The modeling of nonlinear loading and unloading behaviour of geomagnetic substorms under southward IMF conditions has been explored by several authors [103–105]. Vassiliadis et al. used a nonlinear filter approach for describing the solar wind magnetosphere coupling [106], and further to predict the AL index [107]. Weigel et al. used a neural network approach to predicting AL index activity [108]. The WINDMI model was used by Horton et al. [91] to classify substorms into three categories, one of which is the northward turning triggered substorm [109]. Here we continue to develop the WINDMI model as a tool for analyzing and forecasting the loading-unloading type of substorm.

A detailed photochemical equilibrium model of the quiet time ionosphere that depended on the solar zenith angle and F10.7 flux was developed by Rasmussen et al. [110]. An ionospheric conductance model based on ground magnetic disturbance data was developed by Ahn et al. [111]. The dependence of ionospheric conductivity on energy deposited by precipitating electrons was modeled by Robinson et al. [112]. It is known that the ionospheric conductivity is enhanced during the growth and expansion periods of a substorm, when increased particle precipitation occurs in the high latitude ionosphere parallel to the magnetic field lines, reported by Tang et al. [113] and references therein. Aksnes et al. [114] derive conductance maps showing the increase in Hall and Pederson conductivities during an isolated substorm using data from the Polar Ionospheric X-ray Imager (PIXIE) and the Ultraviolet Imager (UVI) on board the Polar satellite. Gjerloev and Hoffman calculated the height integrated Hall and Pederson conductances during substorms using the Dynamics Explorer 2 data [115]. In our model we introduce the effect of conductivity enhancement by including a nonlinear conductivity term controlled by the parallel streaming kinetic energy of the plasma along magnetic field lines that terminate on the ionosphere. This term adds a new component to the dynamics of substorms, which we explore.

Our aim in this paper is to determine how the enhanced ionospheric conductivity plays a role in the buildup and recovery of a substorm. For instance, if the conductivity rises slowly

during the growth phase, and then is suddenly enhanced in a sharp manner at substorm onset, the resulting increase in the auroral electrojet current appears more sawtooth like, as opposed to the case of the electrojet signature due to a reconnection trigger only. The faster the rate of enhanced conductivity, the more sawtooth like the response becomes. We also evaluate the model results for two isolated substorm events: one on July 31 1997, and another on April 13 2000. These two substorms are examples of well-documented events, where the onset, expansion, and recovery phases are clear while ionospheric conductance enhancement is clearly present [114], and the onset of the expansion phase of the substorm is timed accurately [116]. These two substorms also have two common features in that the solar wind driver sharply decreases in the early part of the recovery phase, and that neither of them are triggered by northward turning of the IMF Bz. The model behavior with enhanced conductivity is compared to the case where the ionosphere conductivity is constant.

In the next section we describe the WINDMI model. In section 5.3, we introduce a nonlinear conductance term into the model. In section 5.4, we show how the increased conductivity affects the phases of a synthetic isolated substorm. In section 5.5, we compare the model to data for the two substorm events. We then summarize the paper and conclude with some suggestions for future work.

5.2 WINDMI Model

The plasma physics based WINDMI model uses the solar wind dynamo voltage V_{sw} generated by a particular solar wind-magnetosphere coupling function to drive eight ordinary differential equations describing the transfer of power between the major energy components of the nightside magnetosphere. The WINDMI model is described in some

detail in earlier works [30, 42, 58]. The equations of the model are given by:

$$
\begin{aligned}
L\frac{dI}{dt} &= V_{\rm sw}(t) - V + M\frac{dI_1}{dt}, && (5.1)\\
C\frac{dV}{dt} &= I - I_1 - I_{\rm ps} - \Sigma V, && (5.2)\\
\frac{3}{2}\frac{dp}{dt} &= \frac{\Sigma V^2}{\Omega_{\rm cps}} - u_0 p K_{\parallel}^{1/2}\Theta(u_1) - \frac{pVA_{\rm eff}}{\Omega_{\rm cps}B_{\rm tr}L_y} - \frac{3p}{2\tau_E}, && (5.3)\\
\frac{dK_{\parallel}}{dt} &= I_{ps}V - \frac{K_{\parallel}}{\tau_{\parallel}}, && (5.4)\\
L_I\frac{dI_1}{dt} &= V - V_I + M\frac{dI}{dt}, && (5.5)\\
C_I\frac{dV_I}{dt} &= I_1 - I_2 - \Sigma_I V_I, && (5.6)\\
L_2\frac{dI_2}{dt} &= V_I - (R_{\rm prc} + R_{A2})I_2, && (5.7)\\
\frac{dW_{\rm rc}}{dt} &= R_{\rm prc}I_2^2 + \frac{pVA_{\rm eff}}{B_{\rm tr}L_y} - \frac{W_{\rm rc}}{\tau_{\rm rc}}. && (5.8)
\end{aligned}
$$

The nonlinear equations of the model trace the flow of electromagnetic and plasma mechanical energy through eight pairs of transfer terms. The remaining terms describe the loss of energy from the magnetosphere-ionosphere system through plasma injection, ionospheric losses and ring current energy losses.

In the differential equations, the coefficients are physical parameters of the magnetosphere ionosphere system. The quantities L, C, Σ, L_I, C_I, and Σ_I are the magnetospheric and ionospheric inductances, capacitances, and conductances, respectively. A_{eff} is an effective aperture for particle injection into the ring current, that on the dusk side merges with what is known as the Alfven layer [42]. The resistances in the partial ring current and region-2 current, I_2 are R_{prc} and R_{A2}, respectively, and L_2 is the inductance of the region-2 current. The coefficient u_0 in eq. (5.3) is a heat flux limiting parameter. The energy confinement times for the central plasma sheet, parallel kinetic energy and ring current energy are τ_E, τ_k, and τ_{rc}, respectively. The effective width of the magnetosphere is L_y and the transition region magnetic field is given by B_{tr}. The pressure gradient driven current is given by $I_{ps} = L_x(p/\mu_0)^{1/2}$, where L_x is the effective length of the magnetotail. The output of the model are the AL and Dst indices, in addition to the magnetospheric field aligned

currents.

The pressure unloading function $\Theta(u_1) = \frac{1}{2}[1 + \tanh u_1]$ where $u_1 = (I - I_c)/\Delta I$ in eq. (5.3) is specified by a critical current I_c and the interval ΔI for the transition to loss of plasma along newly opened magnetic field lines with a parallel thermal flux $q_{||}$. It changes from zero to unity as a function of I compared to I_c. The unloading function follows from current gradient driven tearing modes or cross-field current instabilities [94].

The AL index is obtained from the region 1 current I_1 index by assuming a constant of proportionality $\lambda_{AL}[A/nT]$, giving $\Delta B_{AL} = -I_1/\lambda_{AL}$. The input function used for the model is the standard rectified vB_s formula [45], given by:

$$V_{sw}^{Bs} = 40(kV) + v_{sw} B_s^{IMF} L_y^{eff}(kV), \tag{5.9}$$

where v_{sw} is the x-directed component of the solar wind velocity in GSM coordinates, B_s^{IMF} is the southward IMF component, and L_y^{eff} is an effective cross-tail width over which the dynamo voltage is produced. For northward or zero B_s^{IMF}, a base viscous voltage of 4 kV is used to drive the system.

5.3 Enhanced Nonlinear Conductivity During Substorm Growth and Onset

The ionosphere electron density is the auroral zone is strongly affected by particle precipitation along magnetic field lines. Impact ionization increases with the number and energy of particles entering the ionosphere down to 100 - 120 km, where the auroral electrojet currents flow. The magnetic field lines begin in the magnetotail plasma sheet and close in the ionosphere above 65 degrees latitude. The conductivity is composed of the Hall and Pederson components, given by Coumans et al. [117],

$$\sigma_P = \frac{N_e e}{B}\left(\frac{\nu_{en}\omega_{ce}}{\nu_{en}^2 + \omega_{ce}^2} + \frac{\nu_{in}\omega_{ci}}{\nu_{in}^2 + \omega_{ci}^2}\right), \tag{5.10}$$

$$\sigma_H = \frac{N_e e}{B}\left(\frac{\omega_{ce}^2}{\nu_{en}^2 + \omega_{ce}^2} - \frac{\omega_{ci}^2}{\nu_{in}^2 + \omega_{ci}^2}\right), \tag{5.11}$$

where N_e is the electron density, e the electron charge, ν_{en} and ν_{in} are the electron neutral

and ion neutral collision frequencies, ω_{ce} and ω_{ci} are the electron and ion gyrofrequencies respectively in the geomagnetic field B.

The Pederson component is the conductivity parallel to the electric field and perpendicular to the magnetic field. The Hall component is the conductivity perpendicular to both the electric and magnetic fields. The conductivity is a strong function of N_e. Ionization is expected to ramp up due to increased precipitation, and saturates as the ionization rate is balanced by recombination and losses. In addition, the conductivity increases or decreases according to the electron neutral collision frequency.

When the plasma sheet electric field is enhanced during the substorm growth phase, The crosstail electric field drives field aligned currents from the plasma sheet into the ionosphere. As the upward field aligned currents in the midnight-premidnight sector intensifies, parallel electric potentials form above the auroral ionosphere that accelerate charged particles into the ionosphere [118, 119]. There is a sudden increase in the parallel electric fields around substorm onset [120], which should increase the rate of particle precipitation. Gjerloev and Hoffman [121] and Aksnes et al. [114] report an increase in the Hall and Pederson conductivities in the ionosphere at auroral latitudes during substorm activity . The strength of the westward auroral electrojet will consequently be increased since it is controlled by the Hall conductivity [122].

To include the effect of a nonlinear ionospheric conductance that is enhanced through increased particle precipitation during the substorm growth and expansion phases, eq. (5.6) is modified with a nonlinear function controlled by the parallel kinetic energy along field lines $K_{\parallel}$. The equation then takes the form:

$$C_I \frac{dV_I}{dt} = I_1 - I_2 - (\Sigma_I + \Sigma_{enh}\Theta(u_2))\, V_I. \tag{5.12}$$

The function $\Theta(u_2)$ is in the same form as the function in eq. (5.3) except that in this case, $u_2 = (K_{\parallel} - K_{\parallel}^0)/\Delta K$ where $K_{\parallel}^0$ is a lower limit for the parallel kinetic energy above which the conductivity becomes enhanced at the altitude of the auroral electrojet. We expect that below this value of $K_{\parallel}$ the precipitating particles do not penetrate to the

lowest altitudes. The parameter ΔK controls the rate of conductivity enhancement up to a saturation level of $\Sigma_I + \Sigma_{enh}$. Physically this parameter is governed by the ionization efficiency at a particular altitude.

5.4 Implications on Substorm Dynamics

If the ionospheric conductivity is assumed to be constant during the growth, expansion and recovery phases of a substorm, the westward auroral electrojet current signature is driven only by solar wind magnetosphere coupling, and magnetospheric dynamics. This is illustrated with the black curve in fig. 5.1 where we run the model with a southward IMF of 20 nT, and solar wind velocity of 600 km/s, for 20 minutes. We see the increase in the current during the growth phase of the substorm when the geotail magnetic field stretches, the substorm onset, followed by the expansion phase, and finally the recovery phase. The sudden surge in auroral electrojet current is caused by the unloading trigger $\Theta(u_1)$ being switched on corresponding to reconnection in the geomagnetic tail.

In the same figure, we also show how the input into the model creates an increase in the auroral electrojet current depending on the rate of ionosphere conductivity enhancement, shown as a red curve. In this case, the reconnection switch is turned off, the surge is entirely controlled by the enhanced conductivity. We have slightly exaggerated the enhanced conductivity following Tang et al. [113], the enhancement is sharply increased when the precipitation rate crosses a threshold level, which likely occurs sometime during the later part of the growth phase of a substorm. This corresponds to the idea that above a certain level of activity, the precipitating particles penetrate deeply enough into the ionosphere to reach the altitudes where the auroral electrojet flows. This type of enhancement causes a surge and recovery of the electrojet similar to the charge-discharge process of a linear RL circuit.

Lastly, we now include both the reconnection trigger as well the conductivity enhancement. This is shown with the blue curve in fig. 5.1. Now the overall substorm event is characterized by both the effects simultaneously affecting the expansion and recovery phases. Of particular note is that in the later part of the recovery, the electrojet settles

smoothly to rest without the negative overshoot. We also note that the overall level of electrojet activity increases when the conductivity is enhanced.

To examine the behaviour of the model for changes in the value of $K_{\parallel}^{0}$ and Σ_{enh}, we chose upper and lower values of each parameter around the nominal values whose results were shown in fig. 5.1. We do this for the case when both the reconnection switch and conductivity enhancement are present. In the nominal case, which corresponds to the blue curve in fig. 5.1, we have $K_{\parallel}^{0} = Kc = 6 \times 10^{13}$ Joules, $\Sigma_{enh} = 10$ Siemens, and $\Delta_K = 1.5 \times 10^{13}$ Joules. With changes in parameter values above and below these nominal values, the character of the output auroral electrojet current is altered as shown in fig. 5.2. The input is kept the same as that in fig. 5.1.

The behavior is as expected. In the top panel of fig. 5.2, we see that as the threshold level for beginning the enhancement is lowered, the field aligned currents increase faster during the growth period of a substorm, and decays more slowly during the recovery phase. In the second panel of fig. 5.2, it is clear that if the upper saturation level of the ionospheric conductivity is increase, we obtain much stronger current values. Finally, in the bottom panel of fig. 5.2, the effect of the Δ_K can be observed to change the rate of increase of the conductivity around the threshold level $K_{\parallel}^{0}$, resulting in a change of the rate of increase and decrease of the electrojet strength.

5.5 Results for Jul. 31, 1997 and Apr. 13, 2000 Substorms

We first use the new model to analyze an isolated substorm that occurred between 03:00 and 04:00 UT on Apr. 13, 2000. The growth phase of this substorm is not clear from the data. The onset of the substorm was between 03:05-03:10 UT on the day [116]. With the solar wind parameters obtained from the ACE spacecraft translated to the nose of the magnetosphere [30], the resultant input rectified voltage is shown in the bottom panel of fig. 5.3.

In order to obtain our results, we adjust our model in order to to fulfill two criteria. The first is that the onset time must be almost at the onset time reported by Huang et al. [116]. The second is that we try to capture the overall substorm growth, expansion

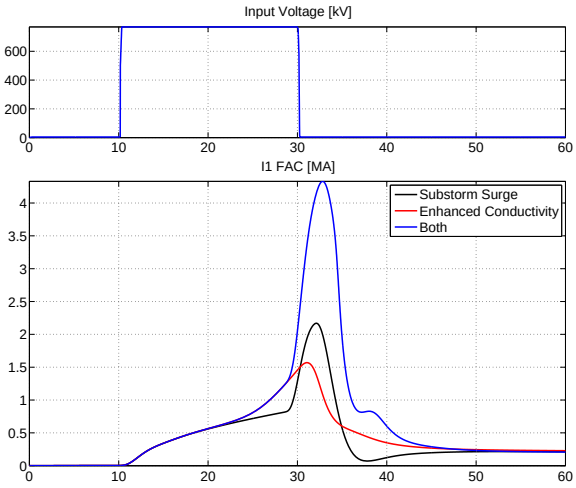

Fig. 5.1: The response of the magnetosphere-ionosphere field aligned current system simulated by the WINDMI model for the case with a reconnection switch (shown in black), or the enhanced conductivity (shown in red), or both (shown in blue).

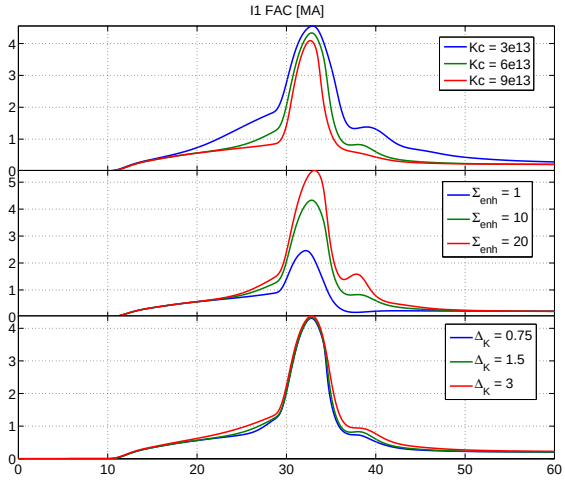

Fig. 5.2: The response of the WINDMI model when the values of $K_{\|}^{0} = Kc$, Σ_{enh} and Δ_K is varied referred to the nominal plot shown by the blue curve in fig. 5.1. The threshold parallel kinetic energy above which the conductivity becomes strongly enhanced is varied from $3 - 9 \times 10^{13}$ Joules, the saturation level of the conductivity is varied from $1 - 20$ Siemens, and the rate of increase in the conductivity is varied from $0.75 - 3 \times 10^{13}$ Joules.

and recovery phases. A particularly important reason why this substorm was chosen is because the input voltage decreases sharply at approximately 03:30 UT, which means that the observed recovery phase is not affected by solar wind driving. In addition, the IMF Bz remains southward during the onset, ensuring that this substorm is not a case that is possibly driven by northward turning of the IMF.

In the first case, the model parameters are adjusted to perform as well as possible on the substorm, but without the conductivity enhancement. The result is shown by the red curve in fig. 5.3. In the plot, the AL index refers to the lower auroral electrojet index obtained from the world data center for geomagnetism, Kyoto, Japan. This data represents the deflection of the earth's magnetic field at auroral latitudes from 12 stations (http://wdc.kugi.kyoto-u.ac.jp/). The time scale is in minutes starting from 00:00 hours UT. The model run shows the growth phase, onset at roughly the same time as observed, a fast expansion followed by recovery after 03:20 UT. The recovery rate is fast in the model, faster than the activity shown in the data.

In the second case, we show how the model result changes when the enhancement in the ionospheric conductivity is included. This is shown by the green curve in fig. 5.3. For this run, the model parameters are adjusted differently in order to capture the substorm activity. In this case, the expansion phase begins at the same time as when the enhanced conductivity is not used, but the peak activity occurs a little later (03:28 UT) and the recovery phase is much slower. Here the recovery appears to follow the recovery phase in the data more closely, except during the time period 03:20 UT to 03:40 UT, where a decline in AL followed by a small surge occurs in the data. We note that the second surge in AL that occurs around 03:38-03:40 UT does not appear to be driven by the solar wind.

Overall, the model captures the substorm activity, but the interpretation of the results depend on whether enhanced conductivity is assumed to play a role, or not. A quantitative measure that we use to determine the goodness of fit between the model output and the data is the Average Relative Variance (ARV). For the Apr. 13, 2000 substorm, the ARV when only a reconnection trigger is used is 0.71. When the conductivity enhancement is

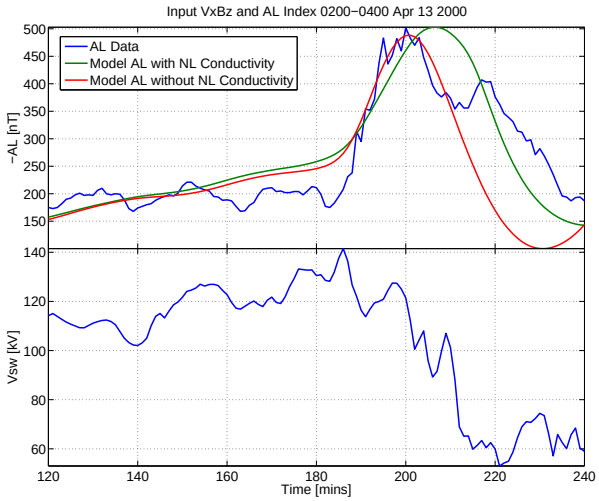

Fig. 5.3: April 13 2000 substorm analysis with the WINDMI model. The result when using only a reconnection trigger (ARV = 0.71) is compared to the result when conductivity enhancement (ARV = 0.32) is also included.

also included, the ARV is 0.32. Using this measure, the lower the ARV the better the performance, which suggests that that the enhanced conductivity improves the result.

Another substorm that has similar features to the April 13 2000 event is an earlier event that occurred on Jul. 31, 1997. The onset for this substorm was timed at 02:40 UT on the day [114]. In this case, we used OMNI data for the solar wind input parameters, obtained from the WIND satellite. The input rectified voltage is shown in the bottom panel of fig. 5.4. For this substorm, conductance maps were generated in Aksnes et al. [114] that clearly show the enhancement of conductivity between 21:00 MLT and 00:03 MLT as the substorm develops. In particular, the Hall conductance showed a strong increase.

As before, we adjust our model in order to to fulfill two criteria. The first is that the onset time must be almost at the onset time reported. The second is that we try to capture the overall substorm growth, expansion and recovery phases. As in the previous case, the input voltage decreases sharply at approximately 03:05 UT, which means that the observed recovery phase is not affected by solar wind driving. The IMF Bz remains southward during the onset, ensuring again that this substorm is not a case that is possibly

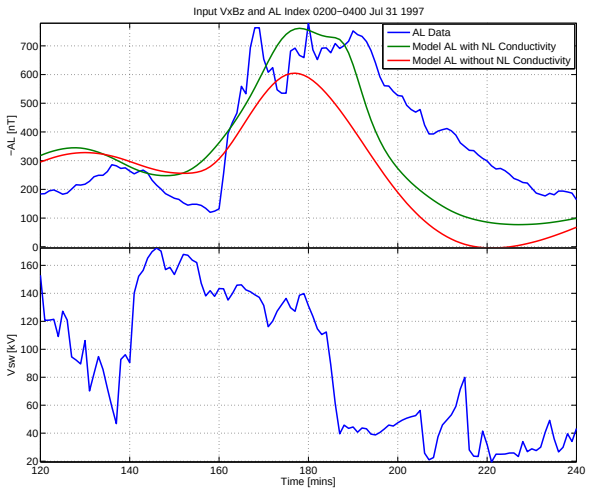

Fig. 5.4: July 31 1997 substorm analysis with the WINDMI model. The result when using only a reconnection trigger (ARV = 1.06) is compared to the result when conductivity enhancement (ARV = 0.55) is also included.

driven by northward turning of the IMF.

Because the conductivity was in fact enhanced according to the reported values in Aksnes et al. [114], we increased the saturation level of the conductivity to $\Sigma_{enh} = 50$ and obtained a result that gave an ARV of 0.55 compared to the case when only the reconnection trigger is present, which gave an ARV of 1.06. The improvement is not significant from a qualitative point of view, but we can see in fig. 5.4 that the green curve, representing the model output with enhanced conductivity, somewhat follows the almost square like features of the AL peak. Increasing the conductivity level further did not improve the calculated ARV.

5.6 Conclusions

In this paper, we modified our nonlinear model of the magnetosphere to account for the enhanced ionospheric conductivity during substorm growth, onset, and expansion. This is incorporated into the model by introducing a term in the equation driving the auroral electrojet that depends on the rate of particle flow along the magnetic field lines that begin in the plasma sheet and close in the higher latitude ionosphere.

We explored the most significant implications of the new term on the dynamics of the model. In addition, we used two substorm datasets, chosen because they were not triggered by northward turning of the IMF Bz, and that the solar wind driver turns off during the recovery phase.

We found that the dynamics of the auroral electrojet is modified, depending on the level of enhancement, the energy content of the parallel flow of particles, and the ionization efficiency, which are controllable parameters in the model. The effect is most pronounced if the conductivity enhancement is sudden. For a gradual build up and decay of conductivity, the electrojet current decays more slowly during the substorm recovery period, and does not overshoot negatively at the end of the substorm.

In future work, we will use the new model to analyze a larger dataset of geomagnetic substorms, such as that provided by the SUPERMAG database (http:supermag.jhuapl.edu/).

Chapter 6

Effects of Changing Solar Wind Conditions on Open Drift Paths

6.1 Introduction

Growth of partial ring current and the formation of the closed ring current are one of the most important features of a geomagnetic storm. The intensity of a storm is measured by the *Dst* index. It has been observed that the *Dst* index generally has a two phase decay as the magnetosphere recovers from a storm. This physics behind this phenomenon has been explained by proposing that the fast initial decay is caused by the initial fast flow out loss of energetic ring current ions through the magnetopause [32, 50]. This is followed by slower charge exchange mechanisms in the later recovery phase. The initial fast flow out loss is assumed to be controlled by the rate of cessation of solar wind driving.

The initial decay rate of storms with abrupt cessation of solar wind driving with other storms with gradual recovery was compared by O'Brien et al. [49]. They used 29 storms in the period Nov. 1963 - Sept. 2001. Their findings suggested that the storms with abrupt northward turning of the IMF Bz show the same recovery in the first six hours or slightly more recovery than do the storms with gradual northward turnings. In another work, Patra et al. [58] studied 13 storms in the period 2001 -2007, with abrupt northward turning of the IMF Bz after the peak in *Dst* index. They too concluded that two phase decay was still evident in those storms even though the solar wind driving was turned off.

Both these works agree on the fact that the rate of recovery is not affected significantly by the northward turning (i.e., shutoff of convection), but suggest different physical mechanisms at work. O'Brien et al. [49] suggest that the flow-out provides an additional loss mechanism, being equal to or greater than charge-exchange loss during slow-shutoff-storm

recovery causing the Dst index to have similar recovery times. In Patra et al.'s work, it was reported that modeling the Dst index by including contributions from other magnetospheric currents, most noticeably the tail current provided a high degree of fidelity in estimating Dst [58]. The plasma sheet density too has an important role to play in the ring current build up and decay as shown by Liemohn and Kozyra [35].

Kozyra and co-workers have successfully modeled many storms with northward turning of the IMF B field using empirical and numerical models [10, 14]. The energy transfer from the solar wind and the resulting convection electric field plays an important role in the fast flow out losses of ring current ions in these kind of models. This field is closely related to the interplanetary E-field [123]. The various solar wind magnetospheric coupling functions represent this relationship. A clear consensus does not yet exist as to which function describes the convections electric field the best. This leads to some difficulty in interpreting model results related to flow out losses.

In this work, we compare simulation results against magnetometer data for certain storms with abrupt northward turning of the IMF Bz (hence, possibly leading to cessation of solar wind driving). The selected storms have been classified as Category I storms in Patra et al. [58]. Category-I storms have been classified on the basis of their similar performance under different solar wind coupling functions. Magnetometer data from various low latitude stations are presented in a unique way first proposed by Love and Gannon to compare against ring current simulations [124]. In the next section we explain the models available at CCMC, which have been used for this analysis. Next, in section 6.3, we explain the procedure used to generate the movie maps from the magnetometer data. A comparison of the results of the simulation with the magnetic data is done section 6.4.

6.2 Models at CCMC

The Community Coordinated Modeling Center (CCMC) Runs-on-Request System (RoR System) is used to obtain output from the BATS-R-US global MHD model run along with the Rice Convection model (RCM) [125] and the Fok Ring Current model of the inner magnetosphere model [62, 63].

The BATS-R-US code solves the governing equations of magnetohydrodynamics [126]. All terms describing deviations from ideal MHD are included through appropriate source terms. The governing equations for an ideal, non-relativistic, compressible plasma may be written in a number of different forms. In primitive variables, the governing equations, which represent a combination of the Euler equations of gas dynamics and the Maxwell equations of electromagnetics, may be written as:

$$\frac{\partial \rho}{\partial t} + \mathbf{u}.\nabla\rho + \rho\nabla.\mathbf{u} = 0, \tag{6.1}$$

$$\rho\frac{\partial \mathbf{u}}{\partial t} + \rho\mathbf{u}.\nabla\mathbf{u} + \nabla p - \mathbf{j}\times\mathbf{B} = 0, \tag{6.2}$$

$$\frac{\partial \mathbf{B}}{\partial t} + \nabla\times\mathbf{E} = 0, \tag{6.3}$$

$$\frac{\partial \rho}{\partial t} + \mathbf{u}.\nabla p + \gamma p\nabla.\mathbf{u} = 0, \tag{6.4}$$

where the current density j and the electric field vector E are related to the magnetic field B by Amperes law and Ohms law, respectively:

$$\mathbf{j} = \frac{1}{\mu_0}\nabla\times\mathbf{B}, \tag{6.5}$$

$$\mathbf{E} = -\mathbf{u}\times\mathbf{B}. \tag{6.6}$$

The Comprehensive Ring Current Model (CRCM) couples the Rice Convection Model (RCM) and the kinetic model of Fok et al. [63]. The calculations are performed in two steps. First, the evolution of distribution function at each point is calculated which is due to drift and losses (FokRC model). Then, the field-aligned currents in the ionosphere and ionospheric potential are calculated using RCM scheme (for the details, see Fok et al. [63]). Field-aligned currents are calculated from a current continuity equation between the magnetosphere and ionosphere [62]:

$$J_{||i} = \frac{1}{r_i cos^2\lambda}\sum_i\left(\frac{\partial\eta_j}{\partial\lambda}\frac{\partial W_j}{\partial\phi} - \frac{\partial\eta_j}{\partial\phi}\frac{\partial W_j}{\partial\lambda}\right), \tag{6.7}$$

where the summation is done at fixed λ, ϕ point and over all M, K points, $J_{||i}$ is a sum of

ionospheric field- aligned current densities for both hemispheres, W_j is the kinetic energy of a particle with given λ, ϕ, M, K and η_j is the number of particles per unit magnetic flux (density invariant in terms of RCM) associated with $\Delta M, \Delta K$:

$$\eta_j = 4\sqrt{2}\pi m_0^{3/2}\overline{f}_s(\lambda, \phi, M, K,)M^{1/2}\Delta M\Delta K. \tag{6.8}$$

Using the distribution of field-aligned currents, the ionospheric potential is obtained from eq. (6.8). We assume here that B_i is the same for both hemispheres. By definition, $J_{||i}$ here describes only region 2 field aligned currents.

6.3 Moviemaps

The *Dst* index is used as an indicator of the ring current energization. It is calculated from a weighted average of disturbance data from a sparse longitudinal distribution of four low-latitude magnetic observatories. However, *Dst* does not measure the local time shape of low-latitude magnetic disturbances. The present availability of an extensive network of high quality magnetometer stations provides us the opportunity to study the local time distribution of magnetic disturbances. Love and Gannon were the first to use unique maps of the local time functional dependence of storm time disturbance [124]. They were the first ones to plot the magnetic disturbance data in a geometry that resembled the physical structure of the ring current. These "movie maps" permit detailed inspection of the data, their variation in time, and their variance in space.

Another popular scheme to analyze magnetometer data is to create panoramic views by making contour plots of magnetic disturbance across a domain of local time and universal time (LT-UT) [127–129]. We use maps similar to the movie maps in addition to the LT-UT plots to compare the FRC results with the ground magnetic disturbances. We use a technique similar to the that used for the generation of Kyoto *Dst* index to calculate the magnetic disturbances. We find the two quietest days in a month and take the average to create the quiet time B-field ($StatQ_{avg}$). This is subtracted from the magnetic field

measured at each magnetometer station ($Stat_H$) as shown in eq. (6.9).

$$Dist_H = \frac{Stat_H - StatQ_{avg}}{cos(\phi)} \tag{6.9}$$

The latitudinal correction is accounted by dividing the cosine of the each station's magnetic latitude value (ϕ). $Dist_H(\theta_m)$ is a smooth curve generated by interpolating each magnetic station data using a Fourier series fit to the data as shown in eq. (6.10). The various model parameters (Dst_O, a_i^c, a_i^s) are obtained with a least squares algorithm. The movie maps are plotted in a polar co-ordinate system similar to the ones used by Love and Gannon [124].

$$Dist_H(\theta_m) = Dst_O + \sum_{i=1}^{3} a_i^c cos\left(\frac{2\pi i\theta_m}{1440}\right) + \sum_{i=1}^{3} a_i^s sin\left(\frac{2\pi i\theta_m}{1440}\right), \tag{6.10}$$

where Dst_O is a representive Dst generated from all the low-latitude stations under consideration.

The decomposition in terms of Fourier terms is motivated by a need for a complete basis set that is periodic in local time. The reason for only choosing Fourier expansion up to degree 3 is guided by the need to satisfy the spatial Nyquist criteria [128]. It was found by Clauer and McPherron that the distribution of magnetic observatories around the world at that time was inadequate to define coefficients beyond the third harmonic, which corresponds to sine waves of eight-hour period in local time and by the Nyquist criteria requires a separation of at most four hours [128]. The number of magnetic stations used by us are similar to the ones used by earlier scientists [124, 128], hence using higher order harmonics in the Fourier fit will lead to suspect model values.

The polar plots used in movie maps aid in better visual understanding of the ring current system under observation. Each instantaneous disturbance value $Dist_H$ from each observatory is plotted radially, where the zero value is on a black circle centered at the origin. This permits unambiguous plotting of disturbance data that are positive (inside the

zero-value circle) and negative (outside the circle). The azimuthal angle used for plotting each $Dist_H$ value is the local magnetic time for the observatory.

Selected movie maps will be made freely available on the web. In the next section, we will compare the FRC results and the movie maps for a few storms.

6.4 Simulation Results and Moviemaps

In Spencer et al. [79] storms with abrupt turning of IMF Bz have been classified into Category I and II, depending on the similarity or dissimilarity of their coupling functions and resultant analysis by the WINDMI model. Category-I storms have similar solar wind coupling function values leading to similar Dst estimation by the WINDMI model irrespective of the input coupling function used. These storms are ideal in analyzing the magnetospheric response when solar wind energy input in the recovery phase of a geomagnetic storm is minimal.

Figure 6.1 shows the solar wind conditions and the $SymH, ASymH$, and AL magnetic indices. We choose eight instances in time to illustrate a few unique observations made for this particular storm. The first instance is at 10:00 hrs on day 17 representing the quiet time features before the start of the storm. Three other instances are chosen in the initial phase of the storm showing some symmetric and asymmetric features during this phase. Two instances each in the main phase and recovery phase are chosen to show the how the asymmetric response in the main phase changes to symmetric during the later part of the recovery phase. These eight instances are shown by the dashed vertical red lines in fig. 6.1.

A popular way of representing the temporal and spatial (azimuthal) variations of the disturbance H is to display them in a two-dimensional LT-UT diagram. The usefulness of the LT-UT map consists of the identification of its features (the spatial location of the field disturbance) with specific current systems [130]. The LT-UT plot for the chosen storm is plotted in fig. 6.2 (bottom). It shows the azimuthal (LT) variation of the midlatitude geomagnetic disturbances observed at the magnetometer stations. For reference, we also plot the $SymH$ index at the top of this figure.

The observed diagonal trend in the data having 45 degrees of gradient is the effect of

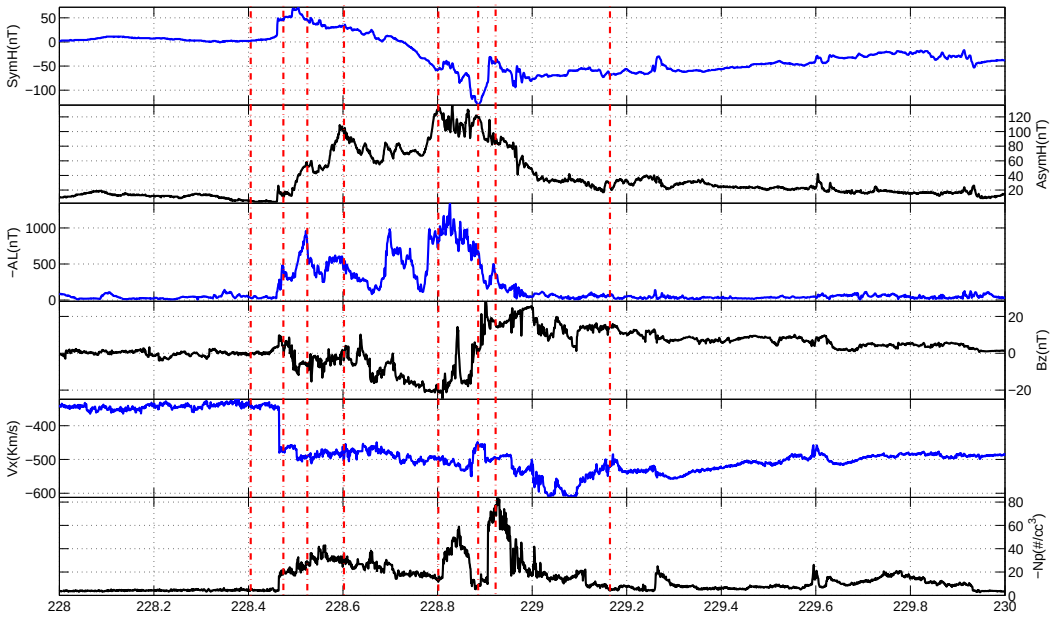

Fig. 6.1: The magnetic indices and the solar wind conditions during the Category I storm starting on Aug. 17, 2001. The dashed vertical lines correspond to the eight instances of time discussed in the text.

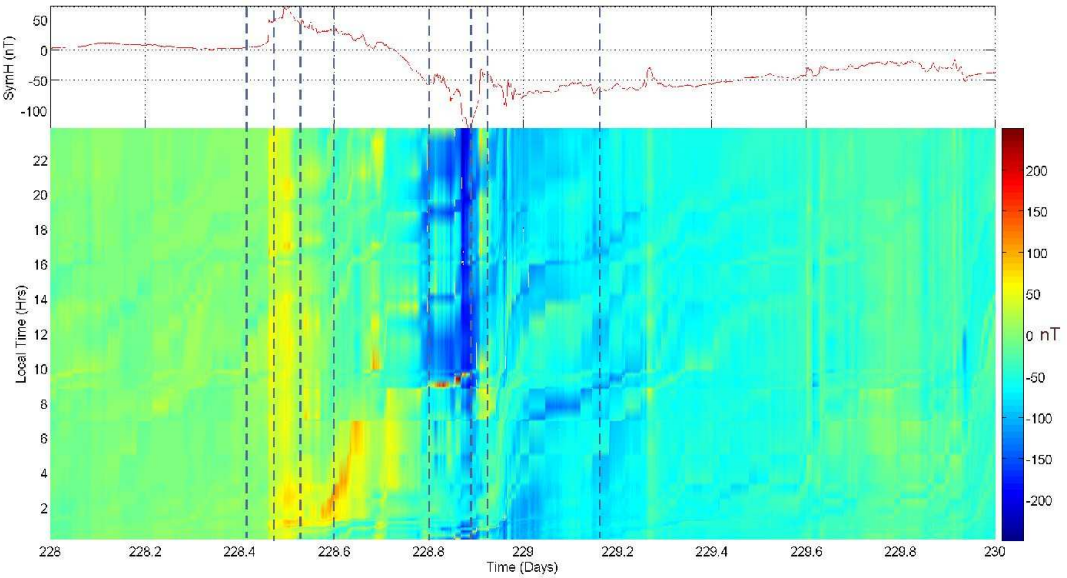

Fig. 6.2: Bottom. UT-LT map showing the azimuthal (LT) variation of the midlatitude geomagnetic disturbance on Aug. 17, 2001. Top. The *SymH* index is for the storm duration plotted. The dashed vertical lines correspond to the eight instances in time chosen for this study.

the earth's rotation which matches the station motion across the map. Clauer et al. [131] investigated this observation and suspected that it results because peaks in the disturbance profile are observed by stations in a specific region, but they rotate with time carrying the peak in the profile with them. A solution to eliminate this effect was also proposed by them where a reference time was selected and subtracted from the data values at the reference time from all later values for each station. We have, however, not used this method in producing fig. 6.2.

Before the start of the storm just before 12:00 UT, Aug. 17, 2001, the magnetometer stations are symmetric and show almost negligible disturbance referenced by the first vertical line in fig 6.2. The start of the storm is signaled by the arrival of a solar wind pressure pulse triggering the SSC. This disturbance is shown by the second vertical dashed line in and it can be seen that the positive disturbance due to the compression of the magnetosphere is observed at all local times. The next two vertical lines signify the start of the magnetospheric convection while the effect of magnetospheric compression is still active.

The signature of convection is localized first in the night side and gradually its magnetic signature spreads to cover the entire earth (vertical lines 5 and 6). The next instance in time chosen during the early recovery phase (vertical line 7) shows the response of the magnetometer station to a pressure pulse during the recovery phase. This can also be seen as a sudden recovery in the $SymH$ index. The strong, dynamic azimuthal variations of the midlatitude disturbance provide qualitatively different information from the placid, simpler view of the storm afforded by $SymH$ or even the $ASymH$ index. The LT-UT plots provide a different perspective as compared to the $SymH$ index and when analyzed with the movie maps, a lot of new information can be obtained.

We ran the BATSR-US model along with RCM and FRC at CCMC for the Category - I geomagnetic storm starting on Aug 17, 2001. The ring current particle flux results of the simulation are plotted in a unique way by overlaying the corresponding movie maps over them as shown in figs. 6.3-6.6. Each of the figs. 6.3-6.6 have four rows each. The first row in each figure plots the $SymH$ for the entire storm. Also, plotted in the first row is the

total proton energy calculated by the FRC. The ring current energy W_{rc} can be related to the $Dst/SymH$ index using the Dessler-Parker-Schopke (DPS) relation [46, 47]:

$$Dst = \frac{\mu_0 W_{rc}(t)}{2\pi B_E R_E^3}, \tag{6.11}$$

where W_{rc} is the plasma energy stored in the ring current and B_E is the earth's surface magnetic field along the equator. The second and third rows plot the $ASymH$ and AL indices for the storm, respectively. The fourth row compares the FRC simulation results with the magnetic data from the movie maps. In each of the figures, two instances in time are compared in the fourth row. Each image from the FRC plots the calculated flux of protons in the inner magnetosphere. The plots are color coded in a 2-D surface plot. The movie map plots the magnetospheric disturbances in a polar coordinate. A central black circle designates the zero disturbance reference. Magnetospheric data from each station is plotted as red dots and a smooth fit according to eq. (6.10), is plotted to represent the local time variation of the disturbance. The spatial scales of the disturbance calculated by FRC are accurate while the movie map data is just illustrative.

The left panel in the fourth row of fig. 6.3 shows the response of the FRC, as well as the moviemap, before the storm has started (quiet time response). It can be clearly seen that the FRC flux of protons is symmetric. The magnetic disturbances too are symmetric and hardly show any deviation from the zero disturbance circle.

6.4.1 Initial Phase

Figure 6.3 plots the response of the FRC and movie map before the storm has started and just after the sudden storm commencement (SSC). The right panel in the fourth row of the figure shows the results at time 11:20 UT on Aug. 17, 2001. The $SymH$ data in the first row shows a positive disturbance. Corresponding disturbances are also seen in the AL and $ASymH$ indices. The moviemap result shows almost symmetric positive disturbance across all the magnetic stations. This is consistent with the theory of Chapman and Ferraro [132], the movie-map for this storm makes it clear that the onset of the initial

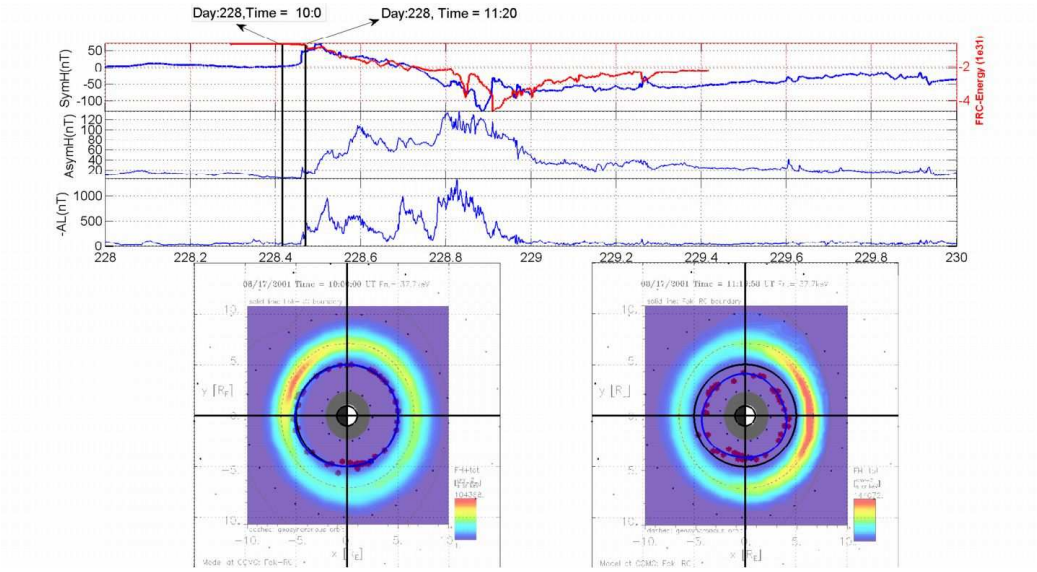

Fig. 6.3: Comparison of Fok Ring current simulation results for the Category I storm starting on Aug 17, 2001 with magnetospheric indices and movie maps. The first row plots the $SymH$ and the FRC proton energy. The second and third rows show the AL and $ASymH$ values for the storm. Comparison of the FRC ion flux and the movie maps is shown in the fourth row at 10:00, and 11:20 UT.

phase is caused by an enhancement of solar wind pressure. This pushes the magnetopause in toward the earth and intensifies the eastward electric currents of the magnetopause. By Ampres law, the magnetopause currents generate a northward magnetic disturbance, and since the dimension of the magnetopause is much larger than the diameter of the earth, positive magnetic disturbance is seen more or less uniformly at all local times; the curve fitted to the disturbance data is relatively symmetrical [124]. The FRC response shows an increase in the particle flux on the dayside in response to this pressure pulse.

Figure 6.4 illustrates the additional information that is obtained from the use of movie maps. The asymmetries observed during the initial phase of this storm are clearly visible in the fourth panel of this figure. The panel on the left in the fourth row plots data-simulation results at time 12:40 UT. Compared to the right panel in the fourth row of fig. 6.3, the disturbance of this initial phase becomes more asymmetrical. This is possibly in response to mild magnetospheric convection commencing with intermittent Bz south and connection of the interplanetary magnetic field onto the geomagnetic field. The IMF and solar wind

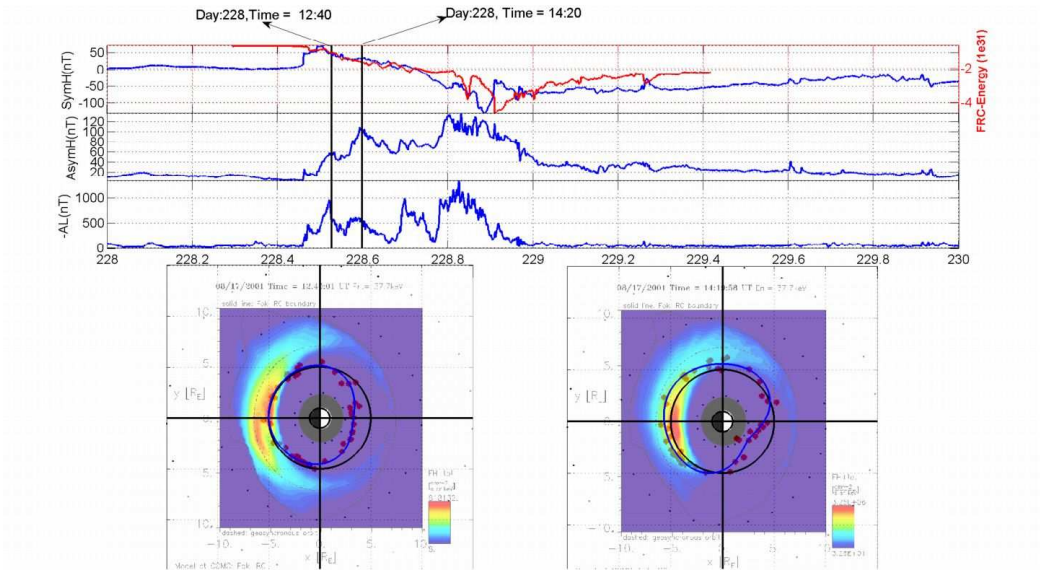

Fig. 6.4: Comparison of Fok Ring current simulation results for the Category I storm starting on Aug 17, 2001 with magnetospheric indices and movie maps. The first row plots the $SymH$ and the FRC proton energy. The second and third rows show the AL and $ASymH$ values for the storm. Comparison of the FRC ion flux and the movie maps is shown in the fourth row at 12:40, and 14:20 UT.

parameters can be found in fig. 6.1. Thus the obvious energization of the ring current prior to the start of the main phase of the storm can be observed through the movie maps.

The second instance, plotted in fig. 6.4, is at 14:20 UT. At this time the maximum asymmetry in the latitudinal magnetic disturbance during the initial phase of the storm was observed, as shown in the $ASymH$ index. The asymmetry is created by both positive and negative disturbances. It can be hypothesized that these represent a superposition of disturbance sustained by magnetopause currents, supported by solar wind pressure, and partial ring currents (and, even, field-aligned currents) [124, 133].

6.4.2 Main Phase

The dawn dusk asymmetry observed in magnetic station data has been historically interpreted as due to the strong presence of the partial ring current. The cause of the asymmetry is a combination of forces due to magnetic field gradients and convective electric fields. This results in a concentration (reduction) of ion drift lines of trajectory in the dusk

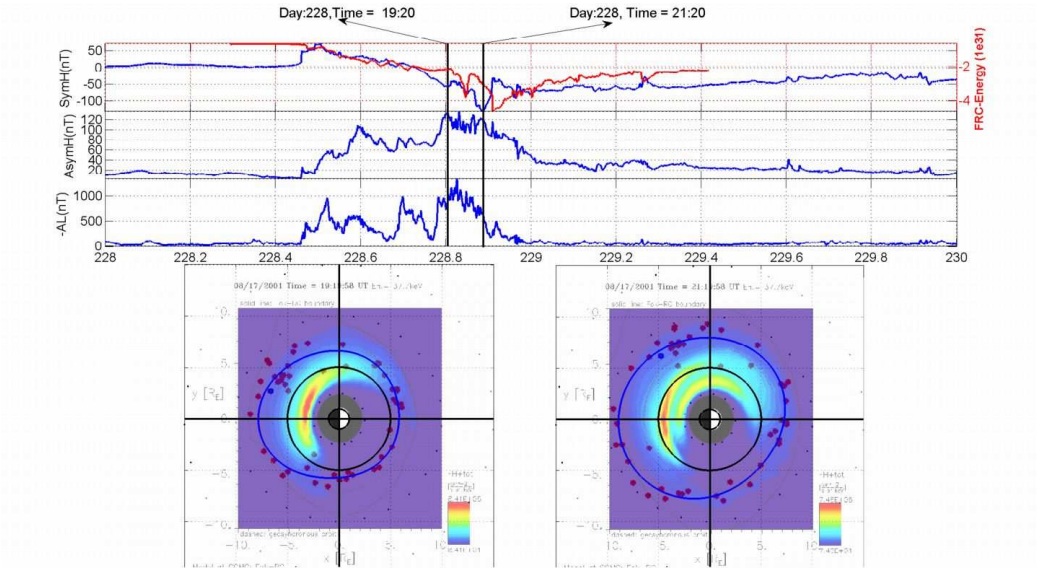

Fig. 6.5: Comparison of Fok Ring current simulation results for the Category I storm starting on Aug 17, 2001 with magnetospheric indices and movie maps. The first row plots the $SymH$ and the FRC proton energy. The second and third rows show the AL and $ASymH$ values for the storm. Comparison of the FRC ion flux and the movie maps is shown in the fourth row at 19:20, and 21:20 UT.

(dawn) magnetosphere (e.g., Takahashi et al. and Liemohn et al. [32, 50]), or equivalently, a dusk-centered partial ring current. Figure 6.5 shows results at time 19:20 and 21:20 UT. These times correspond to the peak asymmetry and the peak intensity observed during the main phase of the storm. It can be seen from the movie map as well as FRC data that the flux and the associated disturbance is large during this time. The solar wind and IMF conditions indicate that conditions favorable for strong convection were present.

At the end of the main phase, approximately around 21:20 UT, the IMF Bz turns northward almost abruptly and the recovery of the storm is triggered. It is expected that the flow out losses which were dominant during the main phase will be become less important in the recovery phase.

6.4.3 Recovery Phase

This storm starting on Aug. 17, 2001 was initially chosen for study by Patra et al. [58] since a sudden northward turning of the IMF Bz was observed after the peak in Dst index

was reached. It was hypothesized that this sudden northward turning of the IMF Bz will lead to trapped particle in the earth's ring current and the flow out losses which were one of the dominant modes of ring current particle loss during the main phase will be less important. The FRC simulation results seem to agree with this assumption as can been seen in fig. 6.6. The FRC simulation results at the instances of time show that the peak of intensity has clearly shifted from the nightside to the dayside (compare left panel and right panel in the fourth row). This can be possibly be explained as a result of drift of trapped particles on closed drift paths in the absence of convection from the nightside in response to the northward turning of IMF Bz.

At 22:00 UT a sudden drop in the value of $Sym - H$ was observed. A simultaneous sudden increase in solar wind dynamic pressure was also observed, as can be seen in fig. 6.1. The corresponding movie map plot shows an interesting almost triangular disturbance. This could possibly be a response to the sudden compression of the dayside magnetosphere in response to the pressure pulse. The effects of the already increased asymmetric ring and possibly tail current were superposed with this increase in the magnetopause current.

In the late recovery phase, at 04:20 UT on Aug. 18, 2001 an enhanced symmetric ring current is observed in the FRC simulation results. The movie map too shows a symmetric but negative disturbance across the magnetometer data. In this phase the particles are already trapped on the closed drift paths while losing energy due to charge exchange with neutral atoms.

During this storm, the IMF Bz turns northward at around 228.9 right after the peak in $SymH$ was obtained. In Patra et al. [58] it was found that various different solar wind magnetosphere coupling functions produced similar low energy transfer values in the recovery phase when the IMF Bz is northward. We can obtain the total energy gain and loss for the ring current particles from the FRC model. In fig. 6.7 we have plotted the total energy gain as well as the absolute energy gain of the ring current particles. The top two rows show the $SymH$ and Bz values. The eight instances of time chosen earlier are shown by vertical dashed lines. It can be clearly seen that the charge exchange losses are much smaller as

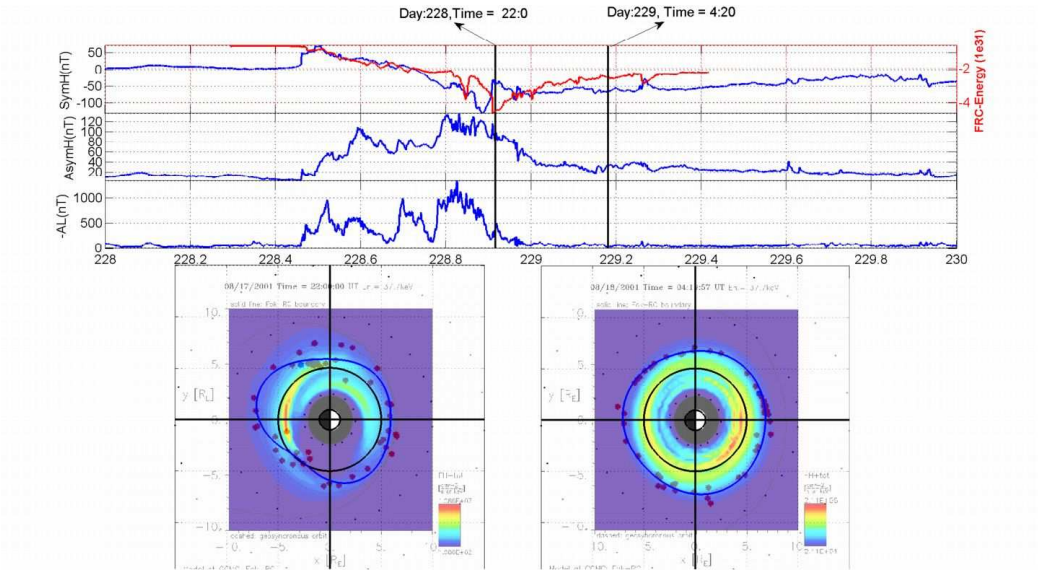

Fig. 6.6: Comparison of Fok Ring current simulation results for the Category I storm starting on Aug. 17, 2001 with magnetospheric indices and movie maps. The first row plots the $SymH$ and the FRC proton energy. The second and third rows show the AL and $ASymH$ values for the storm. Comparison of the FRC ion flux and the movie maps is shown in the fourth row at 22:00 UT on day 228 and 04:20 UT on Aug. 18, 2001.

compared to the losses due to flow out of particles from the magnetosphere in the main and early recovery phase. The ratio of the flow out to charge exchange exceeds 1 only in the late recovery phase. Although the flowout losses do not abruptly stop after the northward turning of the IMF Bz, but the flow out losses reduce sharply after the northward turning. For this storm, the flow out losses reduce drastically within two hours, so for this storm it can be safely assumed that the early recovery has a smaller contribution from the flowout loss.

Mitchell et al. have used ENA images of the earth's inner magnetosphere to compare the ring current morphology during the Bastille day event and a moderate event on June 10, 2000 for which the IMF B_z gradually turned northward [39]. The IMF Bz turns northward soon after the peak in $SymH$ for the Bastille day event. They confirmed that the contribution to the ring current in the small, June 10 storm and associated substorms was much further away from earth, and much more dependent on open drift path dynamics, than in the larger Bastille storm where the ions contributing to Dst drifted primarily on

Fig. 6.7: The bottom row shows the absolute energy gain of the ring current particles as simulated by the FRC model for the storm. The third row shows the total energy gain. $SymH$ and IMF Bz are shown in the top two rows. The dashed vertical lines correspond to the eight instances of time discussed in the text.

closed paths. Particles trapped in the ring current once the magnetospheric convection weakens drift around earth and lose energy through the charge exchange process. This was seen in the ENA images for the Bastille day storm [39]. In fig. 6.8, we plot the ring current particle flux data from the FRC simulation for 22.4 ,37.7, 63.3, and 106 keV energies. It can be seen that in the main phase the ring current was enhanced in the night side under continuous magnetospheric convection. The location of the enhancement did not change much when the IMF Bz was southward. For each of the energy levels, when the IMF Bz turns northward and the particles are trapped, it can be seen that the particles drift around earth and eventually lose energy.

6.5 Discussion and Conclusion

In the previous section, a particular Category I storm was analyzed using the FRC model. The results were compared with a movie map created from low latitude stations spread across LT. The total energy of the earth's ring current calculated by the FRC and

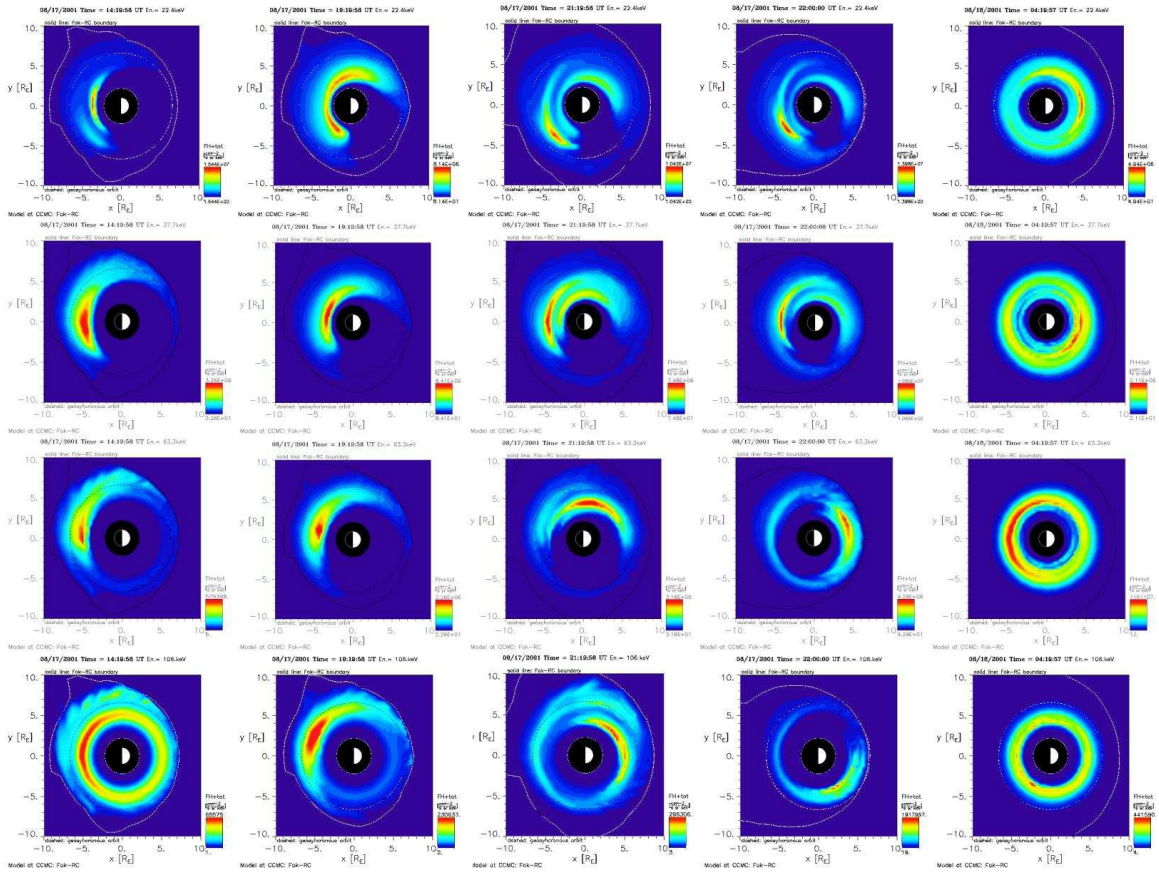

Fig. 6.8: The ring current total particle flux data for energies 22.4, 37.7, 63.3, and 106 keV from the FRC simulation are plotted.

they are compared with the $SymH$ index. These can be seen in the first row of any of the figs. 6.3-6.6. Good agreement was found between the two in the initial and early part of the main phase. FRC model predicted a delayed peak in the ring current energy as compared to the values suggested by $SymH$ index. The recovery phase of the storm also showed a difference in the decay time estimated by the FRC and the $SymH$ index.

Liemohn and Kozyra tested the hypothesis that the observed two phase decay of the $Dst, SymH$ indices can be caused charge exchange processes alone [35]. It was shown that a two-phase decay (a sharp transition between fast and slow recovery rates) of the ring current total energy content is produced when the plasma sheet density is dramatically reduced several hours prior to a sudden reduction in the magnetospheric convection strength. The reverse situation, a convection strength reduction prior to a plasma sheet density decrease, does not produce a two-phase decay signature. A two-phase decay is not visible in the results for simultaneous reduction of these two input parameters.

In our previous work [58], we have shown two phase decay was observed for Category I storms as well. It was also observed by Liemohn and Kozyra [35] that the flow out losses directly follow the convection E-field strength. We observed similar results during the course of this work. These results seem to suggest that during the early phase of the Category I storms the contribution from other magnetospheric currents like the cross tail current might be important. The comparisons made for this study need to be extended to other storms to validate these suggestions

The work done during the course of this study is an exercise in data model validation using the vast network of magnetometer data. Interesting observations were made using the unique movie maps generated from individual low latitude magnetometer station. Although some well known phases of a geomagnetic storms were reliably reproduced in both FRC results and the moviemaps, some interesting differences too were highlighted. The use of several magnetic data to validate model results gives the scientific community with a reliable multipoint tool to match against their models.

Chapter 7

Conclusion and Future Work

7.1 Conclusion

The controversy over the contribution of magnetospheric currents to the Dst index is an open question in the magnetospheric community. The strength of the Dst index indicates the geoeffectiveness of a solar magnetic storm. The ground magnetic perturbations across all the magnetometer station on the surface of the earth are a huge untapped resource for model validations. In this work, we have used a combination of modeling and measurements to understand the perturbing effects of certain magnetospheric currents.

The WINDMI model Dst calculations were improved by including the contributions from the ring, cross tail, and magnetopause currents. For storms with sudden turning of the IMF Bz in the early recovery phase of the storm, the decay rate is found to be similar to storms with gradual northward turning. Two phase decay of the Dst and Dst* indices is observed for most storms. It was found that Dst index could be reliably modeled with the improved WINDMI model.

The energy transfer from the solar wind to the magnetosphere is another open question. A study was done with five different coupling functions to model the Dst and AL indices. The results indicate that the rectified (VB_s) coupling function and the function suggested by Newell are more reliable to model the Dst index. Use of multiple validating constraints was found to be an extremely helpful tool while analyzing conflicting magnetospheric states.

Substorms play a major role in magnetospheric dynamics. The role of substorms in the energization of the ring current is debated. The isotropic boundary location has been used in the past to estimate the strength of the crosstail current. The MT index which is derived from the isotropic boundary is used to act as an additional constraint in addition to the magnetospheric indices used to validate the magnetospheric currents calculated by

WINDMI. The comparison between the perturbations calculated by the MT index and the WINDMI yielded some interesting results. It was found that crosstail current contribution decreased during periods of substorm activity. This decrease in contribution suggests that some additional mechanism contributes to the Dst index during substorms.

The extensive network of magnetometer are a great resource for model validation. A popular ring current simulation by Mei Ching Fok was run for certain storms and the corresponding magnetometer data was compared qualitatively. The model predicts that the flow out losses generally stop after the IMF Bz turns northward. The $ASym - H$ index and the movie maps created from the magnetometer data suggest that the asymmetric contribution to the magnetometer stations remains for a while after the IMF Bz turns northward.

7.2 Future Directions

The work done in this thesis probably raises more questions than it answers. This also means that there are still many avenues for future work. The several magnetospheric models should be compared more comprehensively with this great collection of magnetometer stations to validate their results. The WINDMI model parameters tell us the about the various possible magnetospheric states. A statistical study could be made to find functional form of their relationship with solar wind parameters. The dynamic response of certain global magnetospheric parameters like conductivity and density could be determined this way.

The substorm trigger mechanism is still a question that is hotly debated. A reliable prediction of substorms is not possible unless the physical conditions that trigger a substorm are well known. A lot of work has been done in trying to this solve this problem, but at the present time there is not one single widely accepted theory. The exact instability that triggers the substorm, the state of the magnetosphere most favorable for substorm, the effect of solar wind in the trigger, are all open question that need to answered.

Predicting space weather is an area of active research. The improved WINDMI model gives some of the most accurate prediction of the Dst index. The AL index and its ex-

act relation to the ionospheric currents is still not fully understood. Repositories like the Supermag, Intermagnet, and Magdas should be used to improve the understanding of the birkeland currents. The ionospheric conductivity, magnetosphere-ionospheric coupling and solar wind conditions will all affect these ionospheric currents.

To conclude, it will be helpful to list out some of the questions or problems that were raised during this study. The answers to these would significantly enhance our understanding of the magnetosphere.

- What are the various currents in the magnetosphere and where do they exist?
- How do the various currents in space affect the earth's magnetic field?
- What does the Dst index represent?
- How is the energy transferred across the magnetosphere? Which coupling function is a true representation of the energy transfer?
- What is the relationship between interplanetary E- field and the nightside convection E-field?
- What controls the conductivity of the plasma sheet?
- How does the location of the isotropic boundary change during a substorm?
- Are AE indices a true representation of the auroral electrojets? What is the spatial configuration of these ionospheric currents?
- What controls the ionospheric conductivity during a geomagnetic storm and substorm?
- What triggers a substorm? What are the magnetospheric conditions favorable for substorm triggering?
- What is the role of a substorm in energizing the ring current?

References

[1] Y. Kamide and A. Chian, Eds., *Handbook of the Solar-Terrestrial Environment*. Leipzig, Germany: Springer Verlag, 2007.

[2] Y. Maltsev, "Points of controversy in the study of magnetic storms," *Space Science Reviews*, vol. 110, pp. 227–267, 2004.

[3] I. A. Daglis, R. M. Thorne, W. Baumjohann, and S. Orsini, "The terrestrial ring current: Origin, formation, and decay," *Reviews of Geophysics*, vol. 37, no. 4, pp. 407–438, 1999.

[4] W. Baumjohann, M. Blanc, A. Fedorov, and K. H. Glassmeier, "Current systems in planetary magnetospheres and ionospheres," *Space Science Reviews*, vol. 152, pp. 99–134, 2010. DOI:10.1007/s11214-010-9629-z.

[5] G. L. Siscoe, "Global force balance of region 1 current system," *Journal of Atmospheric and Solar-Terrestrial Physics*, vol. 68, pp. 2119–2126, 2006.

[6] T. I. Gombosi, *Physics of the Space Environment*, J. T. Houghton, M. J. Rycroft, and A. J. Dessler, Eds. New York, NY: Cambridge University Press, 1998.

[7] A. Otto, *Magnetospheric Physics*. Fairbanks, AK: e-Book, 2006.

[8] W. Baumjohann, M. Blanc, A. Fedorov, and K. H. Glassmeier, "Bimodal nature of solar wind magnetosphere ionosphere thermosphere coupling," *Space Science Reviews*, vol. 152, pp. 99–134, 2010. DOI:10.1007/s11214-010-9629-z.

[9] M. Kivelson and C. Russell, Eds., *Introduction to Space Physics*. New York, NY: Cambridge University Press, 1995.

[10] J. U. Kozyra and M. W. Liemohn, "Ring current energy input and decay," *Space Science Reviews*, vol. 109, no. A8, pp. 105–131, Aug. 2003.

[11] M. W. Chen, L. R. Lyons, and M. Schulz, "Stormtime ring-current formation: A comparison between single and double-dip model storms with similar transport characteristics," *Journal of Geophysical Research*, vol. 105, pp. 27,755, 2000.

[12] G. K. Parks, *Physics of Space Plasmas*. Redwood City, CA: Addison Wesley, 1991.

[13] R. K. Burton, R. L. McPherron, and C. T. Russell, "An empirical relationship between interplanetary conditions and Dst," *Journal of Geophysical Research*, vol. 80, no. 31, pp. 4204–4214, Nov. 1975.

[14] J. U. Kozyra, M. W. Liemohn, C. R. Clauer, A. J. Ridley, M. F. Thomsen, J. E. Borovsky, J. L. Roeder, V. K. Jordanova, and W. D. Gonzalez, "Multistep Dst development and ring current composition changes during the 4-6 June, 1991 magnetic storm," *Journal of Geophysical Research*, vol. 107, no. A8, pp. 1295–1322, Aug. 2002. [Online]. Available: http://dx.doi.org/doi/10.1117/1.2818797.

[15] T. P. O'Brien and R. L. McPherron, "An empirical phase space analysis of ring current dynamics: Solar wind control of injection and decay," *Journal of Geophysical Research*, vol. 105, no. A4, pp. 7707–7719, 2000.

[16] M. Sugiura. (1991) On Dst index. [Online]. Available: http://wdc.kugi.kyoto-u.ac.jp/dstdir/dst2/onDstindex.html

[17] P. T. Newell and J. W. Gjerloev, "Evaluation of SuperMAG auroral electrojet indices as indicators of substorms and auroral power," *Journal of Geophysical Research*, vol. 116, no. A12211, pp. 1–12, 2011. DOI:10.1029/2011JA016779.

[18] V. A. Sergeev, M. Malkov, and K. Mursula, "Testing the isotropic boundary algorithm method to evaluate the magnetic field configuration in the tail," *Journal of Geophysical Research*, vol. 98, no. A5, pp. 7609–7620, 1993.

[19] V. Sergeev and B. Gvozdevsky, "Mt-index: A possible new index to characterize the magnetic configuration of magnetotail," *Annales Geophysicae*, vol. 13, pp. 1093–1103, 1995.

[20] B. B. Gvozdevsky and V. A. Sergeev, "MT-index: A possible new index to charactarize the configuration of the magnetotail," *Advances in Space Research*, vol. 18, no. 8, pp. 51–54, 1996.

[21] V. A. Sergeev, E. M. Sazhina, N. A. Tsyganenko, J. A. Lundblad, and F. Soraas, "Pitch angle scattering of energetic protons in the magnetotail current sheet as the dominant source of their isotropic precipitation into the nightside ionosphere," *Planetary and Space Science*, vol. 31, no. 10, pp. 1147–1155, Jan. 1983.

[22] P. T. Newell, Y. I. Feldstein, Y. I. Galperin, and C.-I. Meng, "Morphology of nightside precipitation," *Journal of Geophysical Research*, vol. 101, no. A5, pp. 10,737–10,748, 1996.

[23] P. T. Newell, V. A. Sergeev, G. R. Bikkuzina, and S. Wing, "Characterizing the state of the magnetosphere: Testing the ion precipitation maxima latitude (b2i) and the ion isotropy boundary," *Journal of Geophysical Research*, vol. 103, no. A3, pp. 4739–4745, 1998.

[24] P. Newell, T. Sorelis, K. Liou, C.-I. Meng, and F. Rich, "A nearly universal solar wind-magnetosphere coupling function inferred from 10 magnetospheric state variables," *Journal of Geophysical Research*, vol. 112, no. A01206, pp. 1–16, 2007. DOI:10.1029/2006JA012015.

[25] G. L. Siscoe, G. M. Erickson, B. U. O. Sonnerup, N. C. Maynard, J. A. Schoendorf, K. D. Siebert, D. R. Weimer, W. W. White, and G. R. Wilson, "Hill model of transpolar potential saturation: comparisons with MHD simulations," *Journal of Geophysical Research*, vol. 107, no. A6, p. 1075, 2002. DOI:10.1029/2001JA000109.

[26] J. E. Borovsky, "The rudiments of a theory of solar wind/magnetosphere coupling derived from first principles," *Journal of Geophysical Research*, vol. 113, no. A08228, 2008. DOI:10.1029/2007JA012646.

[27] W. Lyatsky, S. Lyatskaya, and A. Tan, "A coupling function for solar wind effect on geomagnetic activity," *Geophysical Research Letters*, vol. 34, no. L02107, pp. 1–5, 2007. DOI:10.1029/2006GL027666.

[28] M. A. Balikhin, R. J. Boynton, S. A. Billings, M. Gedalin, N. Ganushkina, D. Coca, and H. Wei, "Data based quest for solar wind magnetosphere coupling function," *Geophysical Research Letters*, vol. 37, no. L24107, 2010. DOI:10.1029/2010GL045733.

[29] E. Spencer, A. Rao, W. Horton, and M. L. Mays, "Evaluation of solar wind-magnetosphere coupling functions during geomagnetic storms with the WINDMI model," *Journal of Geophysical Research*, vol. 114, no. A02206, 2009. DOI:10.1029/2008JA013530.

[30] E. Spencer, W. Horton, L. Mays, I. Doxas, and J. Kozyra, "Analysis of the 3 -7 October, 2000 and 15 -24 April, 2002 geomagnetic storms with an optimized nonlinear dynamical model," *Journal of Geophysical Research*, vol. 112, no. A04S90, 2007. DOI:10.1029/2006JA012019.

[31] W. Horton, R. S. Weigel, D. Vassiliadis, and I. Doxas, "Substorm classification with the WINDMI model," *Nonlinear Processes in Geophysics*, vol. 10, pp. 363–371, 2003.

[32] S. Takahashi, T. Iyemori, and M. Takeda, "A simulation of the storm time ring current," *Planetary and Space Science*, vol. 38, no. 9, pp. 1133–1141, 1990.

[33] Y. I. Feldstein and L. A. Dremukhina, "On the two-phase decay of the Dst-variation," *Journal of Geophysical Research*, vol. 27, no. 17, pp. 2813–2816, Sept. 2000.

[34] J. U. Kozyra, M. C. Fok, E. R. Sanchez, D. S. Evans, D. Hamilton, and A. F. Nagy, "The role of precipitation looses in producing the rapid early recovery phase of the Great Magnetic Storm of February 1986," *Journal of Geophysical Research*, vol. 103, no. A4, pp. 6801–6814, 1998. DOI:10.1029/2005JA011091.

[35] M. W. Liemohn and J. U. Kozyra, "Testing the hypothesis that charge exchange can cause a two-phase decay," in *The Inner Magnetosphere: Physics and Modeling*, T. I. Pulkkinen, N. A. Tsyganenko, and R. H. W. Friedel, Eds. Washington, DC: American Geophysical Union, vol. 155, pp. 211–226, 2005.

[36] V. K. Jordanova, L. M. Kistler, M. F. Thomsen, and C. G. Mouikis, "Effects of plasma sheet variability on the fast initial ring current decay," *Geophysical Research Letters*, vol. 30, no. 6,1311, 2003. DOI:10.1029/2002GL016576.

[37] I. I. Alexeev, E. S. Belenkaya, V. V. Kalegaev, Y. I. Feldstein, and A. Grafe, "Magnetic storms and magnetotail currents," *Journal of Geophysical Research*, vol. 101, no. A4, pp. 7737–7747, 1996.

[38] V. Kalegaev and E. Makarenkov, "Relative importance of ring and tail currents to Dst under extremely disturbed conditions," *Journal of Atmospheric and Solar-Terrestrial Physics*, vol. 70, pp. 519–525, 2008.

[39] D. G. Mitchell, K. C. Hsieh, C. C. Curtis, D. Hamilton, H. D. VOSS, E. C. Roelof, and P. C:son-Brandt, "Imaging two geomagnetic storms in energetic neutral atoms," *Geophysical Research Letters*, vol. 28, no. 6, pp. 1151–1154, 2001. DOI:10.1029/2003JA010164.

[40] K. Keika, M. Nose, S. Ohtani, K. Takahashi, S. P. Christon, and R. W. McEntire, "Outflow of energetic ions from the magnetosphere and its contribution to the decay of the storm time ring current," *Journal of Geophysical Research*, vol. 110, no. A09210, 2005. DOI:10.1029/2004JA010970.

[41] D. Y. Lee, L. R. Lyons, and G. D. Reeves, "Comparison of geosynchronous energetic particle flux responses to solar wind dynamic pressure enhancements and substorms," *Journal of Geophysical Research*, vol. 110, no. A09213, 2005. DOI:10.1029/2005JA011091.

[42] I. Doxas, W. Horton, W. Lin, S. Seibert, and M. Mithaiwala, "A dynamical model for the coupled inner magnetosphere and tail," *IEEE Transactions on Plasma Science*, vol. 32, no. 4, pp. 1443–1448, 2004.

[43] W. Horton, M. Mithaiwala, E. Spencer, and I. Doxas, "Windmi: A family of physics network models for storms and substorms," in *Multi-Scale Coupling of Sun-Earth Processes*, A. Lui, Y. Kamide, and G. Consolini, Eds. Amsterdam, Netherlands: Elsevier Publishing Company, pp. 431–446, 2005.

[44] R. Wolf, R. Spiro, S. Sazykin, and F. Toffoletto, "How the earths inner magnetosphere works: An evolving picture," *Journal of Atmospheric and Solar-Terrestrial Physics*, vol. 69, pp. 288–302, 2007. DOI:10.1029/2005JA011091.

[45] P. H. Reiff and J. G. Luhmann, "Solar wind control of the polar-cap voltage," in *Solar Wind-Magnetosphere Coupling*, Y. Kamide and J. A. Slavin, Eds. Tokyo, Japan: Terra Science, pp. 453–476, 1986.

[46] A. Dessler and E. N. Parker, "Hydromagnetic theory of geomagnetic storms," *Journal of Geophysical Research*, vol. 64, pp. 2239–59, 1959.

[47] N. Sckopke, "A general relation between the energy of trapped particles and the disturbance field near the Earth," *Journal of Geophysical Research*, vol. 71, p. 3125, 1966.

[48] D. A. Coley, *An Introduction to Genetic Algorithms for Scientists and Engineers.* Tokyo, Japan: World Scientific Publishing Co., Inc., 2003.

[49] T. P. O'Brien, R. L. McPherron, and M. W. Liemohn, "Continued convection and the initial recovery of Dst," *Geophysical Research Letters*, vol. 29, no. 23, p. 2143, 2002. DOI:10.1029/2002GL015556.

[50] M. W. Liemohn, J. U. Kozyra, C. R. Clauer, and A. J. Ridley, "Computational analysis of the near-earth magnetospheric current system during two phase decay storms," *Journal of Geophysical Research*, vol. 106, no. A12, pp. 29,531–29,542, Dec. 2001.

[51] N. A. Tsyganenko and M. I. Sitnov, "Modeling the dynamics of the inner magnetosphere during strong geomagnetic storms," *Journal of Atmosphere and Terrestrial Physics*, vol. 110, no. A3208, Mar. 2005. DOI:10.1029/2004JA010798,

[52] G. L. Siscoe, R. L. McPherron, and V. K. Jordanova, "Diminished contribution of ram pressure to Dst during magnetic storms," *Journal of Geophysical Research*, vol. 110, no. A12227, 2005. DOI:1029/2005JA011120.

[53] I. I. Alexeev, V. V. Kalegaev, E. S. Belenkaya, S. Y. Bobrovnikov, Y. I. Feldstein, and L. I. Gromova, "Dynamic model of the magnetosphere: Case study for January 9-12, 1997," *Journal of Geophysical Research*, vol. 106, no. A11, pp. 25,683–25,693, 2001.

[54] Y. P. Maltsev, A. A. Arykov, E. G. Belova, B. B. Gvozdevskay, and V. V. Safargaleev, "Magnetic flux redistribution in the storm time magnetosphere," *Journal of Geophysical Research*, vol. 101, no. A4, pp. 7697–7704, 1996.

[55] N. E. Turner, D. N. Baker, T. I. Pulkkinen, and R. L. McPherron, "Evaluation of the tail current contribution to Dst," *Journal of Geophysical Research*, vol. 105, no. A02212, pp. 5431–5439, 2000.

[56] Y. P. Maltsev and A. A. Ostapenko, "Comment on evaluation of the tail current contribution to Dst by N. E. Turner et al." *Journal of Geophysical Research*, 2002. DOI:10.1029/2001JA900098.

[57] D. N. Baker, N. E. Turner, and T. I. Pulkkinen, "Energy transport and dissipation in the magnetosphere during geomagnetic storms," *Journal of Atmospheric and Solar-Terrestrial Physics*, vol. 63, pp. 421–429, 2001.

[58] S. Patra, E. Spencer, W. Horton, and J. Sojka, "Study of Dst/ring current recovery times using the windmi model," *Journal of Geophysical Research*, vol. 116, no. A02212, 2011. DOI:10.1029/2010JA015824.

[59] G. L. Siscoe, G. M. Erickson, B. U. O. Sonnerup, N. C. Maynard, J. A. Schoendorf, K. D. Siebert, D. R. Weimer, W. W. White, and G. R. Wilson, "Hill model of transpolar potential saturation: comparisons with MHD simulations," *Journal of Geophysical Research*, vol. 107, no. A6, p. 1075, 2002. DOI:10.1029/2001JA000109.

[60] G. L. Siscoe, N. U. Crooker, and K. D. Siebert, "Transpolar potential saturation: roles of region-1 current system and solar wind ram pressure," *Journal of Geophysical Research*, vol. 107, no. A10, p. 1321, 2002. DOI:10.1029/2001JA009176.

[61] D. M. Ober, N. C. Maynard, and W. J. Burke, "Testing the Hill model of transpolar potential saturation," *Journal of Geophysical Research*, vol. 108, no. A12, p. 1467, 2003. DOI:10.1029/2003JA010154.

[62] N. Buzulukova, M. Fok, A. Pulkkinen, M. Kuznetsova, T. E. Moore, A. Glocer, P. C. Brandt, G. Toth, and L. Rastatter, "Dynamics of ring current and electric fields in the inner magnetosphere during disturbed periods: CRCM-BATS-R-US coupled model," *Journal of Geophysical Research*, vol. 115, no. A05210, 2010. DOI:10.1029/2009JA014621.

[63] M. C. Fok, R. A. Wolf, R. W. Spiro, and T. E. Moore, "Comprehensive computational model of earth's ring current," *Journal of Geophysical Research*, vol. 106, no. A5, pp. 8417–8424, 2001.

[64] W. Horton and I. Doxas, "A low dimensional energy-conserving state space model for substorm dynamics," *Journal of Geophysical Research*, vol. 101, no. A12, pp. 27, 223–27,237, Dec. 1996.

[65] W. Horton and I. Doxas, "A low dimensional dynamical model for the solar wind driven geotail ionosphere system," *Journal of Geophysical Research*, vol. 103, no. A3, pp. 4561–4572, Mar. 1998.

[66] M. J. Mithaiwala and W. Horton, "Substorm injections produce sufficient electron energization to account for MeV flux enhancements following some storms," *Journal of Geophysical Research*, vol. 110, no. A07224, pp. 363–371, 2005. DOI:10.1029/2004JA010511.

[67] M. Temerin and X. Li, "Dst model for 1995-2002," *Journal of Geophysical Research*, vol. 111, no. A04221, Apr. 2006. DOI:10.1029/2005JA011257.

[68] M. Temerin and X. Li, "A new model for the prediction of Dst on the basis of the solar wind," *Journal of Geophysical Research*, vol. 107, no. A12,1472, Dec. 2002. DOI:10.1029/2001JA007532

[69] T. Asikainen, V. Maliniemi, and K. Mursula, "Modeling the contributions of ring, tail, and magnetopause currents to the corrected Dst index," *Journal of Geophysical Research*, vol. 115, no. A12203, Dec. 2010. DOI:10.1029/2010JA015774.

[70] R. Bala, P. H. Reiff, and J. E. Landivar, "Real-time prediction of magnetospheric activity using the boyle index," *Space Weather*, vol. 7, no. S04003, Apr. 2009. DOI:10.1029/2008SW000407.

[71] M. Mattinen, "Modeling and forecasting of local geomagnetic activity," Master's thesis, Aalto University, School of Science and Technology, Faculty of Information and Natural Sciences, Helsinki, 2010.

[72] N. Y. Ganushkina, T. I. Pulkkinen, M. V. Kubyshkina, H. J. Singer, and C. T. Russell, "Long-term evolution of magnetospheric current systems during storms," *Annales Geophysicae*, vol. 22, pp. 1317–1334, 2004.

[73] J. Aguado, C. Cid, E. Saiz, and Y. Cerrato, "Hyperbolic decay of the Dst index during the recovery phase of intense geomagnetic storms," *Journal of Geophysical Research*, vol. 115, no. A07220, 2010. DOI:10.1029/2009JA014658.

[74] M. C. Fok, J. U. Kozyra, and A. F. Nagy, "Lifetime of ring current particles due to coulomb collisions in the plasmasphere," *Journal of Geophysical Research*, vol. 96, no. A5, pp. 7861–7867, 1991.

[75] M. C. Fok, J. U. Kozyra, A. F. Nagy, C. E. Rasmussen, and G. V. Khazanov, "Decay of equatorial ring current ions and associated aeronomical consequenc," *Journal of Geophysical Research*, vol. 98, no. A11, pp. 19,381–19,393, 1993.

[76] V. K. Jordanova, J. U. Kozyra, A. F. Nagy, and G. V. Khazanov, "Kinetic model of the ring current-atmosphere interactions," *Journal of Geophysical Research*, vol. 102, no. A7, pp. 14,279–14,291, 1997. DOI:10.1029/2009JA014658.

[77] V. K. Jordanova, C. J. Farrugia, R. M. Thorne, G. V. Khazanov, G. D. Reeves, and M. F. Thomsen, "Modeling ring current proton precipitation by electromagnetic ion cyclotron waves during the may 14-16, 1997, storm," *Journal of Geophysical Research*, vol. 106, no. A1, pp. 7–22, 2001.

[78] M. Walt and H. D. Voss, "Losses of ring current ions by strong pitch angle scattering," *Geophysical Research Letters*, vol. 28, no. 20, pp. 3839–3841, 2001.

[79] E. Spencer, P. Kasturi, S. Patra, W. Horton, and M. L. Mays, "Influence of solar wind-magnetosphere coupling functions on the Dst index," *Journal of Geophysical Research*, vol. 116, no. A12235, 2011. DOI:10.1029/2011JA016780.

[80] M. Kubyshkina, V. Sergeev, N. Tsyganenko, V. Angelopoulos, A. Runov, H. Singer, K. H. Glassmeier, H. U. Auster, and W. Baumjohann, "Toward adapted time-dependent magnetospheric models:a simple approach based on tuning the standard model," *Journal of Geophysical Research*, vol. 114, no. A00C21, 2009. DOI:10.1029/2008JA013547.

[81] V. A. Sergeev, T. I. Pulkkinen, R. J. Pellinen, and N. A. Tsyganenko, "Hybrid state of the tail magnetic configuration during steady convection events," *Journal of Geophysical Research*, vol. 99, no. A12, pp. 23,571–23,582, 1994. DOI:10.1029/2008JA013547.

[82] M. Meurant, J.-C. Gerard, C. Blockx, E. Spanswick, E. F. Donovan, B. H. V. Coumans, and M. Connors, "EL - a possible indicator to monitor the magnetic field stretching at global scale during substorm expansive phase: Statistical study," *Journal of Geophysical Research*, vol. 112, no. A05222, 2007. DOI:10.1029/2006JA012126.

[83] A. Konradi, C. L. Semar, and T. A. Fritz, "Substorm-injected protons and electrons and the injection boundary model," *Journal of Geophysical Research*, vol. 80, no. 4, pp. 543–552, Feb. 1975.

[84] E. R. Sanchez, B. H. Mauk, P. T. Newell, and C. Meng, "Low-altitude observations of the evolution of substorm injection boundaries," *Journal of Geophysical Research*, vol. 98, no. A4, pp. 5815–5838, Apr. 1993.

[85] E. F. Donovan, B. J. Jackel, I. Voronkov, T. Sotirelis, F. Creutzberg, and N. A. Nicholson, "Ground-based optical determination of the b2i boundary: A basis for an optical MT-index," *Journal of Geophysical Research*, vol. 108, no. A3, 1115, pp. 1147–1155, Mar. 2003. DOI:10.1029/2001JA009198.

[86] P. T. Jayachandran, E. F. Donovan, J. W. MacDougall, D. R. Moorcroft, J. S. Maurice, and P. Prikryl, "SuperDARN E-region backscatter boundary in the dusk-midnight sector tracer of equatorward boundary of the auroral oval," *Annales Geophysicae*, vol. 20, pp. 1899–1904, Jul. 2002.

[87] P. T. Jayachandran, J. W. MacDougall, J. P. St-Maurice, D. R. Moorcroft, P. T. Newell, and P. Prikryl, "Coincidence of the ion precipitation boundary with the hf e region backscatter boundary in the dusk-midnight sector of the auroral oval," *Geophysical Research Letters*, vol. 29, no. 8, 1256, pp. 1147–1155, Apr. 2002. DOI:10.1029/2001GL014184.

[88] K. Mursula and A. Karinen, "Explaining and correcting the excessive semiannual variation in the Dst index," *Geophysical Research Letters*, vol. 32, no. L14107, 2005. DOI:10.1029/2005GL023132.

[89] P. Newell, T. Sotirelis, J. P. Skura, C. I. Meng, and W. Lyatsky, "Ultraviolet insolation drives seasonal and diurnal space weather variations," *Journal of Geophysical Research*, vol. 107(A10), no. 1305, 2002. DOI:10.1029/2001JA000296.

[90] R. A. Langel and R. H. Estes, "Large-scale, near-field magnetic fields from external sources and the corresponding induced internal field," *Journal of Geophysical Research*, vol. 90, no. B3, pp. 2487–2494, Feb. 1985.

[91] W. Horton, R. S. Weigel, D. Vassiliadis, and I. Doxas, "Substorm classification with the WINDMI model," *Nonlinear Processes in Geophysics*, vol. 10, pp. 363–371, 2003.

[92] E. Spencer, A. Rao, W. Horton, and M. L. Mays, "Evaluation of solar wind-magnetosphere coupling functions during geomagnetic storms with the WINDMI model," *Journal of Geophysical Research*, vol. 114, no. A02206, 2009. DOI:10.1029/2008JA013530.

[93] X. Cai, "Investigation of global periodic sawtooth oscillations observed in energetic particle flux at geosynchronous orbit." Ph.D. dissertation, University of Michigan, Ann Arbor, MI, 2007.

[94] P. Yoon, A. Lui, and M. Sitnov, "Generalized lower-hybrid drift instabilities in current sheet equilibrium," *Physics of Plasma*, vol. 9, no. 5, pp. 1526–1538, 2002.

[95] R. Wolf, R. Spiro, S. Sazykin, and F. Toffoletto, "How the earth's inner magnetosphere works: An evolving picture," *Journal of Atmospheric and Solar-Terrestrial Physics*, vol. 69, pp. 288–302, 2007. DOI:10.1029/2005JA011091.

[96] S. Ohtani, M. Nose, G. Rostoker, H. Singer, A. T. Y. Lui, and M. Nakamura, "Storm-substorm relationship: Contribution of the tail current to Dst," *Journal of Geophysical Research*, vol. 106, no. A10, pp. 21,199–21,209, Oct. 2001.

[97] M. C. Fok and T. E. Moore, "Ring current modeling in a realistic magnetic field configuration," *Geophysical Research Letters*, vol. 24, no. 14, pp. 1775–1778, Jul. 1997.

[98] N. Partamies, T. Pulkkinen, R. McPherron, K. McWilliams, C. Bryant, E. Tanskanen, H. Singer, G. Reeves, and M. Thomsen, "Statistical survey on sawtooth events, SMCs and isolated substorms," *Advances in Space Research*, vol. 44, no. 3, pp. 376–384, 2009. DOI:10.1016/j.asr.2009.03.013.

[99] M. L. Mays, W. Horton, E. Spencer, and J. Kozyra, "Real-time predictions of geomagnetic storms and substorms: Use of the solar wind magnetosphere-ionosphere system model," *Space Weather*, vol. 7, no. S07001, 2009. DOI:10.1029/2008SW000459.

[100] D. Baker, T. Pulkkinen, J. Buchner, and A. Klimas, "Substorms: A global instability of the magnetosphere-ionosphere system," *Journal of Geophysical Research*, vol. 104, no. A7, pp. 14 601–14 611, 1999.

[101] V. Sergeev, V. Angelopoulos, and R. Nakamura, "Recent advances in understanding substorm dynamics," *Geophysical Research Letters*, vol. 39, no. L05101, 2012. DOI:10.1029/2012GL050859.

[102] A. Pulkkinen, A. Klimas, D. Vassiliadis, and V. Uritsky, "Role of stochastic fluctuations in the magnetosphere-ionosphere system: A stochastic model for the AE index variations," *Journal of Geophysical Research*, vol. 111, no. A10, 2006. DOI:10.1029/2006JA011661.

[103] A. Klimas, D. Baker, D. Vassiliadis, D. Roberts, D. Fairfield, and J. Buchner, "A nonlinear analog model of geomagnetic activity," *Journal of Geophysical Research*, vol. 97, no. A8, pp. 12,253–12,266, 1992.

[104] A. Klimas, D. Vassiliadis, D. Baker, and D. Roberts, "The organized nonlinear dynamics of the magnetosphere," *Journal of Geophysical Research*, vol. 101, no. A6, pp. 13 089–13 113, 1996.

[105] G. Blanchard and R. McPherron, "A bimodal representation of the response function relating the solar wind electric field to the AL index," *Advances in Space Research*, vol. 13, no. 4, pp. 71–74, 1993.

[106] D. Vassiliadis, A. Klimas, D. Baker, and D. Roberts, "A description of solar-wind magnetosphere coupling based on nonlinear filters," *Journal of Geophysical Research*, vol. 100, no. A3, pp. 3495–3512, Mar. 1995.

[107] A. Klimas, J. Valdivia, D. Vassiliadis, and D. Baker, "AL index prediction using data-derived nonlinear prediction filters," in *Physics of Space Plasmas*, T. Chang and J. Jasperse, Eds. Cambridge, MA: MIT Center for Theoretical Geo/Cosmo Plasma Physics, pp. 431–446, 1998.

[108] R. Weigel, W. Horton, T. Tajima, and T. Detman, "Forecasting auroral electrojet activity from solar wind input with neural networks," *Geophysical Research Letters*, vol. 26, no. 10, pp. 1353–1356, 1999.

[109] B. Gallardo-Lacourt, Y. Nishimura, L. Lyons, and E. Donovan, "External triggering of substorms identified using modern optical versus geosynchronous particle data," *Annales Geophysicae*, vol. 30, pp. 667–673, 2012. DOI:10.5194/angeo-30-667-2012.

[110] C. Rasmussen, R. Schunk, and V. Wickwar, "A photochemical equilibrum model for ionospheric conductivity," *Journal of Geophysical Research*, vol. 93, no. A9, pp. 9831–9840, 1988.

[111] B. H. Ahn, A. D. Richmond, Y. Kamide, H. W. Kroehl, B. A. Emery, O. de la Beaujardie, and S. I. Akasofu, "An ionospheric conductance model based on ground magnetic disturbance data," *Journal of Geophysical Research*, vol. 103, p. 14769, 1998.

[112] R. M. Robinson, R. R. Vondrak, K. Miller, T. Dabbs, and D. Hardy, "On calculating ionospheric conductances from the flux and energy of precipitating electrons," *Journal of Geophysical Research*, vol. 92, no. A3, pp. 2565–2669, 1987.

[113] B. Tang, C. Wang, Y. Hu, and J. Kan, "Intensification of the cowling current in the global MHD simulation model," *Journal of Geophysical Research*, vol. 116, no. A06204, 2011. DOI:10.1029/2010JA016320.

[114] A. Aksnes, J. Stadsnes, J. Bjordal, N. Ostgaard, R. R. Vondrak, D. L. Detrick, T. J. Rosenberg, G. A. Germany, and D. Chenette, "Instantaneous ionospheric global conductance maps during an isolated substorm," *Annales Geophysicae*, vol. 20, pp. 1181–1191, 2002.

[115] J. Gjerloev and R. Hoffman, "Height-integrated conductivity in auroral substorms: 1. Data," *Journal of Geophysical Research*, vol. 105, no. A1, 2000. DOI:10.1029/1999JA900354.

[116] C. Huang, J. Foster, L. Goncharenko, G. Reeves, J. Chau, K. Yumoto, and K. Kitamura, "Variations of low-latitude geomagnetic fields and Dst index caused by magnetospheric substorms," *Journal of Geophysical Research*, vol. 109, no. A05219, 2004. DOI:10.1029/2003JA010334.

[117] V. Coumans, J. C. Gerard, B. Hubert, M. Meurant, and S. B. Mende, "Global auroral conductance distribution due to electron and proton precipitation from IMAGE-FUV observations," *Annales Geophysicae*, vol. 22, no. 5, pp. 1595–1611, 2004.

[118] J. Birn, A. V. Artemyev, D. N. Baker, M. Echim, M. Hoshino, and L. M. Zelenyi, "Particle acceleration in the magnetotail and aurora," *Space Science Reviews*, vol. 173, pp. 49–102, 2012. DOI:10.1007/s11214-012-9874-4.

[119] S. Knight, "Parallel electric fields," *Planetary and Space Science*, vol. 21, pp. 741–750, 1973.

[120] A. Morioka, Y. Miyoshi, Y. Miyashita, Y. K. an H. Misawa, F. Tsuchiya, R. Kataoka, A. Kadokura, T. Mukai, K. Yumoto, D. Menietti, G. parks, K. Liou, F. Honary, and E. Donovan, "Two-step evolution of auroral acceleration at substorm onset," *Journal of Geophysical Research*, vol. 115, no. A11213, 2010. DOI:10.1029/2010JA015361.

[121] J. Gjerloev and R. Hoffman, "Height-integrated conductivity in auroral substorms: 2. Modelling," *Journal of Geophysical Research*, vol. 105, no. A1, 2000. DOI:10.1029/1999JA900353.

[122] S. Akasofu, "Several 'controversial' issues on substorms," *Space Science Reviews*, vol. 113, no. 1-2, pp. 1–40, 2004.

[123] W. D. Gonzalez, B. T. Tsurutani, A. L. Gonzalez, E. J. Smith, F. Tang, , and S.-I. Akasofu, "Solar wind-magnetosphere coupling during intense magnetic storms (1978-1979)," *Journal of Geophysical Research*, vol. 94, no. A7, pp. 8835–8851, Jul. 1989.

[124] J. J. Love and J. L. Gannon, "Movie-maps of low-latitude magnetic storm disturbance," *Space Weather*, vol. 8, no. S06001, 2010. DOI:10.1029/2009SW000518.

[125] F. Toffoletto, S. Sazykin, R. Spiro, and R. Wolf, "Inner magnetospheric modeling with the rice convection model," *Space Science Reviews*, vol. 107, pp. 175–196, 2003.

[126] D. L. D. Zeeuw, S. Sazykin, R. A. Wolf, T. I. Gombosi, A. J. Ridley, and G. Toth, "Coupling of a global MHD code and an inner magnetospheric model: Initial results," *Journal of Geophysical Research*, vol. 109, no. A12219, pp. 8417–8424, 2004. DOI:10.1029/2003JA010366.

[127] A. N. Zaitev and Bostrom, "On methods of graphical displaying of polar magnetic disturbances," *Planetary and Space Science*, vol. 19, pp. 643–649, 1971.

[128] C. R. Clauer and R. L. McPherron, "Mapping local time universal time development of magnetospheric substorms using mid-latitude magnetic observations," *Journal of Geophysical Research*, vol. 79, pp. 2811–2820, 1974.

[129] C. R. Clauer, M. W. Liemohn, J. U. Kozyra, and M. L. Reno, "The relationship of storms and substorms determined from mid-latitude ground-based magnetic maps, in disturbances in geospace: The storm-substorm relationship," *Geophysics Monograph Series*, vol. 142, pp. 143–157, 2003, AGU, Washington, DC.

[130] I. A. Daglis, J. U. Kozyra, Y. Kamide, D. Vassiliadis, A. S. Sharma, M. W. Liemohn, W. D. Gonzalez, B. T. Tsurutani, and G. Lu, "Intense space storms: Critical issues and open disputes," *Journal of Geophysical Research*, vol. 108, no. A5, p. 1208, 2003. DOI:10.1029/2002JA009722.

[131] C. R. Clauer, X. Cai, D. Welling, A. DeJong, and M. G. Henderson, "Characterizing the 18 April 2002 storm-time sawtooth events using ground magnetic data," *Journal of Geophysical Research*, vol. 111, no. A04S90, p. 1208, 2006. DOI:10.1029/2005JA011099.

[132] S. Chapman and V. C. A. Ferraro, "A new theory of magnetic storms," *Nature*, vol. 126, pp. 129–130, 1930.

[133] G. L. Siscoe and K. D. Siebert, "Bimodal nature of solar wind-magnetosphere-ionosphere-thermosphere coupling," *Journal of Atmospheric and Solar-Terrestrial Physics*, vol. 68, pp. 911–920, 2006.

Vita

Swadesh Patra

Published Journal Articles

- The effect of nonlinear ionospheric conductivity enhancement on magnetospheric substorms, *Nonlinear Processes in Geophysics* , *Accepted for publication*, MS No.: $npg - 2012 - 87$.

- Plasma Impedance Probe Simulations and Comparison to Sounding Rocket Mission Data, S. Patra and E. Spencer, *IEEE, Transactions on Plasma Science*, *Accepted for publication*, doi: $10.1109/TPS.2012.2225112$.

- The Influence of Solar Wind Magnetosphere Coupling Functions on the Dst Index, E. Spencer, P. Kasturi, S. Patra, W. Horton, M. L. Mays, *Journal of Geophysical Research*, Vol. 116, A12235, doi:10.1029/2011JA016780,2012.

- Study of Dst/ring current recovery times using the WINDMI model, S. Patra, E. Spencer, W. Horton, J. Sojka, *Journal of Geophysical Research*, Vol. 116, A02212, doi:10.1029/2010JA015824E (2011).

- Electron density and electron neutral collision frequency in the ionosphere using plasma impedance probe measurements, E. Spencer, S. Patra, T. Andriyas, C. Swenson, J. Ward, A. Barjatya, *Journal of Geophysical Research*, Vol. 113, A09305, doi: 10.1029/2007JA013004(2008).

Journal Articles under Review

- Effects of changing solar wind conditions on open drift paths, S. Patra, E.Spencer, *Journal of Geophysical Research*.

- A Novel Method to Determine Ionospheric Current Systems Using Amateur Satellite Radio Frequencies, E.Spencer, P.Kasturi, S.Patra, A.Raj, *Radio Science*.

- Magnetotail Currents contribution to the Dst index, S.Patra, E. Spencer, T. Asikainen, and W. Horton, *Advances in Space Research*.

Published Conference Papers

- Fully Integrated electronics system for a plasma impedance probe, M. Jayram, M. E. Hamoui, S. Patra, C. Winstead, E. Spencer, in *22nd Annual AIAA/USU conference on small satellites* 2008.

- Plasma impedance probe analysis with a finite difference time domain simulation, E. A. Spencer, S. Patra, T. Andriyas, C. M. Swenson, J. Ward, in *16th IEEE-Pulsed Power Conference*, 2007, doi: 10.1109/PPPS.2007.4652493.